Anode Engineering for Proton Exchange Membrane Water Electrolyzers

Chang Qiu,[#] Zikai Xu,[#] Feng-Yang Chen, and Haotian Wang*

Read Online

ACCESS | Metrics & More | Article Recommendations

ABSTRACT: Sustainable hydrogen (H_2) production via water electrolysis is one of the most critical pathways to decarbonize the chemical industry. Among various electrolyzer technologies, proton exchange membrane (PEM) water electrolyzer (PEMWE) is widely regarded as having a great advantage and promise for large-scale H_2 production given its high efficiency, reliable stability, and high output pressure. Though state-of-the-art iridium-based catalysts exhibit satisfying activity and stability for oxygen evolution reaction at the anode, their high loadings, as well as the precious metal coating and titanium bulk of porous transport layer (PTL) and bipolar plates, significantly add to the capital cost of the PEMWE stack. The respective optimization and integration of PTL, catalyst layer (CL) and PEM is critical for enhancing charge transfer, mass transport, and catalyst utilization to lower the operation and capital cost, yet it has not received adequate attention. In this review, anode engineering strategies to rationally design PTL, PTL/CL interface and PEM/CL interface for performance improvement and cost reduction are summarized. Current understandings on PTL material, structure, and two-phase transport properties are first gathered, followed by the discussion of anode interface engineering methods and catalyst coating techniques. Given the raising attention to large-scale water electrolyzers operating at high current densities, this review provides a practical and comprehensive direction for next-generation PEMWE anode design by addressing the integration of key components related to the cost, efficiency and stability issues in PEMWE.

KEYWORDS: *water splitting, proton exchange membrane water electrolyzers, oxygen evolution reaction, porous transport layer, interface engineering*
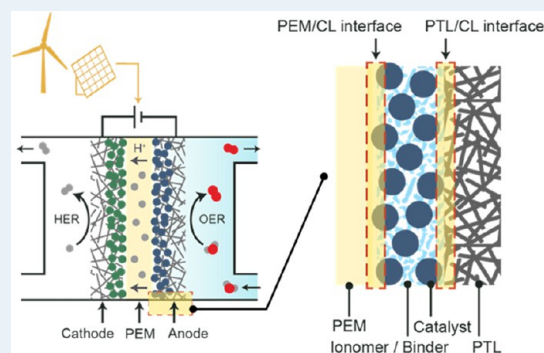
1. INTRODUCTION

Since the industrial revolution, massive consumption of fossil fuels and deforestation have given rise to global warming and climate change, posing serious threats to human health and biodiversity.[1−3] In recent years, electrochemical fuel synthesis driven by renewable electricity has been proposed and extensively investigated to ultimately realize the decarbonization of the chemical industry, which includes water splitting, oxygen reduction, carbon dioxide reduction and nitrogen fixation.[4−8] Among these emerging electrolysis technologies, sustainable hydrogen (H_2) production via water splitting is generally regarded as a critical pathway to address the current energy and environmental challenges, due to the easy accessibility of water and eco-friendly combustion of H_2.[9,10]

At present, the leading water electrolyzer designs include traditional alkaline water electrolyzers (AWE), proton exchange membrane (PEM) water electrolyzers (PEMWE, Figure 1a) and anion exchange membrane (AEM) water electrolyzers (AEMWE). Though well-established, the conventional AWE suffer from limited operating current density, gas crossover, and low output pressure, owing to the presence of a

liquid electrolyte and a diaphragm in the cell.[1,11] In comparison, the compact configuration of membrane electrode assembly (MEA) provides low resistance, fast response, high efficiency, gas purity, and safety for PEMWE and AEMWE, promising for large-scale H_2 production.[11] For the relatively new AEMWE technology, despite a pool of low-cost electrocatalysts available for its local alkaline environment, the poor electrochemical stability of current AEM and anion exchange ionomers largely hampers its practical applications.[12,13] In contrast, PEMWE is a more mature technology, with long-term stable operation demonstrated and megawatt-scale commercial electrolyzers being developed.[14−18] The share of PEMWE in the total installed capacity of water
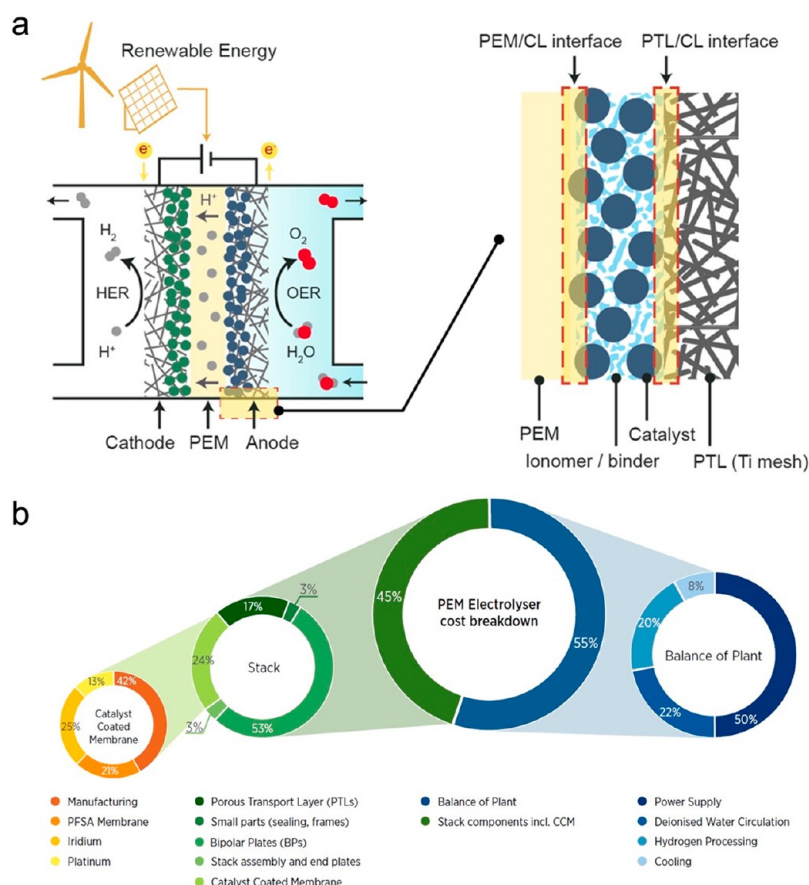
Figure 1. (a) Schematic illustration of sustainable H_2 production in a PEMWE. (b) Cost distribution of a typical PEMWE stack. Reproduced with permission from ref 24. Copyright 2020 International Renewable Energy Agency.

electrolyzers is estimated to be gradually increasing and equal to that of conventional AWE by 2030.[19]

Though the price of renewable electricity is continuously going down, further cost reduction and performance improvement in PEMWE are still necessary to make green H_2 produced from this technology more competitive than fossil fuels. Due to the employment of PEM and high voltages required by the sluggish oxygen (O_2) evolution reaction (OER), a highly acidic and oxidative environment is created at anode in PEMWE, necessitating the use of robust but expensive materials.[20] To date, while exciting progress has been made in the development of nonprecious metal-based electrocatalysts for efficient OER in PEMWE at lab-scale, iridium- (Ir-) based materials are still widely recognized as the only practical anode catalysts for PEMWE due to their outstanding stability and activity, which however possess a high price and a very limited supply.[21−23] Except the high loading of expensive Ir-based noble-metal catalysts, precious metal coating and titanium bulk for porous transport layer (PTL) and bipolar plates (BPP) are another two of the main capital cost contributors in a typical PEMWE stack (Figure 1b).[24] Moreover, it remains a challenge to lower the operation cost via cell performance enhancement and total energy input reduction for satisfying electrical efficiency.

PTL, which is also known as the gas diffusion layer (GDL) or the liquid/gas diffusion layer (LGDL), is a vital multifunctional layer sandwiched between catalyst layer (CL) and BPP. The composition and structure of PTL are crucial to determine charge, mass, and heat transport properties, as well as a large

portion of capital cost in PEMWE.[25,26] Additionally, as expected in the future that the anode catalyst loading will be gradually reduced, the influence of PTL properties on the cell performance will become increasingly pronounced,[27] further emphasizing the importance of PTL engineering.

On the other hand, the interfaces between the compressed functional layers in electrochemical devices, including batteries,[28,29] solar cells,[30,31] protonic ceramic cells,[32] fuel cells,[33,34] and electrolyzers,[35,36] are crucial intersections which have profound impacts on the transport phenomena and device performance. For PEMWE, the investigation and rational designs of interfaces between components are also critical. For instance, through in situ visualization, Mo et al. observed that water splitting only happens where catalysts are in direct contact with PTL, revealing a significant waste of the expensive Ir-based catalyst when uniformly distributed.[37] Another example from our group demonstrated that poorly fabricated anode electrode will cause catalyst detachment from PTL and performance degradation, suggesting the necessity to stabilize the interface between CL and PTL by advanced engineering approaches.[15] While countless studies have demonstrated novel catalyst designs with enhanced performance for OER,[38−42] only a few works have focused on developing strategies to engineering the other components of the anode electrode, namely the respective optimization and integration of PTL, CL, and PEM.

In this review, the novel designs of PTL, PTL/CL interface and PEM/CL interface at anode, and how these designs lead to the performance improvement and cost reduction in PEMWE
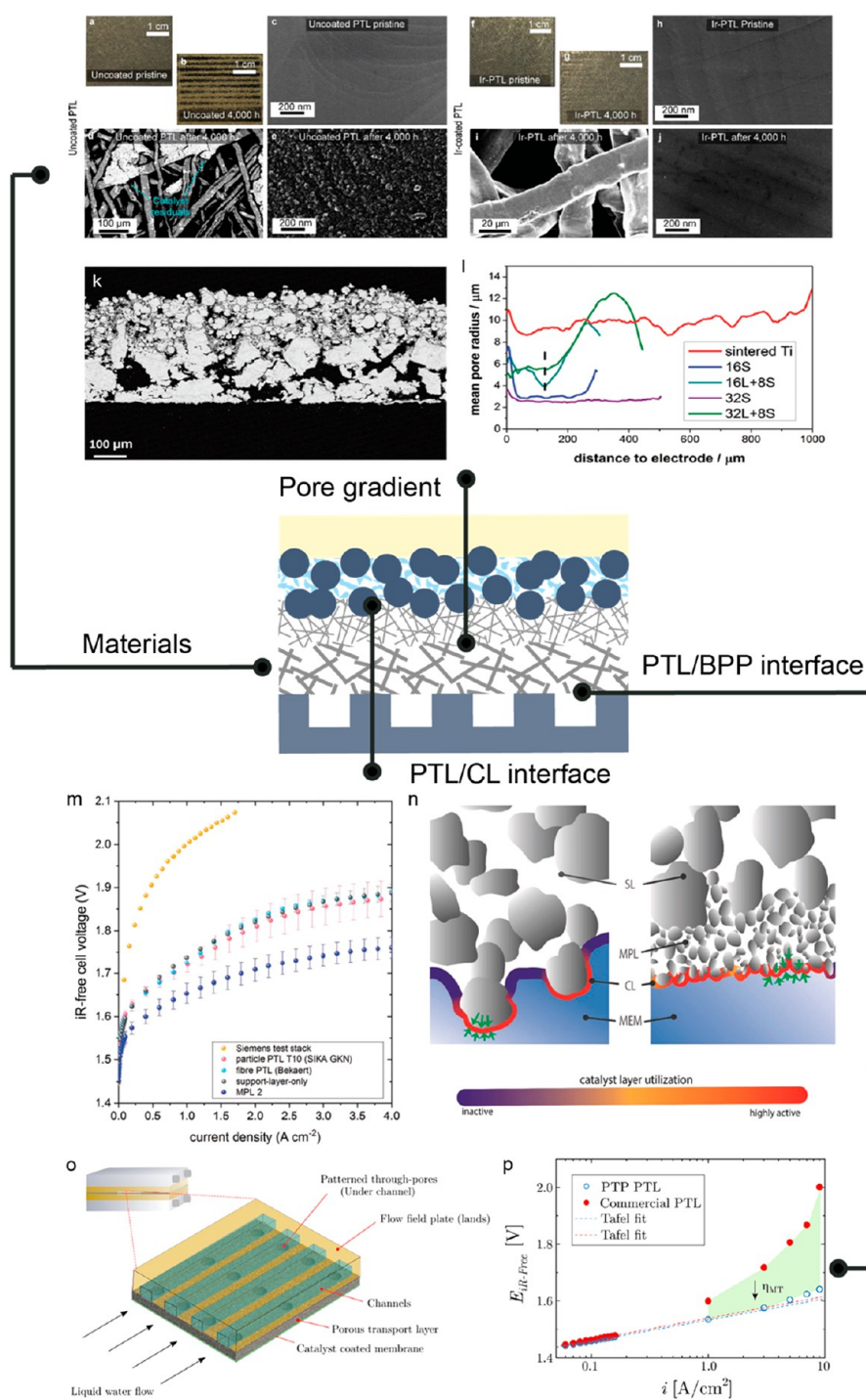
Figure 2. (a, b) Optical and (c−e) SEM images of uncoated PTL before and after 4000-h operation. (f, g) Optical and (h−j) SEM images of Ir-coated PTL before and after 4000-h operation. Reproduced with permission from ref 48. Copyright 2021 Wiley-VCH. (k) Cross-section SEM image of the 32L + 8S PTL. The PTL was fabricated by spraying 8 layers of small size (S) Ti particles on 32 layers of large size (L) Ti particles, which was designated as "32L + 8S". (l) Height-dependent pore diameters of single-layer and multilayer PTL. The distance to electrode refers to the pathway from CL side to BPP side. The boundary between small-particle layer and large-particle layer is shown with a dashed line. Reproduced with permission from ref 75. Copyright 2017 Royal Society of Chemistry. (m) *iR*-free polarization curves at 50 °C and 25 bar balanced gas pressure of PEMWE test stack (Siemens, Germany), and of laboratory cells at 10 bar balanced pressure with transport layers indicated of 1 mm thickness, Bekaert (NV Bekaert SA, Belgium) o.d. 20 μm fibers and 56% porosity and particle sintered PTL SIKA T10 (GKN Sinter Metals). (n) Schematic illustration of the microporous layer (MPL) effect showing the interfacial cross sections of mechanical deformation of CL and membrane for (left) the coarse support layer (SL) and (right) a multilayer PTL with fine structured MPL top layer. The catalyst utilization is depicted in color code from blue (inactive) to red (active). Local microscopic compression of CL by surface particles is indicated by green arrows. Reproduced with permission from ref 76. Copyright 2019 Wiley-VCH. (o) Schematic of the PTL with patterned through-pores (PTP) under the flow field channels. (p) The Tafel slope and *iR*-free cell potential for the PTP PTL and commercial PTL. The region in green indicates the reduction in mass transport overpotential due to the PTP PTL. Reproduced with permission from ref 79. Copyright 2020 American Chemical Society.

are summarized, which we believe will draw more attention to this field and also provide rational guidance for designing future PEMWE. To be specific, we will first discuss current understandings on PTL material, porous structure and transport properties, with emphasis on the characterization techniques and modeling methods of bubble evolution and two-phase transport dynamics. In the next section, a comprehensive summary of recent advances in interface engineering strategies and catalyst coating techniques for a better PEM/CL interface and PTL/CL interface will be presented. Finally, an outlook of future orientations to integrating the anode will be proposed, targeting to facilitate the designs of the next-generation PEMWE with higher performance and lower cost.

2. CURRENT UNDERSTANDINGS ON PTL MATERIAL, STRUCTURE AND, TRANSPORT PROPERTIES

PTL, as one of the major components and cost drivers in PEMWE, should serve at least the following functions: (1) robust mechanical and electrochemical stability under high pressure and harsh environments; (2) outstanding electrical conductivity between CL and BPP; (3) efficient management of reactant and product (i.e., water and O_2) transport; (4) superior thermal conductivity to dissipate heat from the catalytic sites. These functions put forward complex requirements on the material and structure of PTL for PEMWE. In this section, the state-of-the-art PTL materials will be summarized, followed by the discussion of the structure–function relationship of PTL, including pore size, porosity, thickness, and pore gradient. Also, current comprehension on the bubble evolution and two-phase transport dynamics through various experimental and modeling approaches will be gathered.

2.1. PTL Material. In conventional AWE and AEMWE with local alkaline environments, nickel- (Ni-) based materials (e.g., Ni mesh or foam) are generally employed as PTL.[43] However, for PEMWE, the highly acidic and oxidative environment at anode limits the use of cost-effective PTL materials with low corrosion potential, such as stainless steel, carbon-based and Ni-based materials.[25,26] Early studies have demonstrated that extensive corrosion was observed on a stainless steel mesh as anode PTL after operation in a PEMWE.[44,45] During the corrosion process, the iron (Fe) and Ni cations were found to migrate from anode CL to cathode CL through PEM, blocking the reaction sites and proton transport pathways in PEM, which led to performance failure.

For now, titanium (Ti) is the most widely used PTL material for PEMWE due to its high electrical conductivity and corrosion resistance.[25,26] However, aside from its high cost, uncoated Ti has other obvious disadvantages as the anode PTL material. Uncoated Ti-based PTL tends to form an adverse TiO_x passivation layer under harsh operation conditions in PEMWE, which will undergo further growth and surface dissolution, leading to a large increase in the ohmic resistance and cell voltage.[46,47] In addition, catalyst particles were reported to detach from the catalyst-coated membrane (CCM) and agglomerate on the surface of uncoated Ti-based PTL (Figure 2a–e), indicating that the degradation of other components in the electrolyzer (i.e., PTL in this case) can impair the stability of CL.[48] Therefore, to prevent the undesired passivation and degradation of Ti-based PTL materials, a protective noble-metal (e.g., platinum (Pt) or

gold (Au)) coating is usually applied, which adds to the total capital cost along with the expensive Ti metals.

In recent years, developing low-cost PTL, as well as BPP with the same material requirements, has received increasing attention. Attempts to lower or replace the precious-metal coating of PTL and BPP have been successfully made.[48−53] For example, Liu et al. utilized plasma sputtering to apply a skin Ir layer on Ti-based PTL with loading of 0.1 mg_{Ir} cm^{-2}, which was 10 times lower than the loading of typical Pt coating in commercial PEMWE.[48] After 4000-h continuous electrolysis at 2 V and 80 °C, negligible changes were observed on the morphology of Ir-coated PTL and cell performance (Figure 2f−j), suggesting the remarkable electrochemical stability of Ir coating and inhibition of Ti passivation. Recently, they further demonstrated through atomic force microscope (AFM) electrical conductivity measurements that the Ir coating on PTL also effectively reduced the loss of ionomer by 27% compared to the uncoated PTL, which was attributed to the greatly higher thermal conductivity of Ir than Ti and TiO_2.[54] The Ir-based coating can simultaneously serve as the catalytic sites, reducing the ohmic resistance between CL and PTL.[49] Corrosion-resistant Ti-based compounds, such as Ti_4O_7[51] and TiN,[52,53] were also investigated as promising alternative coatings. For instance, surface-nitrided Ti-based materials have been proven to possess high conductivity and corrosion resistance, which can be fabricated by thermal (gas) nitridation, plasma nitridation and electrochemical nitridation.[52,53]

Meanwhile, efforts have also been made to substitute cost-effective materials for the high-cost Ti bulk.[55−59] Notably, Stiber et al. displayed the prospective possibility to employ stainless steel as the base material for PTL and BPP.[55] By coating it with nonprecious niobium (Nb) and Ti via vacuum plasma spraying, the stainless steel based PTL showed almost no degradation under an accelerated stress test with intentional intermittent interruptions at 2 A cm^{-2} for more than 1000 h. No Fe contamination was observed and the cell performance recovered with 99% after refreshing and replacing the other components, suggesting the effective protection of the Nb/Ti coating against corrosion of stainless steel under aggressive environments in PEMWE. Copper was also investigated as the alternative bulk material with Nb coating for BPP, which exhibited outstanding anticorrosion properties and potential to be a low-cost PTL material.[59]

2.2. Porous Structure. Practical applications require PEMWE to operate at ampere-level, which makes the kinetic, ohmic, and mass transport resistance induced by PTL a nonnegligible impact on the cell performance.[60] Especially at low catalyst loadings, the bulk structural properties of PTL determine the ohmic and transport losses, while the PTL surface properties are mainly responsible for catalyst utilization and kinetic resistance (which will be described in detail in section 3.2, PTL/CL Interface Engineering).[61] Typically, an ideal trade-off should be achieved between mass transport properties, electrical contact, mechanical stability, and thermal conductivity when deciding PTL structure parameters, including pore size, porosity, tortuosity, thickness, and wettability.

To be specific, PTL with larger pore size and porosity can provide sufficient channels for gas removal, which will also cause an increase in ohmic resistance due to the inadequate conductive solid phase of PTL. The reduction in PTL thickness enhances electrical conduction and gas permeability,

but at the price of sacrificing mechanical stability. Therefore, the porous structure of PTL should be optimized according to specific cell configurations and operation conditions. For instance, Parra-Restrepo et al. prepared four sintered Ti powder PTL with a mean pore size of 3, 10, 35, and 60 μm, and porosity of 26%, 31%, 34%, and 37% to study the effects of PTL structural characteristics on the cell performance.[62] Through polarization curves and electrochemical impedance spectroscopy (EIS) results, PTL with a mean pore size of 10 μm and porosity of 31% exhibited the optimum performance, owing to its lower electrical and mass transport resistance. In addition, a low tortuosity in PTL can lead to enhanced interfacial contact between PTL and CL, as well as shortened travel distance for mass transfer.[63]

For PTL thickness, it is generally assumed that it determines the length of diffusion path for electrons, water and gas.[64] Nevertheless, some studies observed better cell performance on the thicker PTL, which might be caused by insufficient compression pressure or faster heat transfer.[65,66] Moreover, Weber and co-workers demonstrated that the optimal thickness is also related to the flow field design, which was approximately half of the flow field land size in their case.[66]

In terms of wettability, a hydrophilic and aerophobic PTL is generally thought to be favorable for water permeability and gas removal.[67] Kang et al. regulated the hydrophobicity of Toray papers via tuning the loading of polytetrafluoroethylene (PTFE) from 0% to 20%.[68] The activation, ohmic and diffusion resistance all displayed a significant increase as the PTL became more hydrophobic. Zhao et al. fabricated a superhydrophilic PTL through surface treatment of commercial Ti PTL.[69] Microfluidic experiments verified that the time for water saturation ($\sim$5 s) was $\sim$30 times shorter in the treated PTL with superhydrophilic features, which was responsible for the low oxygen saturation and over 11% reduction in cell voltage at current densities higher than 5 A cm^{-2}. Furthermore, hydrophilic/hydrophobic cooperative (i.e., amphiphilic) PTL and electrodes have been designed in polymer electrolyte membrane unitized regenerative fuel cells and water electrolyzers, which are very promising for rational management of water and gas flows.[70,71]

To effectively manage the water transport and gas removal at anode, designing pore gradients in PTL for PEMWE has been emerging as a promising strategy in recent years. The strategy is originally derived from the introduction of a microporous layer between CL and PTL in PEM fuel cells (PEMFC), which enables sufficient interfacial contact and facilitates mass transport.[72−74] In such a graded PTL structure, the pore size and porosity will gradually increase from the CL side to the BPP side, which can also lead to better cell performance in PEMWE. On one hand, the low tortuosity of PTL close to the CL side leads to an improved PTL/CL interface and mitigated membrane deformation, resulting in higher catalyst utilization and reactant supply. Lettenmeier et al. employed vacuum plasma spraying to fabricate pore-graded PTL via spraying different layers of titanium particles with small or large size (Figure 2k).[75] Height-dependent pore-size distribution calculated from X-ray computed tomography (CT) reconstructions showed a linear increase in mean pore radius from the dashed line in Figure 2l, which was regarded as the boundary between small-particle layer and large-particle layer. The resulting low tortuosity and capillary pressure enhanced water supply and gas evolution at 2 A cm^{-2}, contributing to high performance. Schuler et al. developed a hierarchically structured multilayer

PTL by cosintering fine and coarse Ti powders.[76] Compared with some commercially available Ti-based PTL and support-layer-only in this study, the novel multilayer PTL (MPL 2) displayed superior cell performance (Figure 2m), with an average 100 mV lower overpotential at 2 A cm^{-2}. The authors concluded that the low surface roughness of MPL 2 ensured a high interfacial contact area with CL, resulting in almost triple catalyst usage. Meanwhile, MPL 2 featured a homogeneous pressure distribution toward the PEM and CL, inhibiting the membrane deformation and distortion of CL caused by ionomer swelling (Figure 2n). Therefore, the less coarse surface allowed the use of thin membranes in the electrolyzer to further reduce the ohmic overpotentials. Stiber et al. produced a novel graded PTL structure by diffusion bonding of a Ti porous sintered layer on a Ti mesh, which offered effective two-phase transport and absolved the use of BPP with flow fields.[77] The enhanced mass transfer and elimination of the interface between Ti sintered layer and Ti mesh led to a 31% higher voltage efficiency at 4 A cm^{-2} than mesh-only PTL. However, when stacking two layers of Ti mesh with different pore diameters, due to their large pore sizes (>200 μm) compared with Ti powders and fibers (<60 μm), ohmic losses dominated the cell voltage over mass transport overpotential.[78] Through finite element methods, heterogeneous compression between the bilayer mesh PTL and CL was visualized, which accounted for the poorer performance when using mesh-based PTL with pore gradients.

On the other hand, large pore diameters and high porosity of graded PTL adjacent to the flow field facilitate gas removal, reducing mass transport overpotentials, especially at industrially relevant current densities. Lee et al. perforated commercial PTL to create patterned through-pores (PTP) under flow channels while retaining regular pores for water supply (Figure 2o).[79] Compared with the commercial PTL, the PTP PTL enabled a 4-fold reduction of mass transport overpotential from 150 mV to 37 mV at an ultrahigh current density of 9 A cm^{-2} (Figure 2p). Through in operando neutron imaging and subsecond X-ray synchrotron imaging results, a 43.5% decrease in gas saturation at PTL/CL interface and more frequent bubble growth and snap-off ($\sim$3.3 Hz) were revealed for the PTP PTL, indicating the remarkable enhancement of gas removal and water delivery rates. In addition, Kim and co-workers demonstrated that introducing large pores neighboring to BPP side in graded PTL can mitigate the mass diffusion losses induced from the coverage of small pores by the flow field lands, which blocks or prolongs the water transport pathway to the reaction sites under these lands.[80]

Except for optimizing the porous structure of PTL, developing cost-efficient advanced manufacturing technologies for large-scale PTL production (e.g., tape casting) is a prerequisite for next-generation PEMWE,[81,82] which is beyond the scope of this review.

2.3. Characterization Techniques and Modeling Methods for Bubble Evolution and Two-Phase Transport Dynamics Inside PTL.

The PTL/CL interface and porous structure of PTL will guide the bubble evolution process and transport pathway in PEMWE. Preferential oxygen pathways were observed in PTL with certain pore-size distribution and wettability, regardless of water flow rate, operating current density, and pressure.[83,84] The generated bubbles have complex effects on the cell performance, including activation overpotential, ohmic overpotential, and mass transport (or concentration) overpotential. Therefore, a
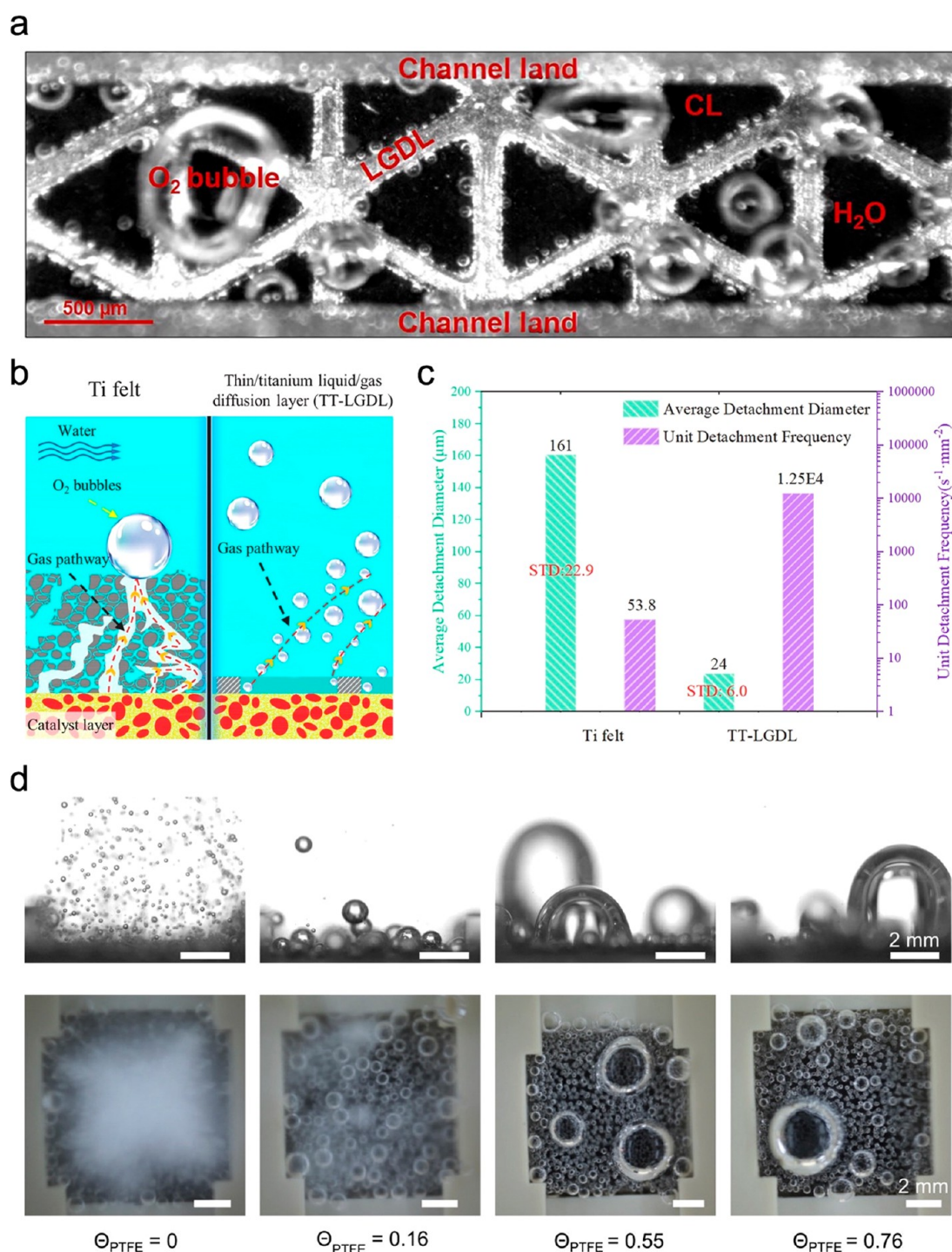
Figure 3. (a) Front-view image of oxygen bubble evolution in the PEMWE microchannel. Reproduced with permission from ref 37. Copyright 2016 American Association for the Advancement of Science. (b) Schematics of two-phase transport in Ti felt and TT-LGDL. (c) Comparison of bubbles dynamics between Ti felt and TT-LGDL in pore scale. Reproduced with permission from ref 90. Copyright 2021 Elsevier. (d) Side and top views of oxygen bubbles on porous Ni foam with PTFE coverage of 0, 0.16, 0.55, and 0.76. Reproduced with permission from ref 91. Copyright 2021 Elsevier.

deep understanding in bubble evolution and two-phase transport dynamics through advanced characterization techniques and modeling methods will in turn facilitate the rational designs of PTL.

During water electrolysis, a single bubble typically goes through four stages, namely nucleation, growth, detachment, and transport. The OER provides a continuous increase in the dissolved gas concentration near the catalytic surface, leading

to gas supersaturation, which propels heterogeneous bubble nucleation at favorable sites on CL.[85] The bubble growth is driven by the difference between the dissolved gas concentration near the catalytic surface and that surrounding the bubble. When the upward forces outweigh the downward forces, bubble detachment happens from a narrowing of the neck between the bubble and CL, with a remaining small gas pocket to start a new cycle of bubble growth and detachment.
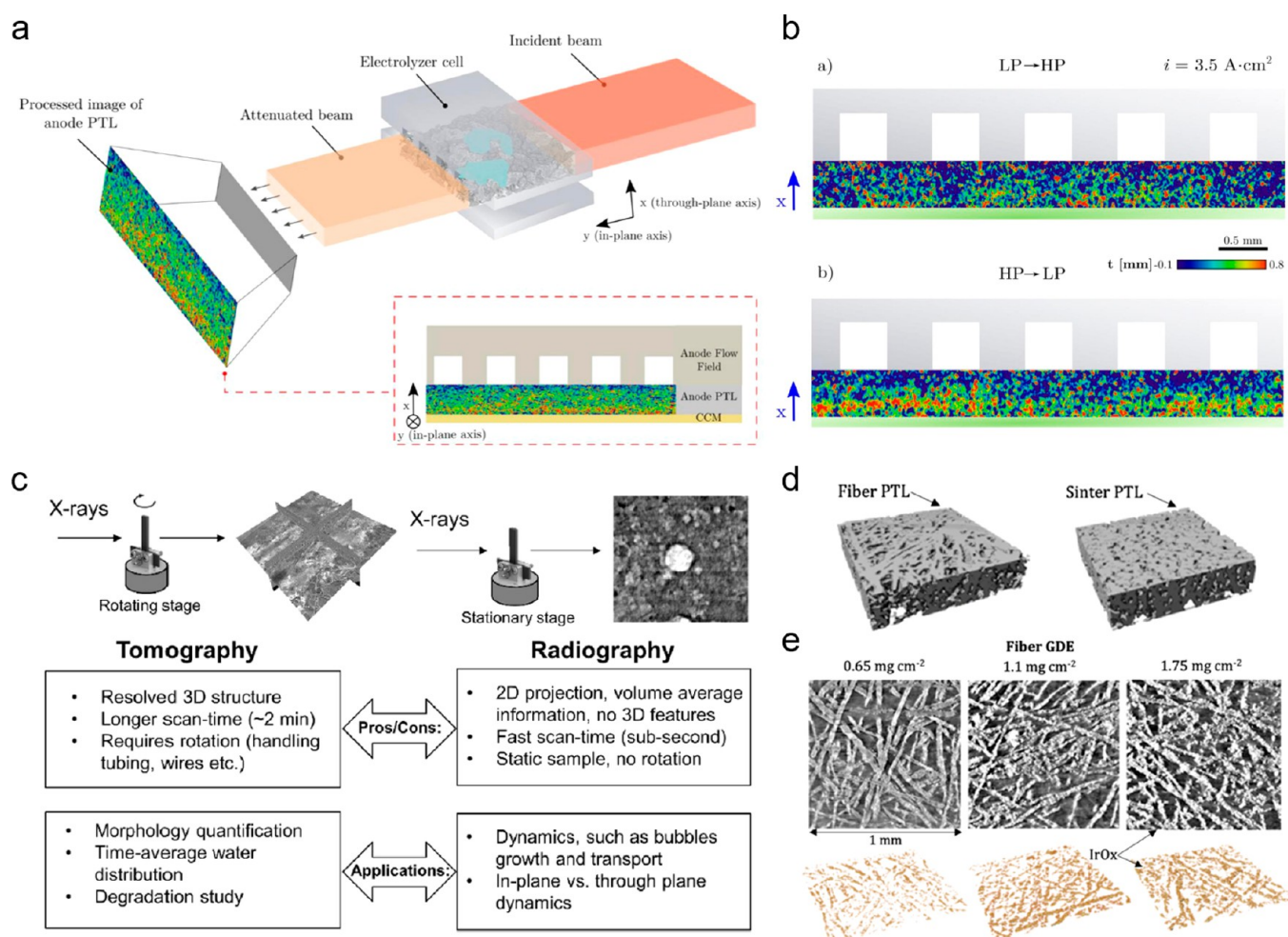
Figure 4. (a) Schematic of the in operando neutron imaging experiment setup. (b) The neutron radiographic image of the LP → HP (namely increasing the PTL porosity from PTL/CL interface to PTL/flow-field interface) and HP → LP PTL configuration acquired in operando. Reproduced with permission from ref 97. Copyright 2020 Elsevier. (c) Summary chart outlining the differences in imaging between X-ray CT and X-ray radiography as applied to electrolyzer imaging. Reproduced with permission from ref 98. Copyright 2018 Elsevier. (d) 3D renderings of fiber and sintered Ti PTL obtained from X-ray CT. (e) 2D reconstruction and 3D renderings of fiber Ti PTL and IrO$_x$ catalyst with various loadings in a gas diffusion electrode (GDE) configuration obtained from X-ray CT. Reproduced with permission from ref 104. Copyright 2022 Elsevier.

After that, the bubble will transport through PTL into the flow fields and be removed by the water flow. In practical PEMWE, the bubble evolution process involves multiple bubbles, which makes it a need to characterize average behavior instead of individual bubbles.

The cell voltage loss induced by the bubbles can be divided into activation loss, ohmic loss, and mass transport loss. The activation loss originates from the coverage of electrocatalytic surface areas by the attached bubbles. The ohmic loss is introduced by the blockage of ion transport pathways in the electrolyte. Additionally, bubbles attached on the surface of CL will impose an uneven current density distribution surrounding the bubbles, affecting the charge transfer.[86] For the mass transport loss, the evolution of bubbles reduces the dissolved gas concentration near the catalytic surface, thus decreasing mass transport overpotential. Also, the dissolved oxygen concentration gradients may be mitigated through convective flows caused by the bubble diffusion process.

Given the complicated influence of bubble evolution and transport, efforts have been made to understand these processes through various characterization techniques and modeling methods, including optical, neutron, and X-ray imaging, as well as computational studies. Through utilization of a high-speed camera and transparent flow fields, the bubble evolution and transport process can be visualized. Back in 2016, Mo et al. discovered that opposite to the conventional belief that OER will uniformly occur throughout the whole CL in PEMWE, the oxygen bubbles were exclusively generated at the interface of LGDL and CL (Figure 3a).[37] Preclusive experiment further validated that the bubble would not nucleate at the interface between CL and nonconductive wires, identifying the importance of excellent electron conduction for bubble generation. The bubble nucleation sites, growth rate, detachment diameter, and number were found to increase with the operating temperature and current density, while the water flow rate had limited influence.[87,88] At the channel scale, bubbly flow pattern was observed at a low current density, which transformed into slug and finally annular flow patterns at a higher current density, as bubble coalescence became more frequent.[89] The microscale visualization system was also used to study the difference of bubble dynamics on various PTL. For example, Wang et al. developed a novel thin/tunable liquid/gas diffusion layer (TT-LGDL), which exhibited greatly reduced large slugs unfavorable for
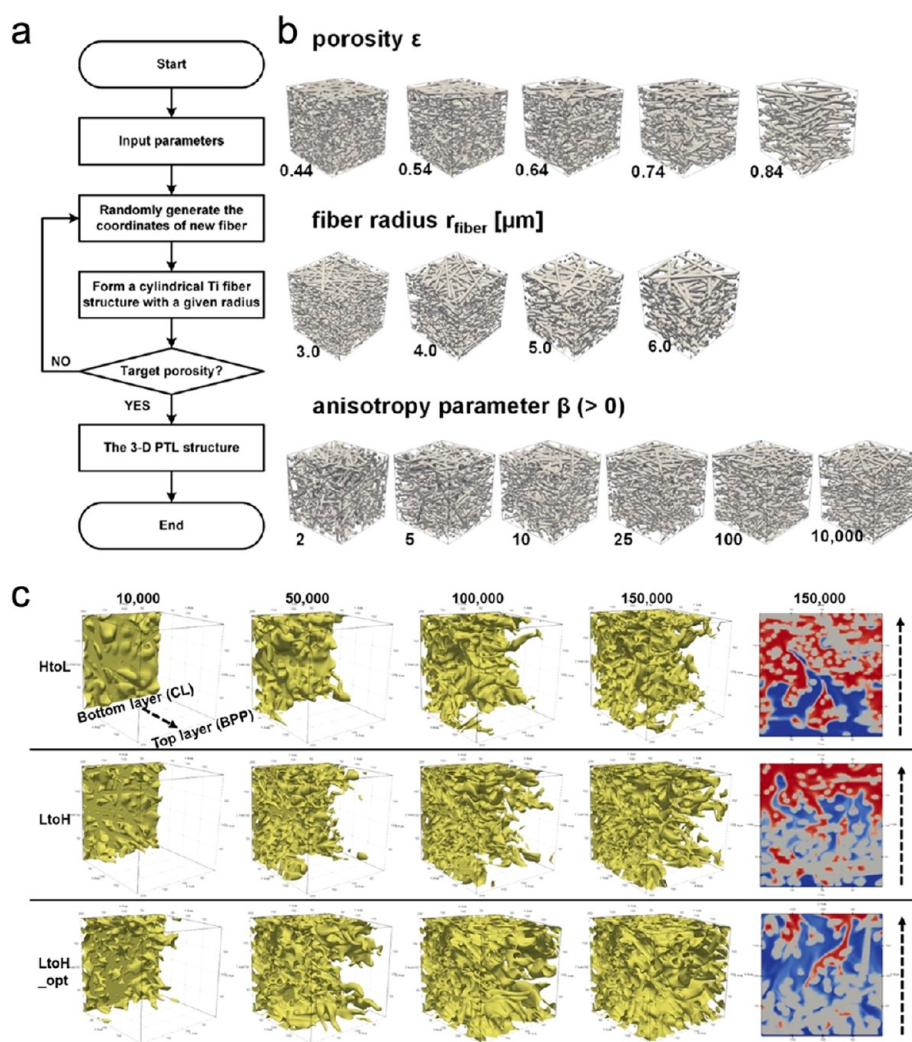
Figure 5. (a) Steps for a 3D PTL reconstruction. (b) 3D renderings of the reconstructed PTL with different porosity (ε), fiber radii (r_{fiber}), and anisotropy parameters (β). (c) The oxygen propagation processes and gas/water distribution of the graded PTL (HtoL, LtoH and LtoH_opt) at the 10000th, 50000th, 100000th, and 150000th simulation step. The yellow color represents oxygen. In the last column (gas/water distribution from bottom CL side to top BPP side), the blue color represents oxygen, the red color represents liquid water, and the gray color represents solid fibers. Reproduced with permission from ref 117. Copyright 2023 Wiley-VCH.

water supply compared with a conventional Ti felt PTL (Figure 3b).[90] The TT-LGDL showed a remarkably high bubble generation frequency (Figure 3c), which was 236 times higher than the Ti felt PTL, as well as a 6-times smaller average detachment diameter, indicating its strong capability for bubble production and removal. By changing the wettability of porous Ni foam through PTFE deposition, Iwata et al. observed that the enhancement in PTL hydrophobicity led to larger bubble sizes and higher bubble coverage (Figure 3d), thus inducing severe mass transport losses.[91] As the bubble diameter increases, the bubble evolution mode transitioned from the internal growth and departure mode (bubble diameter < pore diameter) to the wicking mode (bubble diameter ≈ pore diameter) and gas-filled mode (bubble diameter > pore diameter), where frequent bubble coalescence occurred and bubble removal from internal pores was inhibited. Due to the compact structure of PEMWE, the limitation of current optical imaging lies in the incapability to characterize the bubble evolution process at CL and PTL/CL interface, as it often reflects the bubble behavior coming out from PTL.[85]

Neutrons can provide high sensitivity toward H_2 and water, as well as fair spatial resolution, making neutron radiography a powerful tool to study the gas/water distribution and its dynamic changes in PEMWE.[92−94] For instance, Seweryn et al. utilized neutron imaging to visualize through-plane water distribution at anode in a steady state, which showed a constant equilibrium between reactant and gas transport at a wide range of current density from 0.1 A cm^{-2} to 2.5 A cm^{-2}.[95] Maier et al. employed in-plane neutron radiography to observe significant inhomogeneity in water thickness across the active area, highlighting the need for PTL structure and flow field geometry optimization.[96] Combining the obtained water distribution with PTL structural information acquired from X-ray CT results, the authors found that a non-negligible number of pores were not utilized for water transport, which limited the active area and cell performance. Through in operando neutron imaging (Figure 4a), Lee et al. demonstrated the benefits of deploying a spatially graded PTL fabricated via vacuum plasma spraying.[97] The neutron imaging results revealed that the gas saturation near PTL/CL interface for the LP → HP (low porosity to high porosity from PTL/CL

interface to PTL/flow-field interface) configuration was one-half of that for HP → LP (high porosity to low porosity from PTL/CL interface to PTL/flow-field interface) configuration (Figure 4b), which was responsible for its 38% lower mass transport overpotential. These representative examples exhibit the wide potential of neutron radiography for the understanding of two-phase transport dynamics and also the evaluation of novel PTL designs.

X-ray CT and radiography are other common and nonintrusive characterization techniques for the visualization of two-phase transport process in PEMWE. It should be noted that carbon-based PTL are more preferred for X-ray imaging tests owing to the strong X-ray attenuation ability of Ti (about 2 orders of magnitude higher than that of carbon-based materials). X-ray CT provides three-dimensional (3D) information, enabling PTL morphology quantification and time-average water distribution study, which also requires a long scanning time (~2 min) and rotation (Figure 4c).[98] For X-ray radiography, the subsecond scanning time allows the capture of dynamic bubble evolution, which however is two-dimensional and volume-averaged. Leonard et al. observed some water-free voids inside anodic PTL from X-ray CT results, in agreement with the neutron radiography results mentioned above.[95,98] They further utilized X-ray radiography to characterize transient bubble formation and transport in a subsecond scale at various current densities. From the through-plane direction, Kim et al. used X-ray radiography to elucidate that PTL with through-pores under the lands of flow field contributed negatively to gas removal and water supply in the anode.[99] For Ti-based PTL, De Angelis et al. employed a staining agent to improve the X-ray absorption of water for a higher gas/water contrast, thus permitting oxygen pathway visualization in practically used Ti materials.[100]

Moreover, X-ray CT can easily separate solid from pores through image processing, enabling the investigation of PTL morphology and PTL/CL interface.[101−103] For example, through X-ray CT, Kulkarni et al. visualized fiber and sintered Ti PTL structures (Figure 4d), as well as PTL/CL interfacial regions with various catalyst loadings in CCM and gas diffusion electrode (GDE) configurations (Figure 4e).[104] For the GDE configuration with fiber Ti PTL, the catalyst distribution was determined by the surface morphology of PTL and catalyst loadings from the 3D volume rendering of the CL. Due to the resolution limitation, particles with diameters smaller than 1 μm cannot be imaged by X-ray micro CT. Recently, Bierling et al. characterized the through-plane catalyst distribution in a spray-coated GDE configuration via X-ray CT.[105] The surface roughness of the spray coated PTL was observed to be nearly unchanged, except for some big catalyst droplets. Through analysis of the through-plane gray-value gradient, the porosity gradient and CL thickness were estimated, and a maximum of ionically well-connected catalyst in the reported system was calculated to be 60%.

Other visualization techniques were also employed to characterize PTL morphology, PTL/CL interface and two-phase transport dynamics in PEMWE and PEMFC.[33,36,106] Hegge et al. utilized focused ion beam-scanning electron microscope (FIB-SEM) tomography to reconstruct the anode CL.[107] In PEMFC, cryo-SEM and a freezing method were used to directly observe water accumulation in ice form at the PTL/CL interface, which allowed the investigation of mass transport difference in two electrode fabrication methods (CCM and GDE).[108]

To map the local gas/water distribution inside PTL which is experimentally difficult, numerical modeling methods have been developed at different scales.[109−114] For PTL reconstruction, the microstructure data can be acquired from X-ray CT experiments or stochastically generated by algorithm through the input of various structural parameters.[115,116] Liu et al. conducted stochastic reconstruction of PTL in MATLAB with different porosity, fiber radius and anisotropy parameter (Figure 5a,b).[117] After the input of parameters, fibers with the corresponding radius are created in the selected matrix domain size to achieve the target porosity.

In PEMWE, common modeling methods of two-phase flow involve the volume of fluid (VOF) method, pore network modeling (PNM) and lattice Boltzmann method (LBM). The VOF method is capable of gas/water interface tracking and includes surface tension and wall adhesion effects on the macroscopic scale.[118] Arbabi et al. used the VOF method to simulate the gas/water interface movement inside PTL, which agreed well with previous experimental results.[119] The PNM regarded PTL as a network of pores connected by throats, which greatly decreased the computational load due to the discretization of the continuum model, making it a powerful pore-scale simulation tool. For instance, by implementing PNM, Lee et al. revealed a trade-off between gas/water permeability and contact resistance (or surface roughness) through the variation of precursor powder diameter and PTL porosity.[120] The limitation of PNM is that the simplified pore network also leads to the weakening of several important invasion phenomenon, such as capillary valve effect and Haine jumps.[110] The LBM is a promising mesoscopic simulation tool, which includes interparticular forces between molecules at microscale and functions as a Navier−Stokes solver at macroscale.[121] Recently, Liu et al. studied oxygen transport in PTL with different structural characteristics via LBM simulations.[117] They further reconstructed spatially graded PTL noted as LtoH and HtoL, which mean the directionality of the porosity gradient from CL side to BPP side (low-to-high and high-to-low porosity), as well as another graded PTL denoted as LtoH_opt with the same porosity as LtoH but a different fiber radius and orientation based on the modeling results. The LBM simulation results visualized that oxygen preferentially accumulated at the junction between the high porosity layer and the low porosity layer for the HtoL PTL, while a low-to-high porosity gradient facilitated the oxygen propagation process (Figure 5c). Higher efficiency and more transport pathways were observed on LtoH_opt PTL, indicating its stronger gas removal capability, which suggested an optimal fiber orientation angle of 30−45° to the in-plane.

Other modeling methods include molecular dynamics, finite element method, and cohesive zone model, which were applied for two-phase transport investigation in PEMFC.[106] The development of advanced simulation techniques allows the study of gas/water distribution inside PTL with various structural characteristics, providing abundant information about PTL transport properties.

3. ANODE INTERFACE ENGINEERING

Proper engineering of the two interfaces in PEMWE anode, namely PEM/CL interface and PTL/CL interface, can be crucial to the performance advancement of the whole cell.[34,122] Mass transport includes oxygen and water transport in PEMWE anode, both of which happen at the PTL/CL interface.[92] Electron transfer also occurs at PTL/CL interface,
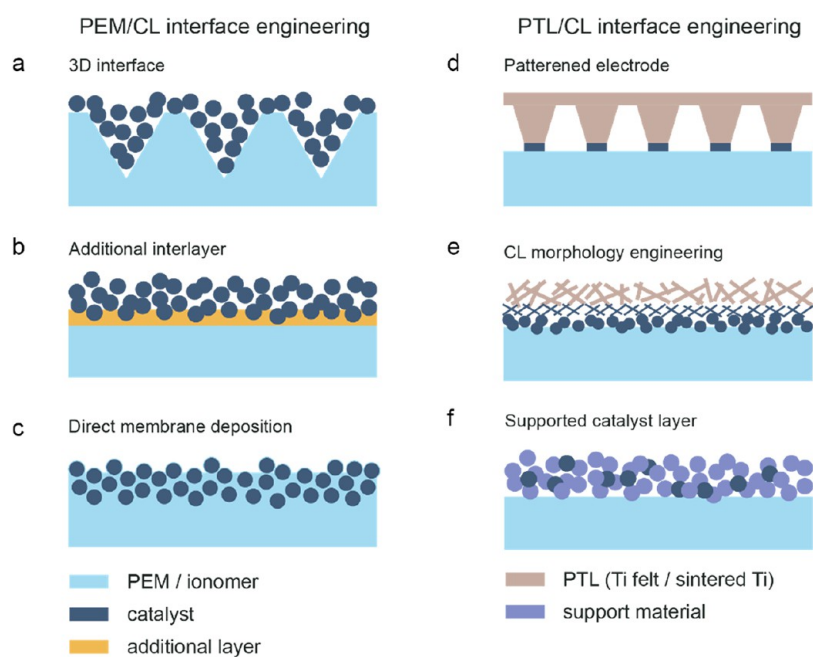
Figure 6. Schematic illustrations of the interface engineering strategies for PEMWE anode.
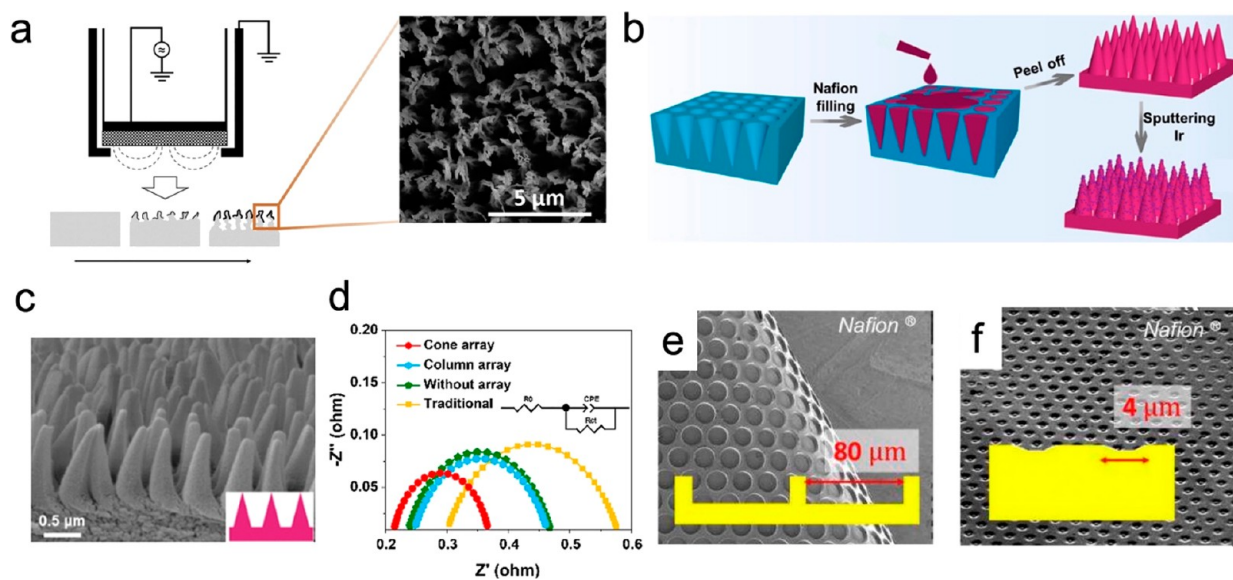

Figure 7. (a) Schematic illustration of surface etching and deposition of a PEM surface and the corresponding top-view SEM image. Reproduced with permission from ref 130. Copyright 2020 Elsevier. (b) Schematic illustration of step synthesis of ordered cone-like Nafion array. (c) SEM image of cone-structured Nafion array. (d) EIS comparison of MEA with various Nafion array morphology. Reproduced with permission from ref 131. Copyright 2023 American Chemical Society. (e, f) SEM images of micropatterned Nafion membrane surface with different pore sizes and depths. Reproduced with permission from ref 132. Copyright 2017 IOP Publishing.

while proton transfer takes place at PEM/CL interface.[20] More importantly, the PEM/CL interface has to keep strong adhesion during operation, otherwise CL delamination can result in cell failure.[106,123,124] Notably, in order to lower capital cost, the requirement of lower precious metal loading further brings challenges to rational interfacial designs.[61,125−127] In this section, various approaches of anode interface engineering in PEMWE will be classified and discussed (Figure 6).

3.1. PEM/CL Interface Engineering. *3.1.1. 3D Interface.* Conventionally, PEM/CL interface has a two-dimensional (2D) structure. The inadequate contact between PEM and CL leads to low catalyst utilization, high contact resistance,

sluggish charge transport, and poor interface stability.[128,129] To overcome these issues, various approaches have been reported to construct a 3D interface at PEM/CL interface (Figure 6a).

PEM surface modification is a straightforward way to construct 3D PEM/CL interface. For instance, Hrbek et al. proposed an innovative sputter-etching treatment for PEM (Figure 7a).[130] To be specific, by utilizing magnetron sputtering to etch the PEM and depositing CeO$_x$ support simultaneously, the surface of PEM was turned into a fiber-like structure of robustness, dramatically increasing the PEM/CL interfacial area. This fine 3D interface enabled an ultralow Ir
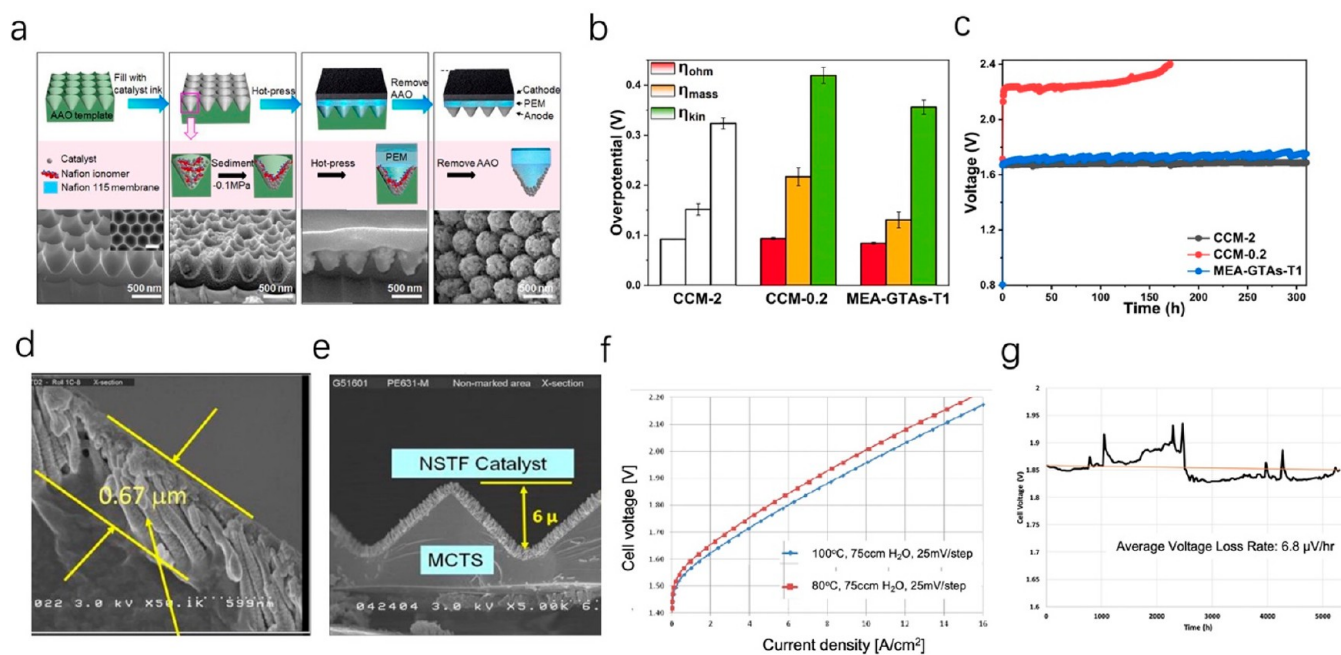
Figure 8. (a) Schematic illustration and corresponding SEM images of fabrication process of ordered MEA anode with tapered array. (b) η_{kin}, η_{Ohm}, and η_{mass} of CCM-2, CCM-0.2, and MEA-GTAs-T1 at a high current density of 2 A cm^{-2}. CCM-2 and CCM-0.2: conventional CCM with 2 and 0.2 mg cm^{-2} of Ir loading. MEA-GTAs-T1: optimal MEA with GTAs. (c) Stability test of the conventional MEAs with 2 mg cm^{-2} or 0.2 mg cm^{-2} of Ir loading and MEA with GTAs at 1 A cm cm^{-2} and 65 °C. Reproduced with permission from ref 133. Copyright 2022 American Chemical Society. (d) Cross-sectional SEM of NSTF electrode after transferred to PEM surface, showing maintained nanowire structure and an intimate interface. (e) Cross-sectional SEM of NSTF electrode grown on MCTS. Reproduced with permission from ref 134. Copyright 2012 IOP Publishing. (f) Polarization curves of MEA with Ir NSTF anode at 100 °C (blue) and 80 °C (red), ambient pressure. (g) Durability test at 2 A cm^{-2} for 5000 h of MEA with Ir NSTF anode, with anode Ir loading 0.25 mg cm^{-2}, Nafion N115 membrane at 80 °C, and ambient pressure. Reproduced with permission from ref 135. Copyright 2015 IOP Publishing.

loading of only 113 μg cm^{-2} and improved electrochemical surface area (ECSA) by 130% compared to the smooth PEM/CL interface without sacrificing ohmic resistance.

To construct a 3D PEM/CL interface, another approach is to directly fabricate PEM with a patterned surface. Tian et al. built a layer of ordered cone-like Nafion array on top of commercial Nafion 115 membrane utilizing an anodic aluminum oxide (AAO) template and sputtered Ir of 20 μg cm^{-2} on top of the cone structure (Figure 7b).[131] The dense layer of sputtered Ir on the enlarged PEM surface enabled effective proton transfer and durable PEM/CL interfacial contact (Figure 7c), yielding extremely high mass activity of 168 A mg$_{Ir}^{-1}$ cm^{-2} at 2.0 V that is superior than most of the reported values. The EIS analysis of MEA with cone Nafion array was also compared to MEA consisting other anode structures (Figure 7d). It was found that the ohmic resistance of MEA with cone array was over 30% lower than that of MEA with traditional configuration, signifying the enhanced contact at PEM/CL interface. Similarly, Zhang et al. proposed a versatile and simple way to engineer micropatterned PEM/CL interface through polydimethylsiloxane (PDMS) soft lithography.[132] PDMS elastomer gel was cured on top of silicon wafer with micropattern, forming a PDMS mold after peeling off. Nafion dispersion was then drop-casted on the PDMS mold and dried to shape. Various pore sizes (2 to 80 μm), pore depths (0.5 to 20 μm), and pore shapes can be easily achieved using this method (Figure 7e, f). A membrane as large as 80 cm^2 was also successfully manufactured, revealing the potential for large-scale production. Regarding the electrochemical performance, the PEMWE with micropatterned Nafion

membrane showed lower onset potential than pristine membrane which can be explained by the larger interfacial area and more exposed active sites.

It is also viable to fabricate CL on a substrate with high surface area first and then transfer CL to PEM surface for a 3D PEM/CL interface. For example, Dong et al. proposed a novel nanoimprinting approach to structure an ordered MEA anode with gradient tapered array (GTA) in PEMWE (Figure 8a).[133] By drop-casting anode catalyst ink onto an AAO template with tapered pores, a thin CL was formed at the surface of pores. Subsequently, PEM and AAO template were hot-pressed together, creating a robust 3D interface with enlarged surface area. Compared to conventional electrolyzer with the same Ir loading, both ohmic resistance and charge transfer resistance evidently dropped for the MEA with GTAs (Figure 8b), owing to the enhanced contact and improved transport at PEM/CL interface. As a result of larger interfacial area and higher catalyst utilization, with only 0.2 mg cm^{-2} of Ir in anode CL, the electrolyzer with 3D interface can maintain good stability running at 1 A cm^{-2} for over 300 h, which is comparable to a conventional electrolyzer with 2 mg cm^{-2} Ir (Figure 8c). A similar case is the nanostructure thin film (NSTF) electrode developed by 3M company.[134,135] The NSTF electrode possesses a core–shell nanowire array structure, in which the core is an organic photoconductor that is resistant to electrochemical corrosion. Ir shell of ~0.25 mg cm^{-2} was sputtered onto the organic core array. When transferred from substrate to PEM surface, the NSTF electrode partly extruded the PEM surface, constructing a robust and intimate PEM/CL interface (Figure 8d).[134] Additionally, since NSTF electrode
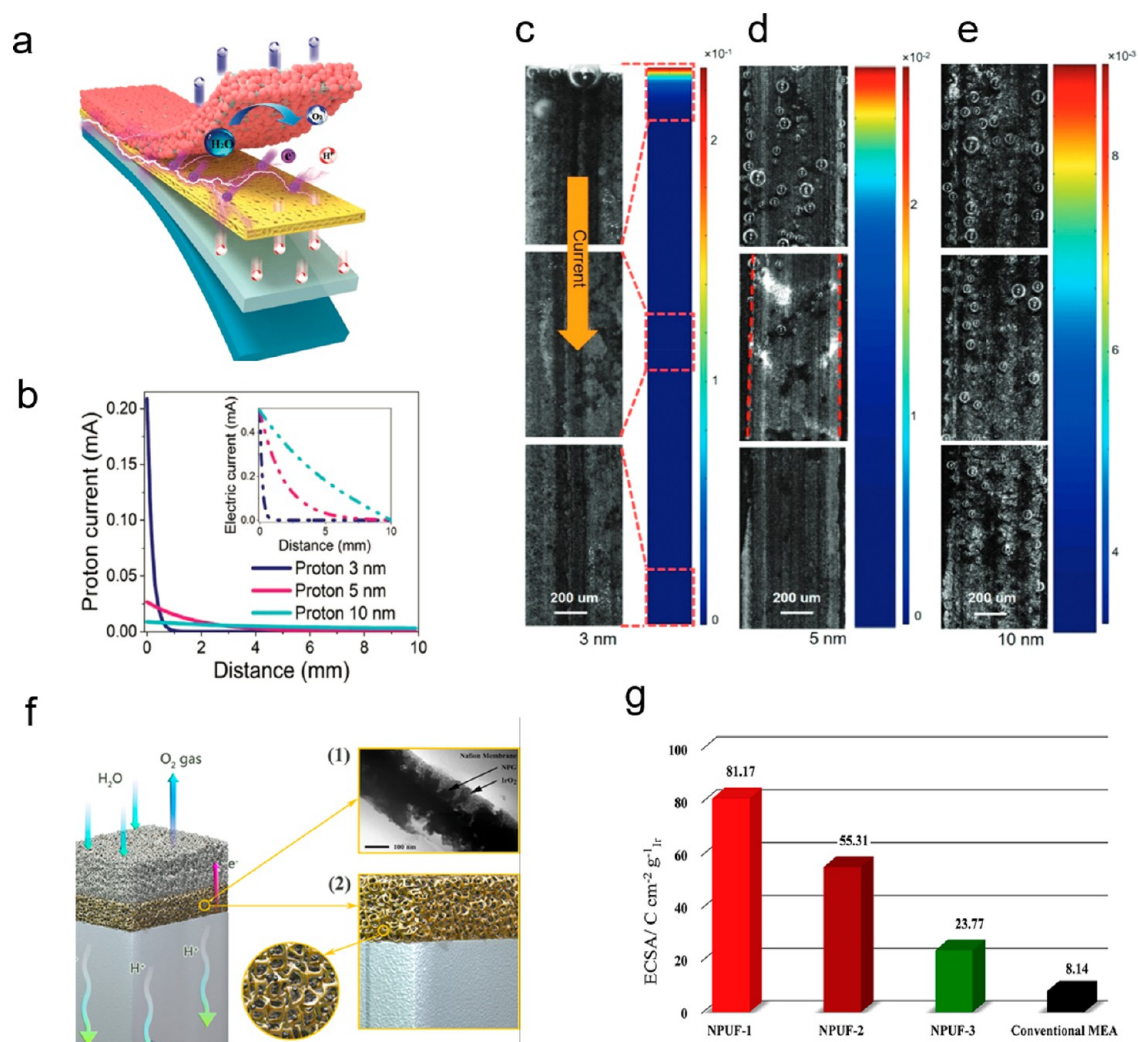
Figure 9. (a) Schematic illustration of PEMWE electrode with AuNL. (b) Proton current distribution along the electrodes with AuNL of various thickness. Inset: electric current distribution along the electrodes with AuNL of various thickness. (c–e) Visualization of active OER sites and current distribution along electrode with (c) 3 nm AuNL, (d) 5 nm AuNL, and (e) 10 nm AuNL. Reproduced with permission from ref 137. Copyright 2020 Wiley-VCH. (f) Schematic illustration of anode electrode consisting of gold/IrO$_2$ NPUF. Insets: structure of gold/IrO$_2$ NPUF. (g) Comparison of specific ECSA between NPUF electrodes and conventional MEA. NPUF-1, NPUF-2, and NPUF-3 were calcinated at 450, 500, and 600 °C. Reproduced with permission from ref 138. Copyright 2017 Elsevier.

was grown on a special substrate, namely microstructured catalyst transfer substrate (MCTS) as shown in Figure 8e, the electrode surface can be further enlarged by $\sqrt{2}$. This special electrode structure showed superior durability of over 5000 h at 2 A cm^{-2} without obvious degradation as well as a high activity of 16 A cm^{-2} at 2.2 V (Figure 8f, g).[135]

3.1.2. Additional Layer. Apart from constructing a 3D patterned PEM/CL interface, incorporating an interlayer between PEM and CL presents a practical way to optimize the interface (Figure 6b). In an earlier study, Song et al. found an additional Nafion layer between PEM and CL can enhance the performance of PEMWE in several ways.[136] As Nafion layer penetrates into CL, a rougher and broadened interface is established, which further results in facilitated proton transport performance at the interface. It is worth mentioning that the Nafion interlayer also contributes to the enhanced interface mechanical stability as Nafion works as a strong binder between CL and PEM, eliminating delamination after stability test.

While the additional Nafion layer contributes to enhanced PEM/CL interfacial mechanical stability and proton transport, Nafion is not a good medium for electron transport. Yang et al. integrated a highly conductive gold nanolayer (AuNL) consisting of gold nanoclusters (AuCL) as proton and electron transport "highways" in between PEM and anode CL in PEMWE (Figure 9a).[137] The AuCL was sputter-coated on Nafion membrane and the thickness of this interlayer was highly adjustable. Conventionally, due to the low in-plane conductivity of anode CL, only the catalyst that is in contact with the LGDL can be real active sites during reaction. This not only leads to low catalyst utilization, but causes a higher overpotential as well. After introducing the highly active gold interlayer, the enhanced in-plane electron transport turned the active sites in anode from 1D (edge of LGDL) to 2D. The simulated proton current and electric current (Figure 9b) suggesting that the current distribution was most homogeneous with 10 nm of AuNL. This phenomenon was further directly visualized with a high-speed, microscale visualization system, as shown in Figure 9c–e. In Figure 9c, bubbles only
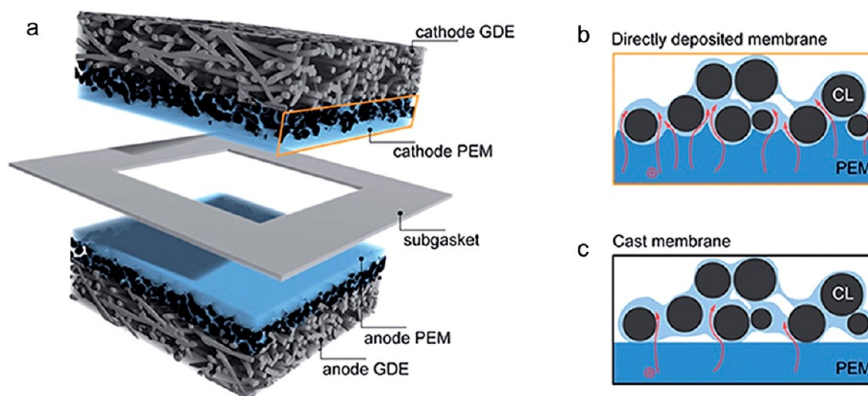
Figure 10. (a) Schematic illustration of a fuel cell MEA fabricated by DMD. Schematic illustration of the cross-section of PEM/CL interface (b) fabricated by DMD and (c) in a conventional MEA with cast membrane. Reproduced with permission from ref 139. Copyright 2015 Royal Society of Chemistry.
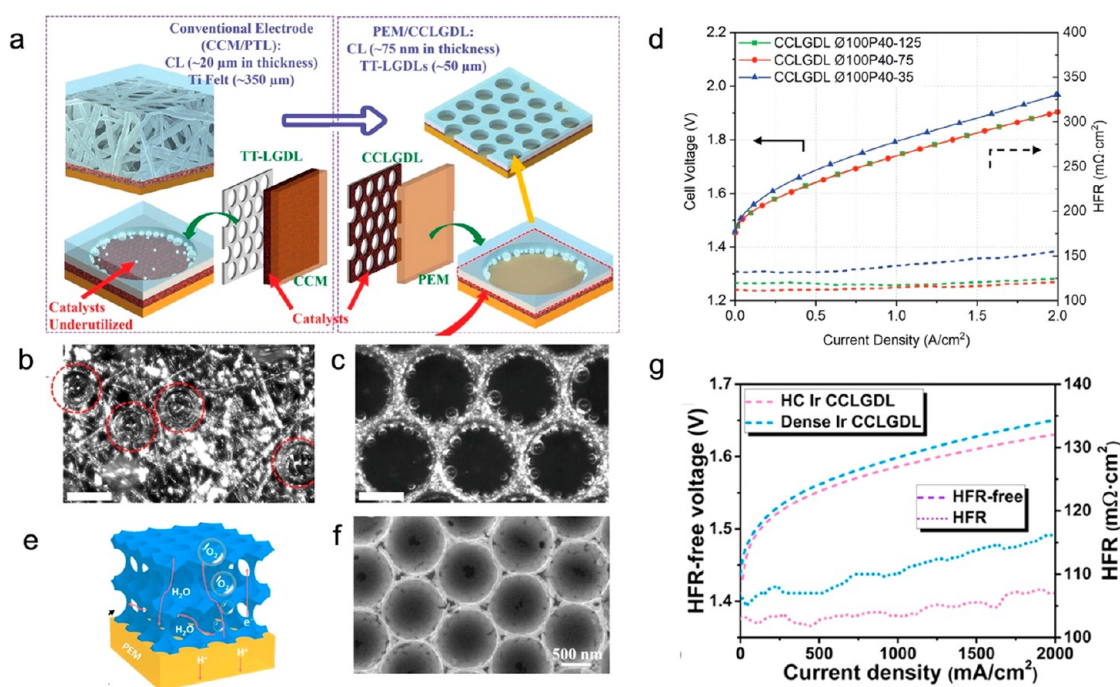

Figure 11. (a) Schematic illustration of the improved catalyst utilization from traditional CCM/PTL MEA structure to CCLGDL. (b, c) High speed video snapshots of (b) Ti felt GDL and (c) CCLGDL during OER process. Scale bar: 200 μm. (d) Polarization curves and HFR of CCLGDL of various Ir CL thickness (namely 35, 75, and 125 nm) at 80 °C. Reproduced with permission from ref 143. Copyright 2022 Wiley-VCH. (e) Schematic illustration of the honeycomb-like Ir CL. (f) SEM image of the honeycomb-like Ir CL. (g) HFR-free potential and HFR of CCLGDL with dense Ir CL and honeycomb-like Ir CL in current density range of 0−2000 mA cm^{-2}. Reproduced with permission from ref 144. Copyright 2023 American Chemical Society.

appear on top of the electrode near the current supplier connector, indicating lower catalyst utilization when AuNL is 3 nm. In contrast, bubbles are generated throughout the whole electrode with 10 nm of AuNL (Figure 9e), emphasizing the importance of proper AuNL thickness for boosting in-plane electron transfer. In addition to in plane-conductivity, proton transport was also enhanced because of the straight mesoporous structure in AuNL.

Similarly, an approach to combine nanoporous gold in anode CL to establish a strong interface between gold and PEM was also proposed.[138] Unlike the gold interlayer in previous mentioned research that stood as a nanohighway for protons between CL and PEM, a gold/IrO$_2$ nanoporous ultrathin film (NPUF) of 125 nm was playing the role of anode

catalyst layer here. The extremely thin NPUF shortened the migrate distance for protons and water molecules to travel between PEM and PTL, thus accelerating both mass transport and charge transfer. The composite film was synthesized by a thermal decomposition method and IrO$_2$ particles were found to be well dispersed on the skeletons of nanoporous gold (Figure 9f), which led to greatly enlarged ECSA (Figure 9g).

3.1.3. Direct Membrane Deposition. In a PEMWE, a precast membrane is typically an integral component, no matter catalyst is coated onto it to form a CCM or it is sandwiched between two GDEs. Back in 2015, Klingele et al. first reported a direct membrane deposition (DMD) method for PEMFC by simply inkjet-printing Nafion ionomer layer on top of the CL of two GDE and then assembling them with
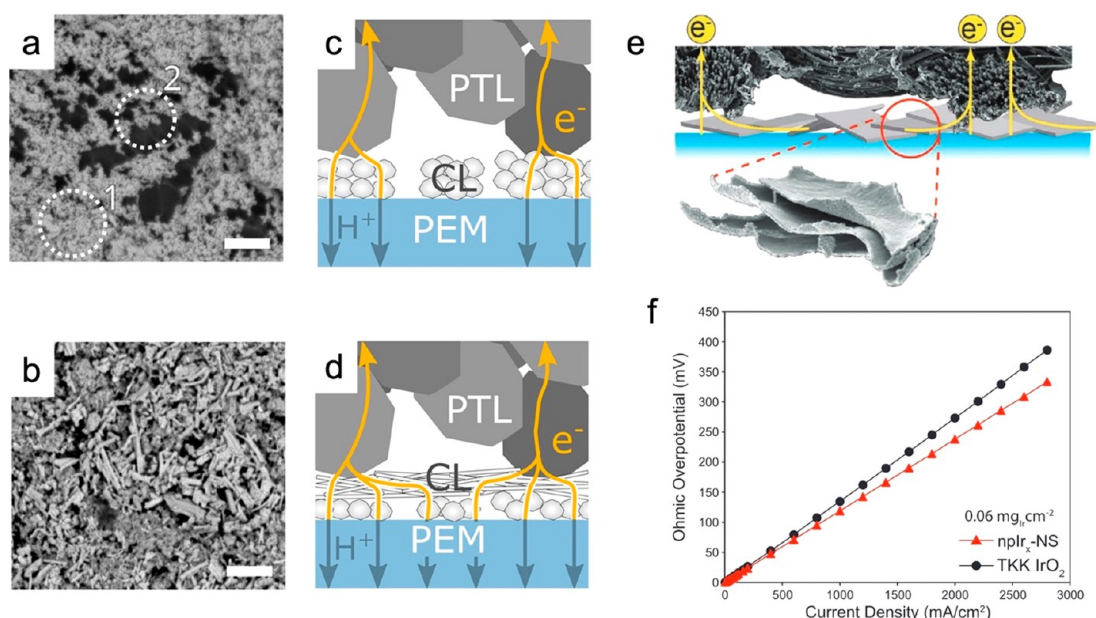
Figure 12. (a) Top-view of Ir nanoparticle CL with (1) inhomogeneous regions and (2) isolated catalyst island. Scale bar is 2 μm and the catalyst loading is 0.2 mg_{Ir} cm^{-2}. (b) Top-view of CL with Ir nanofiber interlayer. Scale bar is 2 μm and the catalyst loading is 0.2 mg_{Ir} cm^{-2}. (c, d) Schematic illustration of charge transfer of (c) regular nanoparticle CL and (d) CL with Ir nanofiber interlayer. Reproduced with permission from ref 147. Copyright 2020 American Chemical Society. (e) Schematic illustration of npIr-NS CL and the enhanced charge transfer. (f) Ohmic overpotential of npIr-NS and commercial IrO_2 at 0.06 mg_{Ir} cm^{-2}. Reproduced with permission from ref 148. Copyright 2021 Wiley-VCH.

Nafion layer facing each other (Figure 10a).[139] It was found that PEM fabricated through DMD can fill the surface holes of CL, reducing the gas crossover and lowering the ionic contact resistance at PEM/CL interface by 40% owing to the enlarged interface area and reduced gaps between catalyst and PEM (Figure 10b, c).[140] This method was later applied to AEMWE as well and successfully built robust AEM/CL interface that was stable for more than 600 h at 1 A cm^{-2}.[35] The DMD approach was also reported to be applied to PEMWE, yet only at the cathode side.[141] The inkjet-printed PEMWE demonstrated obvious reduced kinetic and ohmic resistance compared to the GDE configuration and had a similar performance to the CCM configuration.

To construct a PEMWE completely with DMD approach, a major problem is caused by the big pores in widely used Ti felt or sintered Ti PTL. Fortunately, this may be solved by the development of a micro porous layer (MPL) between PTL and CL. The smaller surface-near pores in MPL will enable the fully blockage of pores by a thin layer of catalyst and make it possible for DMD at anode in future PEMWE designs.[142]

3.2. PTL/CL Interface Engineering. *3.2.1. Patterned Electrode.* In order to maximize catalyst utilization, Yu et al. developed an innovative anode design of catalyst-coated liquid/gas diffusion layer (CCLGDL),[143] as shown in Figure 11a. The LGDL here was an ultrathin Ti layer (~50 μm) with tunable pore size and porosity. The CL and PTL were integrated by electrodepositing a thin layer of Ir (~75 nm) onto the surface of LGDL. This PEMWE reached a current density of 2 A cm^{-2} at 1.97 V, which was comparable to a conventional PEMWE with much thicker Ti felt PTL and a much higher Ir loading of 3 mg cm^{-2} in a CCM configuration. The catalyst utilization in the CCLGDL design was 24 times higher than that in the conventional design, in accordance with the previous finding that only the catalyst adjacent to PTL can be actually utilized during reaction,[37] as evident in Figure 11b, c captured by a high-speed camera. The authors also found the

CCLGDL with Ir layer thinner than 75 nm delivered slightly worse performance in cell voltage and high frequency resistance (HFR), while increasing Ir thickness beyond 75 nm would not improve the performance (Figure 11d), further emphasizing that active OER sites are much more concentrated near the PTL/CL interface than in bulk CL.

Furthermore, the CCLGDL can be improved with advanced CL structures other than the dense deposited CL, such as the honeycomb Ir layer of high porosity (Figure 11e, f) synthesized via a facile electrodeposition process on a polystyrene bead sacrificing template.[144] Compared to CCLGDL with dense Ir CL, the CCLGDL with honeycomb Ir CL exhibited both lower HFR and lower HFR-free cell potential (Figure 11g), implying an overall improvement in ohmic loss, diffusion loss and activation loss.

3.2.2. Catalyst Layer/PTL Surface Morphology Engineering. When anode catalyst loading is significantly reduced, it has been found that the efficiency and durability of the cell often decrease.[145] This may be attributed to the fact that conventional coating methods cannot form an even and continuous layer when the catalyst loading is too low. In such cases, CL contains many isolated catalyst islands, which neither are connected to the bulk CL nor have good electrical contact with PTL, as illustrated in Figure 12a and c.[146,147] In other words, deficient contact at the PTL/CL interface and low in-plane conductivity in CL result in low catalyst utilization during OER.

To address this issue, an efficient approach is to tune the morphology of CL to increase the electrical contact between PTL and CL and to enhance the in-plane charge transfer. Hegge et al. coated a PEM with a layer of IrO_2 nanoparticles (0.1 mg_{Ir} cm^{-2}) and then deposited IrO_2 nanofibers (0.1 mg_{Ir} cm^{-2}) on top of it.[147] Compared to CCM of 0.2 mg_{Ir} cm^{-2} IrO_2 nanoparticles, the isolated catalyst islands were connected by the nanofiber layer (Figure 12b, d), which was further confirmed by the increased in-plane CL conductivity. The
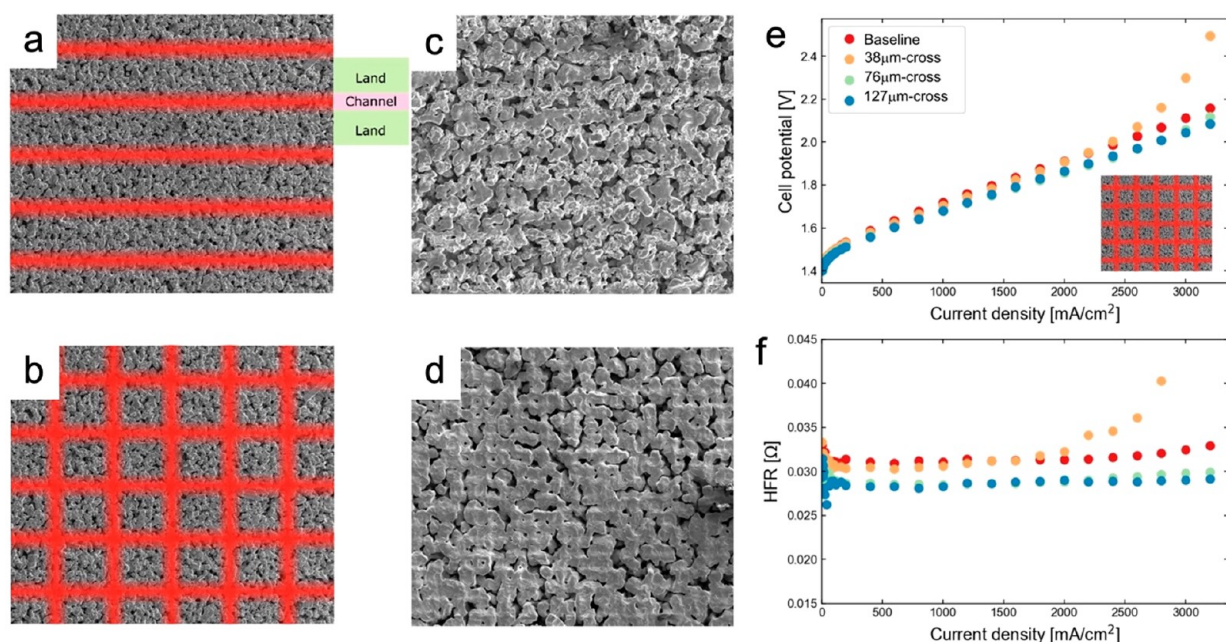
Figure 13. (a, b) Schematic of (a) parallel ablation and (b) cross ablation. (c, d) SEM images of (c) parallel ablation and (d) cross ablation. For both, d_{path} = 127 μm. (e) Polarization curves of cross ablated PTL in comparison with baseline. (f) HFR of cross ablated PTL in comparison with baseline. Reproduced with permission from ref 149. Copyright 2023 Elsevier.

hybrid anode also showed lower HFR, indicating more intimate contact between PTL and CL and accelerated electron transfer at the interface. Regarding durability, PEMWE cell with the hybrid anode showed only 29 mV of voltage increase after operating at 2 A cm^{-2} for 150 h, while the cell with only IrO$_2$ nanoparticle anode had a voltage increase of 104 mV.

Similarly, Chatterjee et al. synthesized a nanoporous Ir nanosheet (npIr-NS) catalyst by dealloying Ni−Ir precursor alloy.[148] As shown in Figure 12e, the nanosheets which are about 1 μm in lateral length and 100 nm in thickness are expected to build up a catalyst layer with low in-plane resistance, due to its lateral and overlaid structure. The ohmic overpotential of MEA with npIr-NS was obviously reduced at an ultralow Ir loading of 0.06 mg$_{Ir}$ cm^{-2} (Figure 12f), benefiting from the improved contact as well as charge transfer at the PTL/CL interface.

Another approach to improve interfacial contact is to apply modification on PTL surface, such as laser ablation. Generally, laser ablation can melt the surface Ti, fill in small pores, and reduce roughness at laser paths. Similar to the function of MPL, the smoothed surface can provide better contact between PTL and CL. A comprehensive study of PTL surface ablation was conducted, focusing on two types of laser ablation paths: parallel (land-channel) and cross (checker-like) patterns (Figure 13a, b).[149] Figure 13c and d show the surface morphology of laser ablated PTL of the same distance between laser paths (d_{path}) for parallel pattern and cross pattern. Assembled with a CCM, for cross patterned ablated PTL, both d_{path} = 76 and 127 μm showed better performance than the baseline, while PTL ablated d_{path} = 38 μm displayed a significant overpotential raise at 2500 mA cm^{-2} (Figure 13e). Both of the PTL with bigger d_{path} exihibited lower HFR than baseline (Figure 13f), due to the enhanced contact between PTL and CL resulted from the smoothened PTL surface. However, the failure of PTL with d_{path} = 38 μm was mainly contributed by a high ohmic resistance at high current density.

One possible reason to this can be that PTL with d_{path} = 38 μm poses a more uneven surface than PTL with a bigger d_{path}, therefore distinct membrane and CL deformation or even PTL intrusion into CL can happen, and this local compression effect may negatively impact the HFR. Additionally, in another study by Lee et al, this laser ablation strategy was also proved effective for GDE anode.[150] To be specific, sintered Ti PTL was first laser ablated and coated with Ir by sputtering deposition. Consequently, lower kinetic overpotential and Tafel slope was achieved using laser ablated PTL.

3.2.3. Supported Catalyst Layer. Another method to efficiently engineer the PTL/CL interface with ultralow Ir loading is combining a support material to CL, forming a thicker layer (Figure 6f). The construction of a supported CL can not only increase catalyst utilization by avoiding gaps in the CL and enhancing Ir dispersion[151] but also favor the contact between the CL and PTL as well.[122] A similar case is that, in PEMFC, Pt nanoparticles are usually well dispersed on carbon black, which has high surface area and high conductivity, and can greatly enhance the contact at PTL/CL interface.[106]

The support material has to meet several requirements to become qualified, such as but not limited to resistance to highly acidic environment, low price, and sufficient conductivity.[152] Among several candidates, titanium oxide has raised attention due to its low price and corrosion resistance at harsh environment. Rozain et al. used sieved commercial TiO$_2$ with particle size ranging from 1 to 40 μm as support material and found the larger TiO$_2$ particles will protrude CL, favoring an enlarged PTL/CL interface.[153] However, the biggest problem with TiO$_2$ support is the low conductivity (2.6 × 10^{-6} S cm^{-1} for TiO$_2$ and 4.9 S cm^{-1} for IrO$_2$), which may be improved in several ways. Some efforts have been made to enhance overall conductivity without modification on TiO$_2$ itself, but creating better coverage of the IrO$_2$ layer.[154−158] Generally, a uniform and complete coverage of IrO$_2$ on top of TiO$_2$ is of vital importance for performance enhancement in
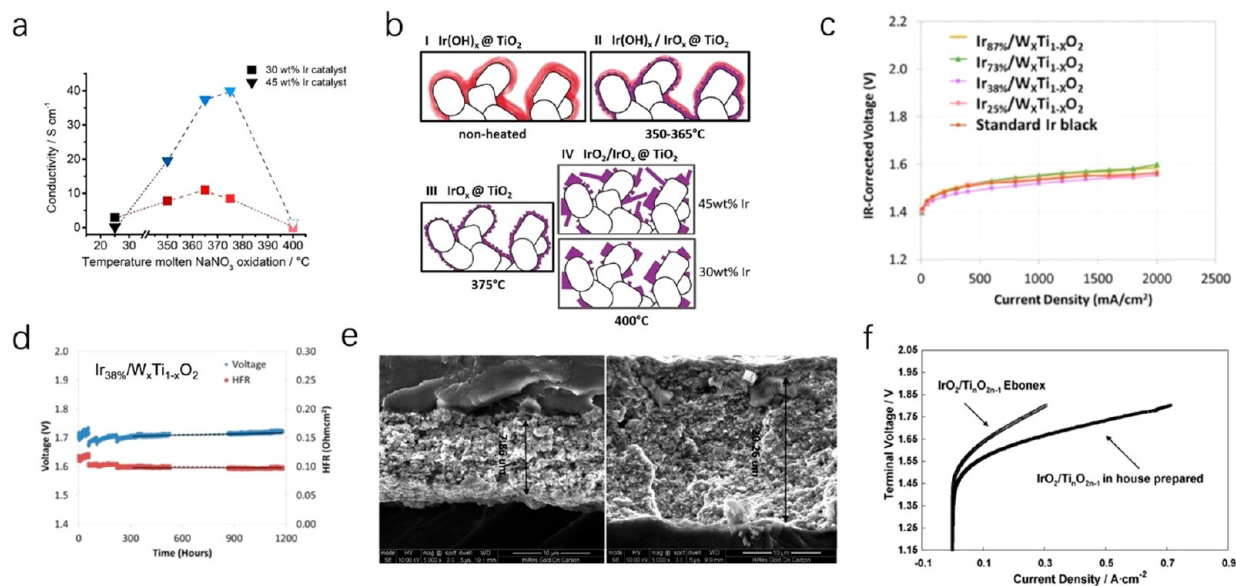
Figure 14. (a) Correlation of conductivity and molten $NaNO_3$ oxidation temperature of 30 (square) and 45 wt % Ir (triangle) coated TiO_2 catalyst. (b) Schematic illustration of catalyst nanostructure formation after oxidation at different temperatures. Reproduced with permission from ref 157. Copyright 2021 Elsevier. (c) IR-corrected polarization curves of $W_xTi_{1-x}O_2$ with various Ir loading, compared with standard Ir black catalyst. (d) Stability test of $Ir_{38\%}/W_xTi_{1-x}O_2$ at 1500 mA cm^{-2}, 80 °C. Reproduced with permission from ref 162. Copyright 2018 IOP Publishing. (e) Cross-sectional SEM image of MEA with pure IrO_2 (left, CL thickness = 7.68 μm) and $IrO_2/Ti_{1-x}Ta_xO_2$ (right, CL thickness = 20.26 μm). Reproduced with permission from ref 159. Copyright 2017 Royal Society of Chemistry. (f) Polarization curves of IrO_2/Ti_nO_{2n-1} prepared in house and from Ebonex at 1 bar abs and 80 °C. Reproduced with permission from ref 165. Copyright 2009 Elsevier.

this type of catalysts.[158] Mazúr et al. found that using low surface area TiO_2 support can improve the IrO_2-TiO_2 catalyst activity when IrO_2 mass percentage was kept at 60%, due to a more homogeneous and continuous coverage of IrO_2 on top of TiO_2 formed for low-surface-area TiO_2 support.[156] Böhm et al. fabricated a highly conductive $IrO_x@TiO_2$ of more than 40 S cm^{-1} (45 wt % IrO_2) by precisely controlling the temperature of molten $NaNO_3$ oxidation.[157] At an optimum oxidation temperature of 375 °C, a homogeneous layer of IrO_x nanoparticles can fully cover the TiO_2 surface (Figure 14a,b), while further increasing the oxidation temperature will cause agglomeration of IrO_2, therefore severely affecting the conductivity.

To enhance the conductivity of TiO_2, it is a common approach to dope a foreign metal, such as tantalum (Ta),[159] Nb,[160,161] tungsten (W),[162,163] and vanadium(V).[164] Zhao et al. developed a template-free and surfactant-free method to disperse Ir nanoparticles on W doped TiO_2 ($W_xTi_{1-x}O_2$).[162] It was found that all samples showed similar IR-corrected voltage in PEMWE as the standard Ir black reference (Figure 14c), while the raw cell potentials of anode catalysts of higher Ir loading ($Ir_{87\%}/W_xTi_{1-x}O_2$ and $Ir_{73\%}/W_xTi_{1-x}O_2$) were obviously higher than the standard, possibly due to Ir aggregation in those samples. The optimized sample, $Ir_{38\%}/W_xTi_{1-x}O_2$ showed very promising durability at a current density of 1500 mA cm^{-2} for 1200 h (Figure 14d). It was pointed out by Lv et al. that controlling the anode CL thickness in a reasonable range can be crucial for lowering overpotential in PEM water electrolysis.[159] They found that the $IrO_2/Ti_{1-x}Ta_xO_2$ catalysts had a higher overpotential compared with IrO_2, especially at high current densities, partly due to the higher cell HFR that arised from lower conductivity. Furthermore, the anode CL of 20.26 μm was regarded as being too thick, and that may contribute to the increase in transport resistance (Figure 14e).

Apart from doping another element, fabricating suboxides is also a viable way to enhance conductivity of TiO_2.[165−167] Siracusano et al. studied both the commercial titanium suboxide (Ebonex) and in-house prepared one, and found the in-house prepared Ti_nO_{2n-1} exhibited better performance in both activity and stability (Figure 14f).[165] Additionally, SnO_2-based materials are also excellent candidates as support for IrO_2 in PEMWE anode, especially those with foreign metal dopants.[168−171]

One limitation of constructing metal oxide supported CL for PEMWE anode is that usually IrO_2 must not be lower than 30 wt % in order to maintain reasonable catalyst conductivity, due to the low conductivity of support material. This issue can potentially be resolved if proper doping can significantly increase its conductivity without adding much cost. Additionally, if metal oxides of higher surface area and mesoporous structure can be developed, the performance can be further improved.[172]

4. CATALYST COATING TECHNIQUES

4.1. Coating CL on Membrane. *4.1.1. Direct Spray.* Direct spray is one of the most widely used methods to fabricate CCM in PEMWE[173] and PEMFC.[34] Direct spray procedure includes two steps, which are ink preparation and spraying. "Ink" refers to a mixture of catalyst, ionomer, and appropriate solvent, which can be isopropyl alcohol (IPA), ethanol, water, or more commonly a mixture of them. After being well dispersed via sonication, the ink is sprayed onto a fixed PEM using an air spray gun or ultrasonic spray equipment. Sometimes the PEM is fixed on a heating plate to accelerate solvent evaporation. Ideally, the CL fabricated in this way is a homogeneous layer of several microns and has a porous structure. The direct spray method may seem to be quite simple, while in fact there are many parameters to be optimized in the procedure, and improper parameters can even
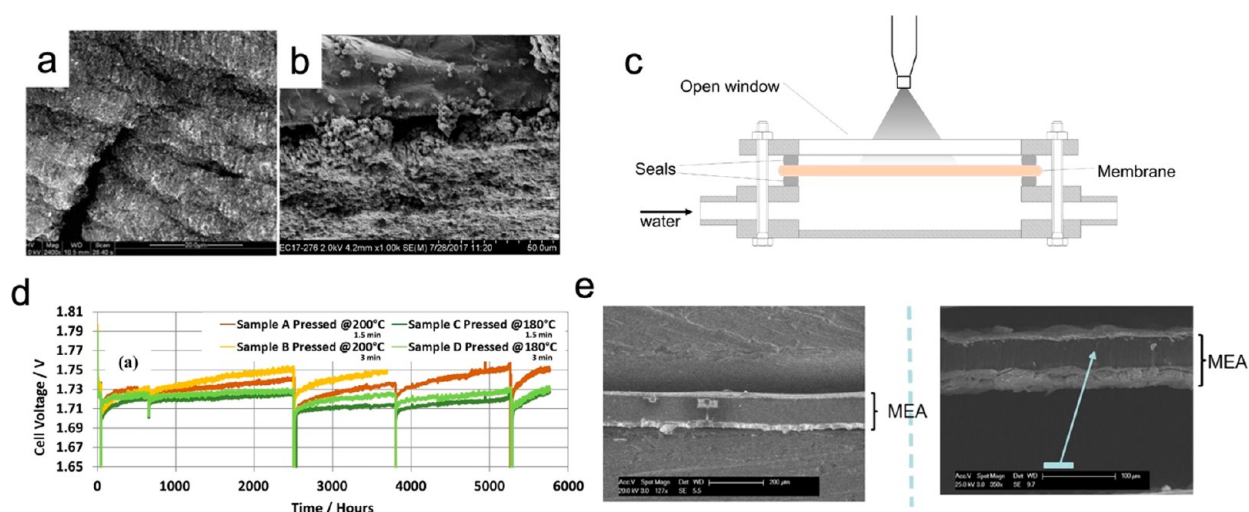
Figure 15. (a) SEM image of a CCM fabricated by spraying coating method with severe membrane swelling and wrinkle. Reproduced with permission from ref 175. Copyright 2009 Elsevier. (b) Cross-sectional SEM of a CCM fabricated by spraying coating method with obvious crack at PEM/CL interface. (c) Schematic illustration of the setup of swelling-spray method. Reproduced with permission from ref 178. Copyright 2017 Elsevier. (d) Durability test at 1 A cm^{-2} of CCM hot-pressed at different temperatures and durations. (e) Cross-sectional SEM images of freshly made CCM (left) and used CCM (right). Reproduced with permission from ref 186. Copyright 2018 Elsevier.
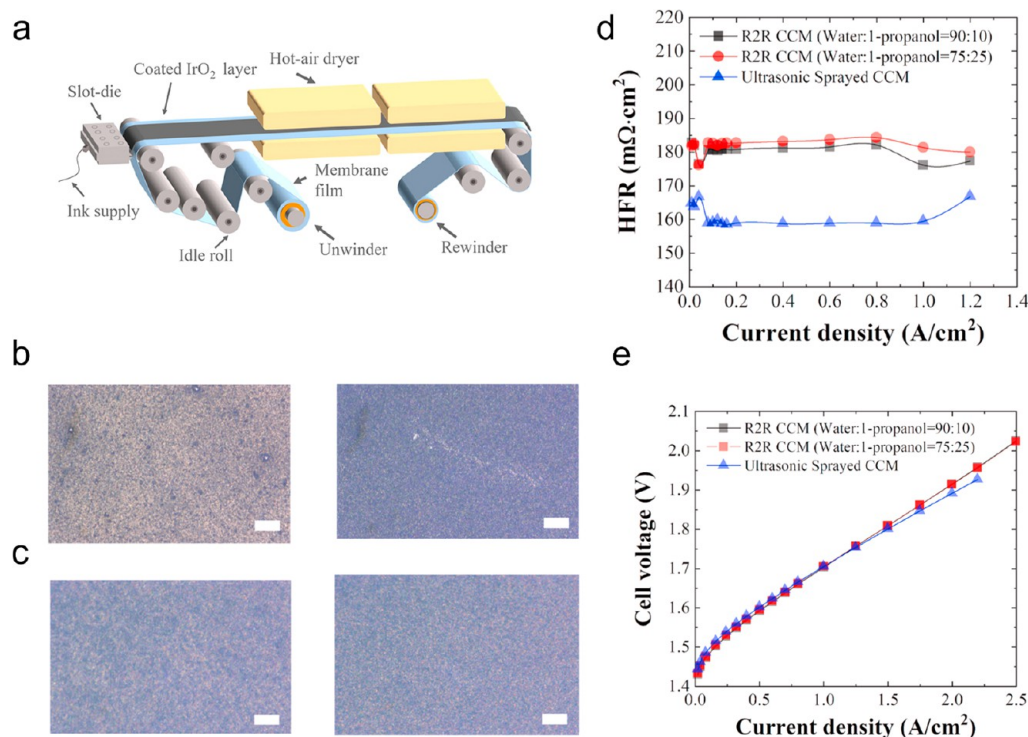

Figure 16. (a) Schematic illustration of slot die coating process. (b) Top-view microscopic images of CL coated by R2R coating with ink containing ethanol. Left: 10 wt % IrO$_2$ in ink, water:ethanol = 75:25. Right: 20 wt % IrO$_2$ in ink, water:ethanol = 75:25. (c) Top-view microscopic images of CL coated by R2R coating with ink containing 1-propanol. Left: 10 wt % IrO$_2$ in ink, water:1-propanol = 75:25. Right: 20 wt % IrO$_2$ in ink, water:1-propanol = 75:25. (d) HFR curves of MEA with R2R CCM and ultrasonic sprayed CCM. (e) Polarization curves of MEA with R2R CCM and ultrasonic sprayed CCM at 80 °C. Reproduced with permission from ref 193. Copyright 2020 Elsevier.

lead to cell failure or membrane damage, which will be further discussed in the following paragraphs.

In direct spray method, the 2D PEM/CL interface is established during spray, therefore the condition of membrane and the parameter control during spray can be crucial to PEM/CL interface formation and can have great influence on the overall performance of electrolyzer. One problem for this method arises from the tendency of PEM to seriously swell and wrinkle when contacting organic liquids such as IPA and ethanol (Figure 15a),[174,175] possibly due to the unbalanced van der Waals force inside membrane caused by the inhomogeneous distribution of organic liquids.[176] The distortion of PEM can result in an uneven distribution of catalyst and cracks at the PEM/CL interface (Figure 15b), which will lead to higher ohmic resistance, lower catalyst utilization, and aggravate gradual catalyst loss during the OER operation.[177,178] Sun et al.
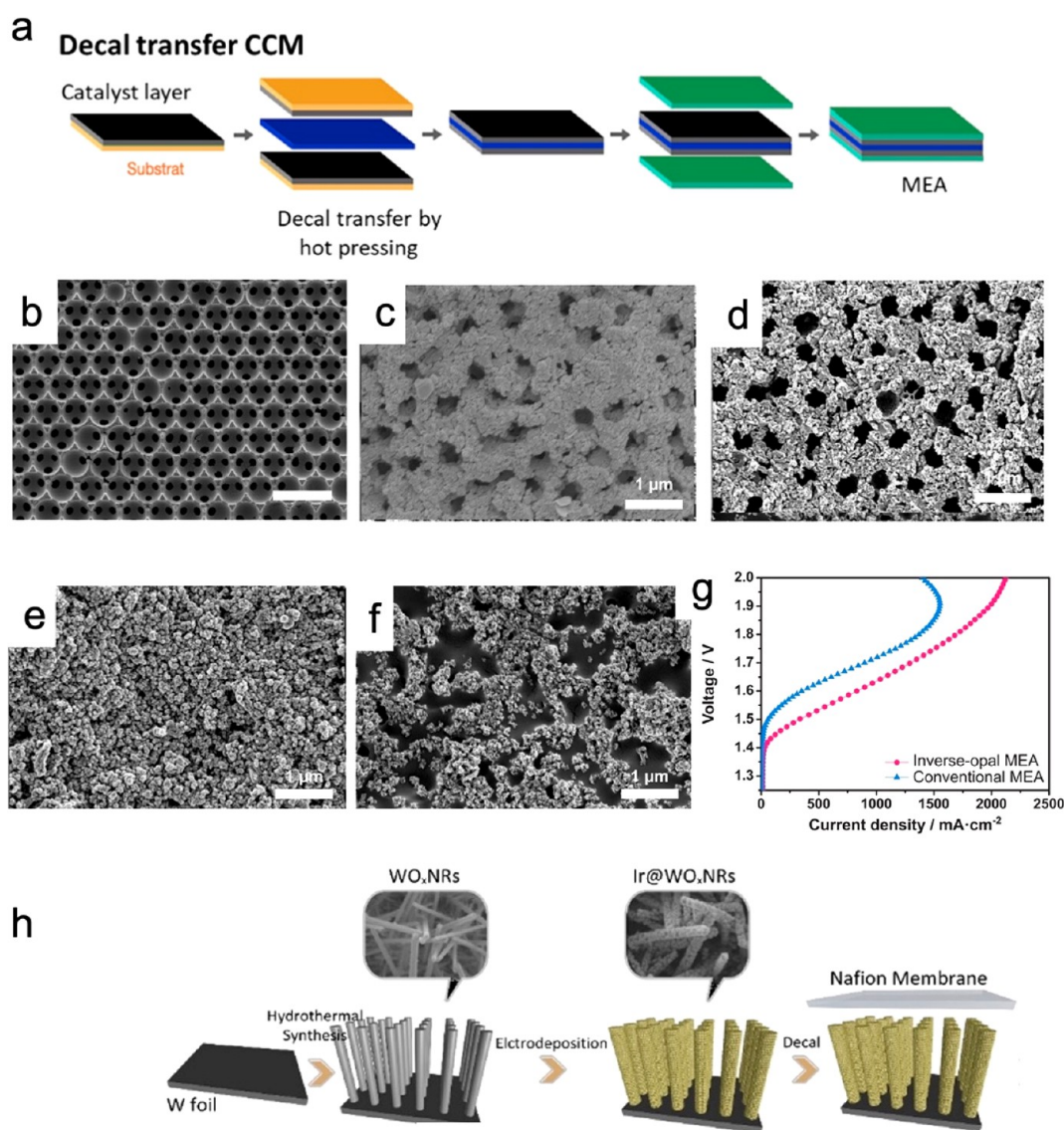
Figure 17. (a) Schematic illustration of the decal transfer process. Reproduced with permission from ref 196. Copyright 2021 MDPI. (b) SEM image of the inverse opal IrO_2 electrode. The scale bar is 1 μm. (c−f) Top-view SEM images of CL in MEA made by decal transfer method: (c, d) inverse opal IrO_2 electrode, loading = 0.02 mg cm^{-2}. e, f) conventional IrO_2 electrode, loading = 0.02 mg cm^{-2}. (c, e) pristine CL, (d, f) post catalysis CL. (g) Polarization curves of inverse-opal MEA and conventional MEA. Reproduced with permission from ref 199. Copyright 2019 Elsevier. (h) Schematic illustration of the fabrication process of Ir@WO$_x$ array electrode. Reproduced with permission from ref 200. Copyright 2021 American Chemical Society.

addressed this problem at lab-scale and in a cost-effective way by taking advantage of the van der Waals force between PEM and Pyrex glass.[175] The wet PEM was first attached to a Pyrex glass with liquid ethanol as an adhesive. After slow heating to evaporate the ethanol, PEM would be firmly attached to the glass surface due to the van der Waals force. By heating at an appropriate temperature during spray, the ethanol solvent in ink could be quickly evaporated before reaching the PEM/glass interface, effectively suppressing local dimensional change. Positioning PEM on top of a vacuum bed is another effective solution to avoiding membrane distortion when contacting organic solvents.[82,179] Apart from the above-mentioned methods, preswelling the membrane by applying specific solvents were also investigated in some works and proved to effectively alleviate membrane deformation during spray and enlarge the interface area at the same time.[177,180] However, usually ethylene glycol or glycerol is required as part of the

expansion agent and it can be difficult to fully evaporate these high-boiling-point solvents during spray, potentially leading to residues inside PEM and further inducing performance loss. Shi et al. developed a novel spray coating method which only require hot water as the expansion agent and heat source for evaporating solvent in ink.[178] In their spray setup, PEM is positioned on top of a chamber where hot water at 90 °C can continuously circulate, keeping PEM swelling up during spray (Figure 15c). Unlike other common spray coating setups where drying requires heat source such as a heating plate or an infrared heating lamp to evaporate water and alcohol solvents inside membrane at the same time,[181,182] in this novel setup shrinkage during evaporation is greatly suppressed since the membrane is kept wet and swollen throughout the process.

In PEMFC, it is a common MEA fabrication method to spray catalyst onto PEM first, and hot-press it at around or above the glass transition temperature of the PEM afterward to

form an improved bonding at the PEM/CL interface.[183−185] Siracusano et al. applied hot pressing as a post treatment for spray coated CCM and further investigated the influence of hot pressing temperature and time on the cell performance (Figure 15d).[186] They found hot pressing at 180 °C for 1.5 min is an optimized parameter for the used Aquivion membrane. As shown in Figure 15e, the hot pressed MEA exhibited excellent PEM/CL interface durability of no obvious delamination and no increment of ohmic resistance after over 5000 h operation at 1 A cm^{-2}. However, raising the temperature to 200 °C or increasing the pressing time will worsen the cell stability, possibly due to the catalyst degradation or loss of ionomer in CL induced by the higher temperature and prolonged pressing time.

4.1.2. Roll to Roll Fabrication. Roll to roll (R2R) is the most promising fabrication approach that can meet the cost and volume target set by the growing demand for PEMWE in the near future. R2R has been proven viable in other energy devices, such as organic photovoltaics,[187,188] perovskite solar cells,[189] and fuel cells.[190,191] Among the several types of R2R coating, slot die coating (SDC) is a preferable choice for CCM manufacture as it is compatible with ink slurry of various rheology and the CL thickness can be precisely controlled.[192] In SDC, the substrate is continuously moving while ink slurry is extruded from the slot die and fills the gap between the substrate and die head (Figure 16a).[193] Followed by the coating process, the wet coated substrate is dried and finally collected as a roll in a rewinder.

Similar to the spray coating method, in SDC the alcohol in ink is in direct contact with membrane while with even prolonged interaction time, therefore swelling should be carefully controlled. It was found that the composition of ink can have great impact on the coating quality. Park et al. investigated the coatability of pure water, water/1-propanol and water/ethanol as the dispersion media in ink slurries.[193] Slurry containing only water showed obvious uneven CL morphology, which was originated from the poor wetting of water on the Nafion membrane surface. Slurry containing water/ethanol formed a continuous CL on PEM, while at microscopic level there was obvious catalyst agglomeration and cracks in CL (Figure 16b). In comparison, slurry containing water/1-propanol resulted in an even and smooth CL morphology (Figure 16c), potentially owing to the better dispersion of catalyst in water/1-propanol and lower surface tension which led to the better wetting at the slurry/PEM interface. The CCM fabricated with ink containing dispersion media of water and 1-propanol had similar HFR (Figure 16d) and I−V curve (Figure 16e) to that fabricated by ultrasonic spray coating, indicating a well-established PEM/CL interface in the anode electrode. Considering it takes 90 min to coat 100 cm^{-2} of membrane using lab-scale ultrasonic spray equipment, while only 7.5 s is needed to coat the same area with SDC, SDC is more promising in terms of large-scale production of CCM with enhanced coating width and coating speed.

4.1.3. Decal Method. Decal method has been one of the most common methods for the fabrication of CCM in PEMWE and PEMFC both at lab-scale and at large-scale since it was first reported by Wilson and Gottesfeld in 1992.[194,195] A schematic illustration of this method is shown in Figure 17a.[196] In this method, ink containing ionomer, catalyst, and solvent is coated onto a substrate, which is usually a PTFE or Kapton thin film. A PEM is sandwiched between the two coated substrates with CL facing each other and hot-pressed at

optimized pressure and temperature for a certain duration. Then the two substrates are peeled off after hot pressing, leaving two thin layers of catalysts on PEM and forming a CCM. For large-scale fabrication, instead of a flat hot-press machine, a roll-press device can be used for the hot pressing process with a high rolling speed of 50 mm min^{-1}.[197]

Compared with other catalyst coating techniques for PEMWE, decal transfer consists of more consecutive processing steps, each of which contains several parameters, adding to its complexity. Since the PEM/CL interface is constructed during hot pressing, the pressing temperature, pressure, and duration can have major impact on the interface quality and properties. Shahgaldi et al. studied the effects of hot pressing conditions and it was found that prolonged pressing duration and higher compression will lead to thinner CL and reduced pores, which further causes a raise in transport resistance, while insufficient compression may not deliver intimate contact between CL and PEM.[198] The hot pressing temperature should also be carefully determined based on the glass transition temperature of PEM and ionomer. Typically, optimized hot pressing temperature should be around the glass transition temperature, which ensures sufficient mobility of ionomer to closely bind CL with PEM, favoring robust PEM/CL interface without reducing the water uptake and proton conductivity in PEM.[183]

Generally speaking, the CCM fabricated by decal method can possess low ohmic and transport resistance that is comparable with that fabricated by direct spray method.[176] On the other hand, a unique advantage of this method is that it allows for the construction of CL with an ordered structure. For instance, Park et al. proposed fabrication of novel porous inverse-opal structured IrO$_2$ as anode CL in PEMWE by a modified decal method.[199] The inverse-opal structured IrO$_2$ layer was constructed on top of Ni-fluorine-doped tin oxide (FTO) by utilizing self-assembled polystyrene beads as sacrificing template, as shown in Figure 17b. The IrO$_2$ CL was transferred to PEM by hot-pressing the prepared electrode together with PEM, followed by HNO$_3$ etching of Ni-FTO, leaving a well-structured CL attached on PEM. When the loading was 0.02 mg cm^{-2}, the CCM with conventional IrO$_2$ CL revealed obvious catalyst loss and morphology change (Figure 17e,f), while the inverse-opal electrode mainly maintained its morphology with big pores (Figure 17c,d), which can assist bubble removal during reaction. As indicated by the polarization curves in Figure 17g, the inverse-opal MEA apparently has superior performance over conventional MEA in high voltage region, which can be attributed to the facile gas removal and more exposed active sites brought by the hollow structure in inverse-opal electrode. Jiang and colleagues also applied decal method to fabricate CL with ordered structure. As shown in Figure 17h, ordered arrays of Ir-coated WO$_x$ at anode in PEMWE was constructed by a similar modified decal method. The Ir@WO$_x$ arrays were first grown on W foil by a hydrothermal method, followed by hot-pressing at 2 MPa, 140 °C for 3 min with a Nafion 115 membrane to combine CL with PEM surface.[200]

4.1.4. Reactive Spray Deposition Technology. As an advanced type of vapor phase deposition method, reactive spray deposition technology (RSDT) is a new technology that was first reported in 2009 for the deposition of electrolyte and cathode materials in solid oxide fuel cells.[201] In recent years, researchers expanded its application to nanocatalyst deposition for PEMFC and PEMWE.[202] RSDT is a flame-based
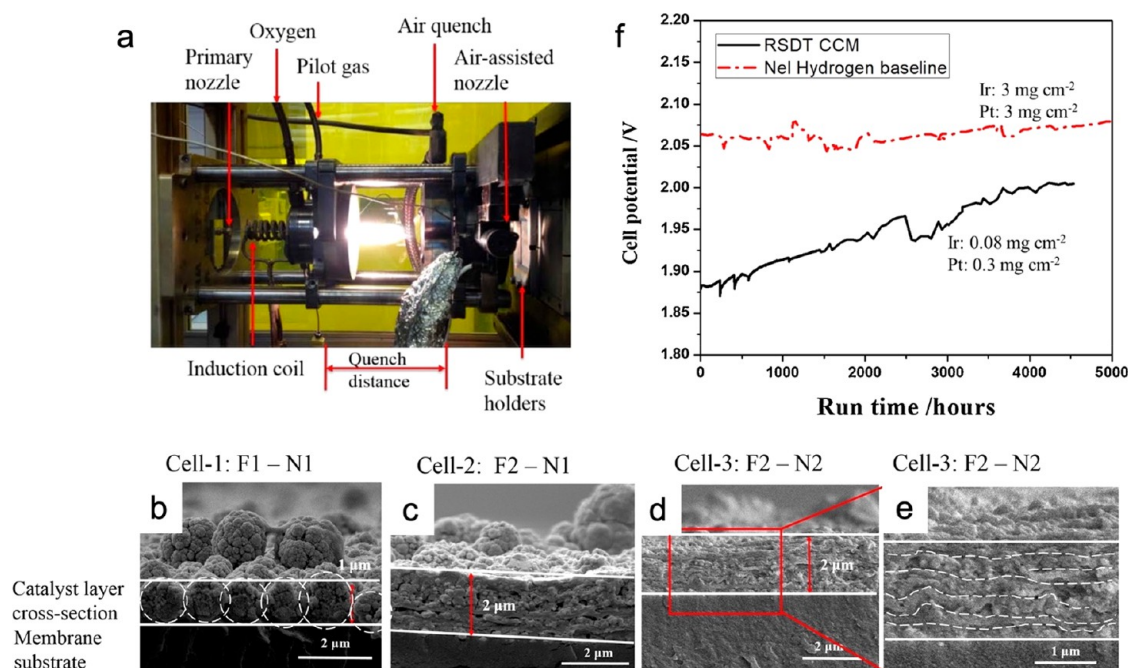
Figure 18. (a) Photo of an RSDT equipment. Reproduced with permission from ref 203. Copyright 2016. Elsevier. (b–e) Cross-sectional SEM images of CL fabricated with different flame conditions (F1 and F2) and Nafion spray conditions (N1 and N2). F1: lower in Ir precursor flow rate, Ir concentration, oxygen flow rate, air quench distance, and air quench flow rate. N1: higher in Nafion spray flow rate and Nafion concentration. (e) Magnified region of part d. Reproduced with permission from ref 204. Copyright 2018 Elsevier. (f) Stability test of MEA fully fabricated by RSDT in comparison with Nel hydrogen baseline. Reproduced with permission from ref 206. Copyright 2020 Elsevier.

technology that combines catalyst fabrication and CL deposition in one step (Figure 18a).[203] In detail, metal precursors are first dissolved in combustion solvents such as ethanol, and the formed solution will be pumped into combustion zone through a customized needle and be atomized into fine spray. In combustion zone, the droplets are ignited and solvents combustion can provide heat for the decomposition of precursors and formation of desired nanoparticles. The particles are then quickly air quenched at well-controlled air flow rate and distance to confine the particle growth, as well as to avoid damage to the deposited substrates, which is especially vital for temperature sensitive substrates such as PEM. Lastly, before the particles finally being deposited, they are mixed with support or ionomer sprayed by an air-assisted nozzle positioned just before the substrate.

Yu et al. reported that by utilizing RSDT, the catalyst particle size, CL morphology and catalyst loading at anode in PEMWE can be well controlled.[204] To be specific, they found that the IrO_x catalyst size was affected mainly by nozzle temperature and precursor solution properties, instead of Ir concentration. Alternatively, by tuning the Ir precursor flow rate/concentration and ionomer flow rate/concentration, the CL morphology exhibited a major difference (Figure 18b–e). To investigate the effect of these parameters, three combinations (F1–N1, F2–N1, and F2–N2) were carried out to compare the consequent CL morphology. When the ionomer flow rate/concentration were high (N1), significant agglomeration was observed within CL with low Ir precursor flow rate/concentration (F1) (Figure 18b). Regarding the CL surface morphology, if ionomer flow rate/concentration were kept at high value (N1), obvious agglomeration would appear at CL surface no matter what Ir precursor flow rate/concentration were chosen (Figure 18b,c), which strongly suggested that lower ionomer flow rate/concentration (N2)

should be applied to avoid agglomeration. With increased Ir precursor flow rate/concentration (F2) and lower ionomer flow rate/concentration (N2) (Figure 18d,e), agglomerates were significantly reduced, while laminated structure appeared in anode CL. By choosing the right parameters, a CL of nanosized IrO_x particles (~2 nm in diameter), ultralow catalyst loading (~0.04 mg cm^{-2}) and uniform distribution of catalyst in ionomer was successfully fabricated on PEM. In terms of the cell performance, as shown in Figure 18f, the electrolyzer had a small degradation rate of ~27 μV h^{-1} in the 4500 h test, which was comparable to that of Nel hydrogen baseline tested with much higher Ir loading in the anode coated by other methods.[205,206]

4.2. Coating CL on Anode PTL. Even though CCM configuration is no doubt dominant in today's PEMWE anode, catalyst coated PTL, also known as GDE or porous transport electrode (PTE) is another promising alternative. Several GDE coating techniques have been reported for PEMWE anode, such as direct spray,[207] electrodeposition,[208–211] dropcasting,[15] atomic layer deposition,[212] and sputtering.[213,214] Among these, direct spray, electrodeposition, and sputtering are three techniques that are more extensively studied and will be further discussed in the following sections.

4.2.1. Direct Spray. Very similar to the direct spray method for CCM manufacturing, direct spray of catalyst onto PTL also incorporates spraying an ink that contains solvent, catalyst powder, and ionomer by using a coating machine.[215] But unlike in CCM manufacturing that airbrush coating is a common low-cost practice, airbrush coating was only reported to coat catalyst on Ti PTL with a microporous layer,[166] and there has barely been any successful demonstration of airbrush-coated CL on common Ti fiber or sintered powder. Instead, ultrasonic spray coater is often utilized for different types of
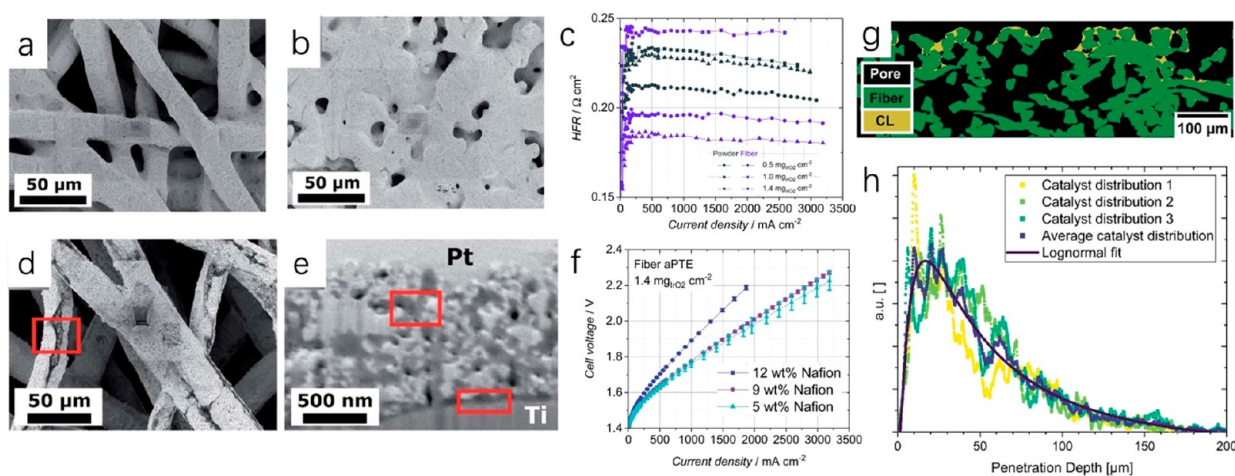
Figure 19. (a, b) Surface morphology of Ti GDE spray coated with 1.0 mg cm$_{-2}$ IrO$_2$ and 5 wt % Nafion. A: Ti fiber GDE. B: sintered Ti GDE. (c) HFR of MEA consisting sprayed GDE, with different IrO$_2$ loadings and GDE types. (d, e) Morphology of spray coated Ti felt GDE with 21% Nafion in catalyst layer. (f) Polarization curves of spray coated GDEs with different Nafion content. Reproduced with permission from ref 215. Copyright 2019 Royal Society of Chemistry. (g) Cross-sectional backscattered electron image of a spray-coated Ti felt. (h) Normalized catalyst distribution of three cross sections, together with their weighted average and its log-normal fitted curve. Reproduced with permission from ref 105. Copyright 2022 Wiley−VCH.
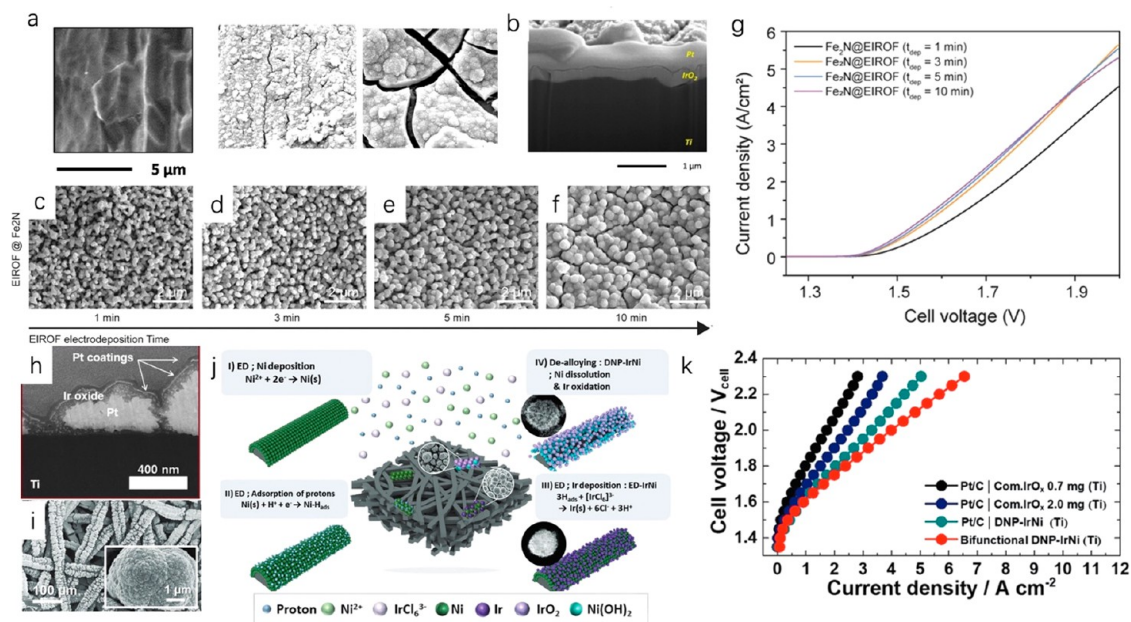

Figure 20. (a) Morphology of electrodeposited IrO$_2$ layer on Ti mesh (E_{dep} = 0.7 V vs SCE). Left: t_{dep} = 1 min. Middle: t_{dep} = 5 min. Right: t_{dep} = 20 min. (b) Cross-sectional image of IrO$_2$ electrodeposited Ti mesh (E_{dep} = 0.7 V vs SCE, t_{dep} = 5 min). Reproduced with permission from ref 208. Copyright 2018 Elsevier. (c−f) Morphology of EIROF of different t_{dep} on Ti PTL coated with Fe$_2$N. (g) Polarization curves of MEA consisting of Fe$_2$N-coated Ti PTL with EIROF of different t_{dep}. Reproduced with permission from ref 209. Copyright 2023 Elsevier. (h) Cross-sectional FIB-SEM image of Pt@IrO$_2$. Surface Pt was coated for surface protection. Reproduced with permission from ref 210. Copyright 2020 Elsevier. (i) SEM image of DNP-IrNi. Inset: SEM image of higher magnification. (j) Schematic illustration of the electrodeposition process of spore-structure IrNi on Ti PTL. (k) Polarization curves of MEA with different anode electrode. Reproduced with permission from ref 211. Copyright 2022 Royal Society of Chemistry.

PTL,[216] possibly due to the incompatibility between air brush coating and the large pore structure of Ti PTL.

Bühler et al. investigated optimization of ultrasonic coated GDE, regarding the impact of PTL type, Nafion content, and catalyst loading on PEMWE performance.[215] As shown in Figure 19a and b, the coated CL surface on fiber Ti PTL and powder-sintered Ti PTL appeared to be completely different in morphology. The GDE with fiber Ti PTL showed no pore filled by catalyst, while that with powder-sintered Ti PTL had a

much more homogeneous and continuous CL due to its denser structure and smaller pore size. However, it was found that the GDE with powder-sintered Ti PTL and a moderate catalyst loading of 1.0 or 1.4 mg$_{IrO2}$ cm^{-2} had a higher HFR when applied in PEMWE anode (Figure 19c), possibly due to the partly filled pores and thicker coating CL both leading to longer electron migration pathways. It was also found that a low Nafion content of 5 wt % in CL resulted in lowest cell voltage among MEA with CL containing various Nafion level,
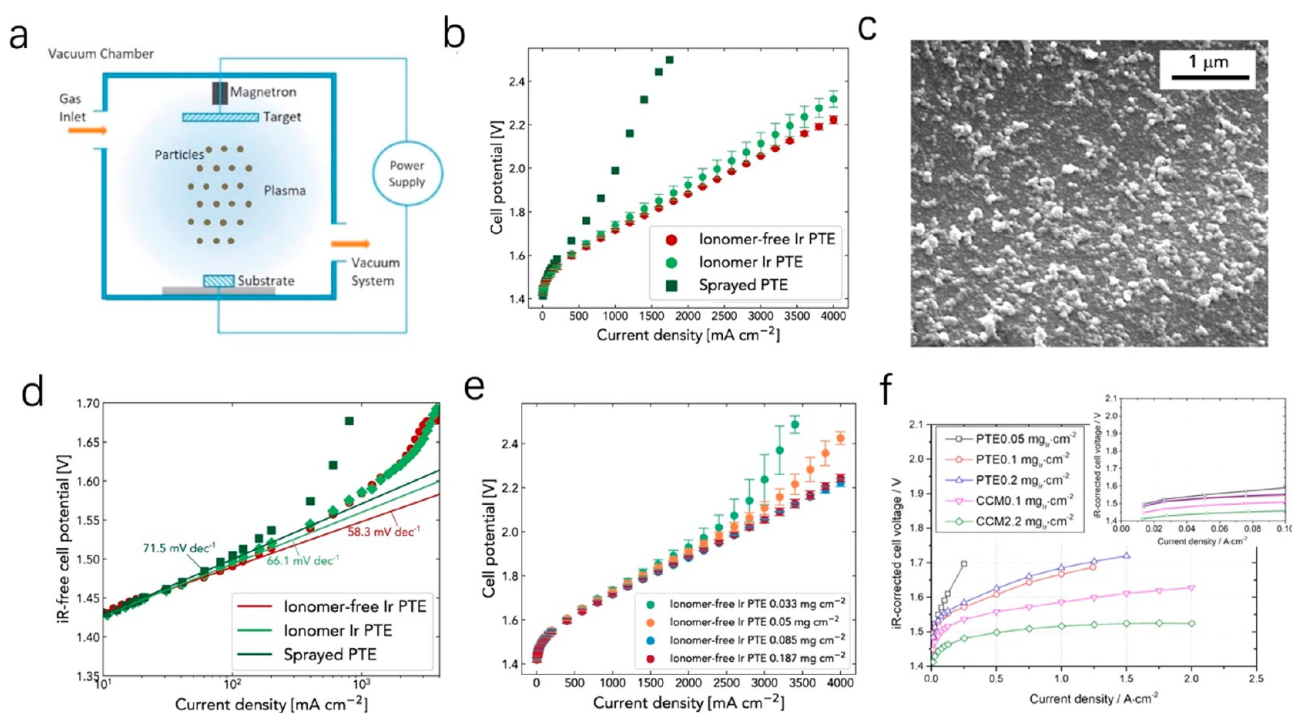
Figure 21. (a) Schematic illustration of sputtering deposition process. Reproduced with permission from ref 223. Copyright 2018 Elsevier. (b) Polarization curves of sprayed GDE and sputtering coated GDE. (c) SEM image of surface of Ir sputtering coated GDE. (d) Tafel slopes of sprayed GDE and sputtering coated GDE. (e) Polarization curves of MEA assembled with sputtering-coated Ir GDE with various Ir loading. Reproduced with permission from ref 150. Copyright 2023 Springer Nature. (f) HFR-free cell voltages of MEA assembled with GDE and CCM of various Ir loadings. Reproduced with permission from ref 226. Copyright 2021 American Chemical Society.

while a higher Nafion content of 21% caused severe CL peeling off and an electrically insulated layer of Nafion at PTL/CL interface (Figure 19d,e). However, low Nafion content of 5% or lower may also cause inhomogeneity in spray pattern. Thus, according to the polarization curve in Figure 19f, compromising between spraying reproducibility and overpotential, 9 wt % of Nafion was considered to be optimized. It is worth mentioning that ultrasonic spray is not only capable of coating regular catalyst loading of several mg_{Ir} per cm^2, it is also capable of constructing ultralow loading down to several μg_{Ir} per cm^2 as reported by Taie et al.[217] In this work, ultralow loading of 3.5 μg_{Ir} cm^{-2} was successfully fabricated by ultrasonic spray coating with well optimized ink composition and preparation procedure.

The through-plane catalyst distribution in a GDE with fiber Ti PTL coated by an ultrasonic spray coater was investigated by Bierling et al.[105] The IrO$_2$ catalyst loading was 1.5 mg cm^{-2} and binder content was of ~10 wt %. The cross-sectional backscattered electron imaging was obtained to have a profound and intuitive demonstration of catalyst distribution, as shown in Figure 19g and h. The result clearly reveals that catalyst follows a log-normal distribution, and 90% of catalyst is within the top 100 μm cross sectional region of fiber Ti PTL.

4.2.2. Electrodeposition. Electrodeposition is a common one-step method for catalyst synthesis and coating. In a typical electrodeposition process, the PTL to be deposited on is connected as the working electrode in the three-electrode system and immersed in electrolyte that contains metal precursors. By applying potential between working electrode and counter electrode, the metal ions in solution are reduced to solid metal states (cathodic electrodeposition) or oxidized (anodic electrodeposition) and deposited on the surface of

PTL. During the process, several parameters can be precisely tuned to control the morphology and loading of deposited catalyst, such as electrolyte pH, precursor concentrations, deposition current density, and deposition time.

For anode GDE in PEMWE, electrodeposition is often utilized to coat Ir or iridium oxide, either directly to coat on Ti PTL or on other deposited material. Choe et al. explored anodic electrodeposition of IrO$_2$ onto Ti mesh PTL and found the deposited CL formed a dense and uniform protective layer at a low loading of 0.4 mg cm^{-2}.[208] By prolongating the deposition time at a fixed applied potential, the IrO$_2$ loading gradually increased and a corresponding better catalyst coverage on Ti mesh was achieved (Figure 20a). However, cracks and agglomerates began to form when further increasing deposition time (t_{dep}) to 20 min, which would result in a much thicker IrO$_2$ layer of 2.69 mg cm^{-2}. Specifically, Figure 20b shows the cross-sectional image of the GDE with a t_{dep} of 5 min with the corresponding IrO$_2$ loading of 0.4 mg cm^{-2}. The IrO$_2$ layer exhibited a complete and homogeneous coverage on the Ti PTL surface, which led to its strong protection against the corrosion of Ti under the harsh anode environment in PEMWE. Böhm et al. deposited 0.5 mg cm^{-2} of Ir metal onto a Ti mesh PTL with a microporous layer.[166] Differently, here a layer of TiO$_{2-x}$ particles of 1 μm in diameter was first deposited on the PTL by spray coating, forming a conductive support layer with rough surface. Ir metal was then deposited on top of TiO$_{2-x}$ particles by cathodic electrodeposition, forming particles of 50−100 nm in diameter. Jeong et al. investigated the OER performance enhancement induced by electrodeposited IrO$_2$ film (EIROF) on top of Fe$_2$N.[209] When t_{dep} = 1 min, the pore structure in Fe$_2$N was well preserved (Figure 20c). With increase in t_{dep}, the pores between Fe$_2$N
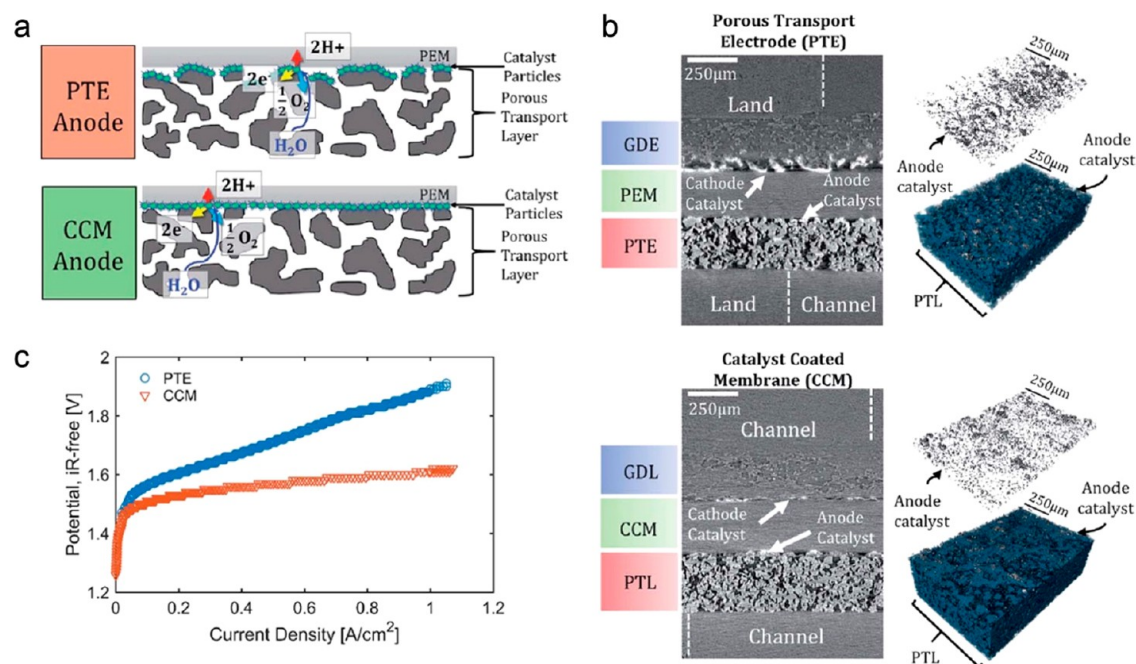
Figure 22. (a) Schematic of the anode side and mass transport process of the PEMWE for the PTE and CCM configurations. (b) Labeled tomographic cross-section of the PTE and CCM MEA sample. The anode catalyst layer (above, silver) was volume rendered separate from, and in combination with, the sintered titanium PTL (below, blue). (c) Polarization curves for the PTE and CCM MEA samples. Reproduced with permission from ref 103. Copyright 2020 Royal Society of Chemistry.

particles were gradually narrowed by EIROF and eventually filled up by EIROF when t_{dep} reached 10 min (Figure 20d−f). The polarization curves of MEA with electrodes of different t_{dep} were in correspondence with the electrode morphology (Figure 20g). The performance was obviously promoted when t_{dep} was increased from 1 to 3 min and reached 4.5 A cm^{-2} at 1.9 V, while further increasing t_{dep} would not introduce any performance enhancement. This can be possibly due to mass transport limitation brought by narrowed or filled pores between Fe$_2$N particles when t_{dep} was prolonged.

Electrodeposition can also be used to synthesize and deposit OER catalysts with sophisticated structures. Lim et al. applied a two-step electrodeposition process to construct a core−shell structure catalyst of hemispherical Pt core and 70 nm of IrO$_2$ shell in unitized regenerative fuel cell (Figure 20h).[210] The precious metal usage of this Pt@IrO$_2$ catalyst is only 0.8 mg$_{Ir+Pt}$ cm^{-2}, which is significantly lower than the usual loading of ~4 mg$_{Ir+Pt}$ cm^{-2} without sacrificing performance. Yeo et al. reported a novel 3D dandelion spore-structured IrNi catalyst fabricated by electrodeposition and a subsequent electrochemical dealloy process.[211] As illustrated in Figure 20j, the Ti fiber GDL was first immersed in the electrolyte comprising NiCl$_2$·6H$_2$O, Na$_3$IrCl$_6$·xH$_2$O, HCl, NH$_4$Cl, and H$_3$BO$_3$ and a constant potential of −2.8 V vs SCE was applied for 15 min. During this process, even though Ni and Ir precursors both existed in the electrolyte, Ni was first deposited onto the Ti fibers, forming a highly porous layer due to H$_2$ bubble generation. Then proton adsorption took place at the Ni layer outer surface, where Ir and Ni would together be catalyzed to deposit on top of the porous Ni layer. After the electrodeposition, the GDE was transferred into 0.5 M H$_2$SO$_4$ solution and kept at 10 mA cm^{-2} for 2 h to leach out the majority of Ni, meanwhile creating nanopores and oxidizing Ir. As shown in Figure 20i, a highly porous structure of IrNi particles with ~15 μm in diameter were attached to Ti fibers

while the fiber contour was still maintained. This GDE demonstrated superior activity in PEMWE with a low Ir loading of 0.67 mg$_{Ir}$ cm^{-2}, delivering a high current density of 3.5 A cm^{-2} at 2 V (Figure 20k), potentially owing to the greatly enlarged active surface area and intimate contact between IrNi CL and Ti fiber PTL.

4.2.3. Sputtering. Sputtering deposition is a mature technique within the realm of physical vapor deposition (PVD), which has been widely used in many industries, such as cutting tool,[218] medical device,[219] textile,[220] and solar−thermal device.[221] PVD comprises of processes that involve the vaporization and subsequently deposition of a coating material onto the surface of the substrate to be coated.[222] In sputtering deposition, a target cathode material is subject to bombardment of positive ions, resulting in ejection of atoms from the target (Figure 21a).[223] The ejected atoms will travel through the chamber and condense on the surface of substrate, forming a thin layer which thickness and composition can be precisely controlled. Compared with other GDE fabrication methods, sputtering is more facile since no ink or deposition solution is required for coating, and is also more practical in scalability. It was reported by Toshiba that they have successfully developed technology to fabricate sputtering deposited Ir GDE at largescale,[224] suggesting the great potential in the industrialization of this fabrication method.

In terms of sputtering coating on PTL for PEMWE anode, the advantages of sputtering deposition were discussed in detail by Lee et al.[150] Overall, the sputtered Ir-coated GDE showed much better performance than spray-coated GDE (Figure 21b). The sputtered nanosized catalyst film (Figure 21c) established very strong adherence to PTL surface without ionomer, which led to lower capital cost and prevention of possible ionomer degradation.[128,225] The intimate contact between PTL/CL interface was further confirmed by the lower Tafel slope (Figure 21d), indicating facile charge transfer in
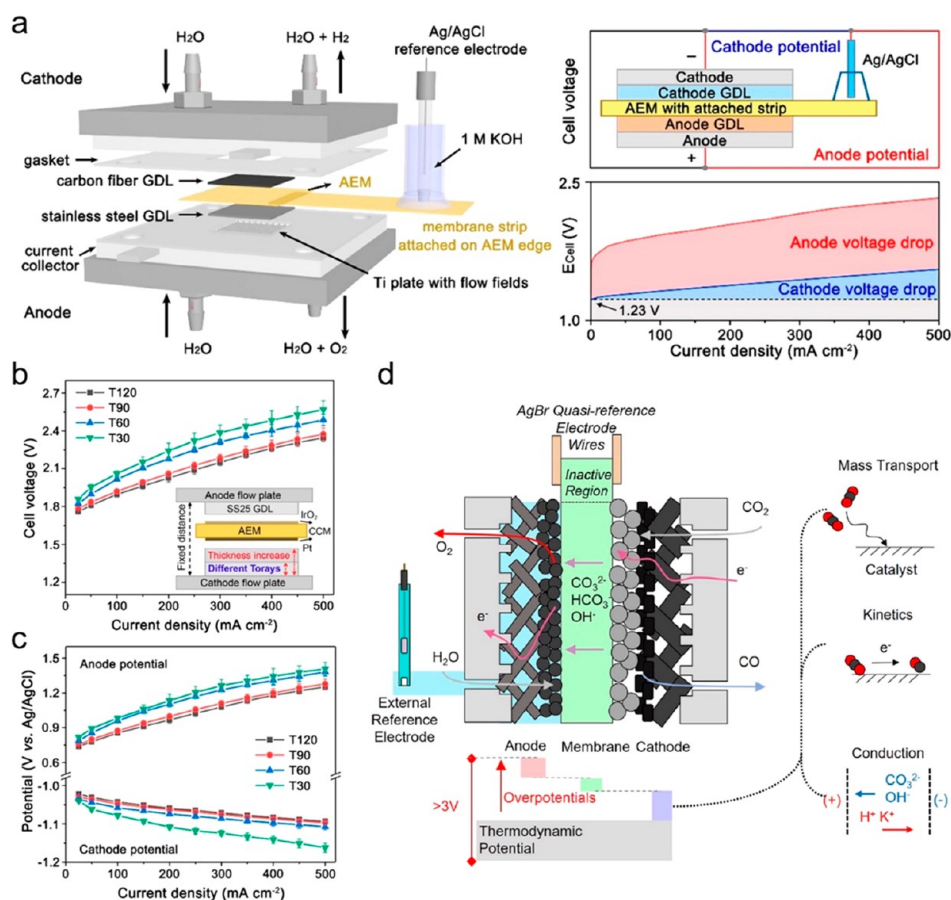
943

Figure 23. (a) Schematic showing the integration of the reference electrode in the AEMWE system, measurement setup and corresponding voltage drops for a typical AEM electrolyzer polarization curve. Polarization curves showing (b) total cell voltage and (c) anode and cathode potential (V vs Ag/AgCl) for the samples with different Toray carbon papers. Reproduced with permission from ref 229. Copyright 2021 American Chemical Society. (d) Schematic of the five-electrode measurement technique in a CO_2 electrolyzer. Reproduced with permission from ref 227. Copyright 2022 American Chemical Society.

sputter-coated GDE. Unlike GDE fabricated by electro-deposition or spray coating that catalyst covers at least partly the bulk PTL, sputtered catalyst is only at the surface of PTL, therefore catalyst utilization is maximized for sputtered GDE. Besides, given the extraordinary homogeneity and controllability of film thickness, sputtering is suitable for fabricating low and ultralow loading of precious metal catalyst. As in Figure 21e, the polarization curves of GDE with various Ir loadings were compared. Negligible performance enhancement was observed from increasing the Ir loading from 0.085 mg cm^{-2} to 0.187 mg cm^{-2}, indicating that a smooth and integrated Ir film was constructed to fully cover PTL surface at 0.085 mg cm^{-2}.

The main drawback of sputter coating for PEMWE anode is the insufficient contact between PEM and CL. The contact area at PEM/CL interface is greatly reduced compared to CCM configuration, especially when the CL surface toward PEM is smooth, as fabricated by sputtering. Liu et al. compared the HFR-free cell voltages of CCM and sputtered GDE and found that at 1 A cm^{-2} and with 0.1 mg_{Ir} cm^{-2}, the cell voltage of MEA with CCM is 100 mV lower than that of MEA with sputtered GDE (Figure 21f).[226] While an intimate contact of large area at PTL/CL interface can be created in sputtered GDE to benefit kinetically, the contact between CL and PEM is very limited compared to CCM, leading to an overall increase in kinetic overpotential especially when applying a thinner Ir coating.

5. DISCUSSION

5.1. CCM vs. GDE, Which Is Better? As discussed above, there are two prevailing electrode configurations, namely CCM and GDE. In a CCM configuration, the CL is deposited on the PEM, while the GDE configuration directly coats the CL on the PTL. Evidently, the CCM configuration ensures intimate contact between CL and PEM and leaves a relatively poor PTL/CL interface (Figure 22a).[103] In comparison, the electron conduction between CL and PTL is favorable in the GDE configuration, while the proton transfer resistance at the PEM/CL interface is high. It remains an open question which configuration is more efficient and stable for PEMWE under practical operation conditions.

Currently, the CCM electrode configuration is more common in the application of PEMWE and PEMFC, due to its sufficient ionic conductivity and technical readiness for large-scale manufacturing. Through X-ray radiography and CT, Leonard et al. observed that the CL in the GDE configuration was more morphologically nonuniform compared to that in CCM and some catalytic sites sunk into the PTL (Figure 22b), thus leading to a higher cell resistance and worse performance (Figure 22c).[103] For CCM, the uniformity of CL can be adjusted through the catalyst ink properties and the ink coating
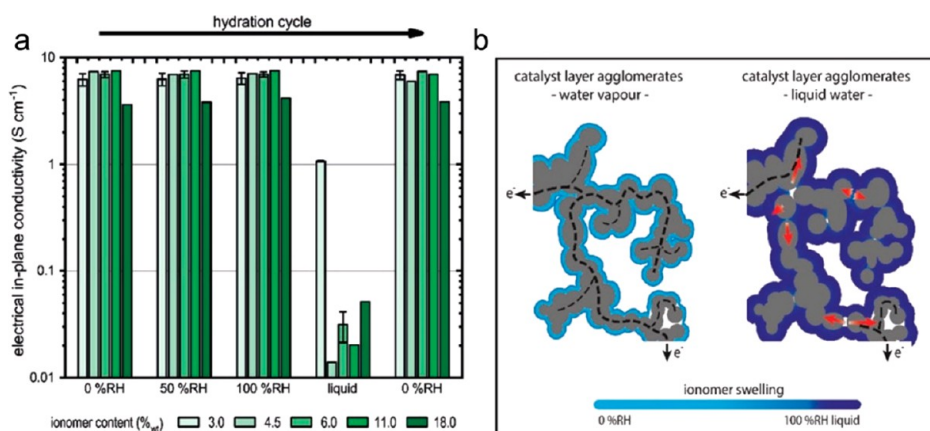
Figure 24. (a) Bar plot of electrical in-plane conductivity for catalyst layers with different ionomer loadings between 3 to 18 wt % at 60 °C in a hydration cycle (dry →100% rh (relative humidity) → liquid water → dry). (b) Schematic of proposed mechanism of ionomer swelling in catalyst layers for equilibration vapor and liquid water; mechanical distortion of electrical percolation network is shown by red arrows. Reproduced with permission from ref 76. Copyright 2019 Wiley-VCH.

process, while the CL morphology largely conforms to the rough surface of PTL in the GDE configuration.[104]

The GDE configuration is also proposed as a promising candidate for PEMWE applications due to some relative strengths over CCM. Despite the poor PEM/CL interface, the decoupling of PEM and CL results in less membrane and CL deformation compared with CCM.[105] Moreover, the choice of membrane is wider for GDE, as it is limited in the process of fabricating CCM (e.g., consideration of the temperature influence during the decal transfer). For some electrode fabrication techniques (e.g., sputtering), the direct coating of CL onto the PTL substrate also simplifies the manufacturing process, lowering the operation cost. In some studies, the PEMWE employing a GDE configuration at anode exhibited comparable or better cell performance than those with CCM.[207,215] For example, Bühler et al. reported that though the GDE configuration has worse kinetics, it showed an enhanced mass transport capability, thus outperforming CCM at high current densites.[207]

Notably, Hansen et al. displayed that the effects of GDE or CCM configuration are also related to the use of different membranes when studying the cathode side in a carbon dioxide (CO_2) electrolyzer.[227] When the Orion AMX 2.8 AEM was used, the CCM largely eliminated the cathode ionic resistance in comparison with GDE. Nevertheless, with FAA-3-50 as the AEM, a high ionic resistance was present in both CCM and GDE configurations. Further voltage loss diagnosis revealed that by substituting CCM for GDE, the ionic resistance shifted from cathode to the anode instead of elimination. Therefore, whether a CCM or GDE configuration is more suitable for PEMWE may depend on specific electrode fabrication methods, catalyst loadings and operation conditions. Efforts to simultaneously engineer both PEM/CL and PTL/CL interfaces are expected to overcome the limitation of the trade-off between a fair proton conduction and electron transfer.

5.2. Separating Anode Overpotential from the Electrolyzer.
For further reduction of the operation cost in PEMWE, optimization of the electrical efficiency (namely cell voltage) is essentially required. The precise analysis of the overpotential sources in the practical electrolysis system is thus of great importance, which enables the location of the component/interface which most needs improvement, as well

as the study of how a single parameter change can influence the different parts in the cell. However, in a typical MEA configuration, only the full cell voltage is commonly measured because the exemption of liquid electrolytes makes it difficult to insert a reference electrode as applied in flow cell configurations to report half-cell potential.[228] In recent years, some novel diagnostic systems have been developed in membrane-based electrochemical cells for the separate investigation of overpotentials induced by components and their interfaces. Xu et al. attached a membrane strip to the AEM as an ionic conductor outside the active area and linked it to an Ag/AgCl reference electrode in AEMWE (Figure 23a), which allowed the respective measurement of anode and cathode potential.[229] From the trend of the cell voltage difference (Figure 23b), it can be told that increasing cathode PTL (commercial Toray papers) thickness from T30 to T120 improved the cell performance. With the integrated reference electrode, the authors further revealed that the parameter change at cathode not only lowered the cathode overpotential but also positively influenced the anode in an indirect way (Figure 23c), which was attributed to the enhancement of the internal pressure. This example demonstrates that the current two-electrode measurement is insufficient to investigate the origin of the cell performance change when altering one parameter of the component or comparing various interface engineering methods. Recently, Hansen et al. reported a five-electrode system for CO_2 electrolysis by placing two AgBr quasi-reference electrode wires on two sides of the membrane and one Ag/AgCl reference electrode in the anolyte (Figure 23d), which identified that the optimization of cathode−membrane ion conduction was the key to effectively lower the cell voltage.[227] The five-electrode technique also reduces the complexity to model the electrolyzer and fit the data for EIS due to the additional three measurements of anode, cathode, and membrane. Other developed diagnostic systems include inserting a reference electrode through the punching of a flow plate for connection to the membrane,[228] or sandwiching a reference electrode between two membranes.[230] It should be noted that to separate anode overpotential from the electrolyzer, the placement of reference electrode, anode and cathode requires careful attention to ensure uniform current distribution and avoid convolution error. For anode engineering in PEMWE, it is also necessary to apply these diagnostic systems

to pinpoint the overpotential sources and investigate their changes through the engineering of different components and interfaces.

5.3. Ionomer-Related Engineering. Ionomer is also an important component at the triple-phase boundary in PEMWE, which is mainly responsible for proton conduction and catalyst binder. Most of the current studies focused on the effects of ionomer content on the cell performance. For instance, Bernt et al. showed that a lower ionomer content leads to a higher proton conduction resistance, while a higher ionomer content results in a higher electron conduction resistance, hindrance of catalyst connection and increased gas removal resistance.[231] The ionomer−catalyst interaction under practical conditions is less investigated, as well as the engineering of ionomer with catalysts for a more effective triple-phase boundary. Schuler et al. studied the influence of ionomer swelling with ionomer weight fraction from 3 to 18 wt % through a hydration cycle (dry → 100% rh (relative humidity) → liquid water → dry).[76] The electrical in-plane conductivity dropped drastically after equilibration in liquid water (Figure 24a), indicating that the swelling for ionomer content >3 wt % isolated the catalyst agglomerates, which led to a disconnected electrical percolation network and longer electron transfer pathways (Figure 24b). In addition, the ionomer degradation, rearrangement, and loss after long-term electrolysis requires further investigation for practical applications. The degradation rate of ionomer can be determined through the variation of surface ionomer content from X-ray photoelectron spectroscopy (XPS) and the fluoride emission rate from fluorescence spectroscopy.[106] Also, the existence of ionomer is considered to have a potential poisoning effect on the Ir-based catalyst surface, impairing the OER kinetics.[230] More practices are expected for ionomer-related engineering on ionomer itself, as well as within the electrode fabrication process (e.g., ionomer content grading) to achieve a better cell performance. Meanwhile, novel ionomer-free or self-supported electrodes have been developed recently and shown to be promising candidates for practical PEMWE applications.[150,232]

6. SUMMARY AND OUTLOOK

6.1. Summary. To make sustainable H_2 production in PEMWE a more economically competitive technology, further reduction in capital and operation costs is urgently needed in the PEMWE stack, which requires careful anode engineering to achieve the respective optimization and integration of PTL, CL, and PEM.

PTL is a major component and cost driver in current PEMWE. The use of precious metal coating and Ti-based bulk materials for PTL and BPP can endure the harsh OER environment, but also greatly adds to the capital cost. Ir-based and corrosion resistant Ti-based coatings were successfully fabricated on the anode PTL in PEMWE to lower or replace the expensive Pt or Au coating, showing high conductivity and outstanding stability. Also, attempts were made to substitute nonprecious metal coated stainless steel or copper for the costly Ti bulk. The porous structure of PTL is responsible for kinetic, ohmic and mass transport losses, especially at low catalyst loadings. An ideal trade-off should be realized between mechanical stability, mass transport, and electrical and thermal conductivity by tuning PTL structural parameters, including pore size, porosity, tortuosity, thickness, and wettability. To further improve water supply and oxygen removal at anode, pore gradients were introduced in PTL, where the pore size

and porosity gradually decreased from the BPP side to the CL side, leading to higher catalyst utilization and better cell performance. Additionally, patterned through-pores under flow field were demonstrated to be beneficial for mass transport at high reaction rates. Advanced characterization techniques, including optical, neutron, and X-ray imaging, were employed in PEMWE to visualize the bubble evolution and transport process inside PTL. Optical imaging is capable of observing oxygen evolution behavior via a high-speed camera and transparent flow fields, such as nucleation sites, growth rate, detachment diameter, and flow pattern. Gas/water distribution and its dynamic changes can be characterized by neutron radiography, which provides high sensitivity and resolution. In addition, X-ray CT and radiography enables the capture of 3D PTL morphology, as well as the visualization of two-phase transport process in PEMWE. Modeling methods, involving VOF, PNM, and LBM, are powerful tools developed for the simulation and prediction of PTL transport properties.

Apart from improvement of each component in PEMWE anode, proper engineering of PEM/CL interface and PTL/CL interface can also remarkably enhance the PEMWE durability and efficiency. The construction of 3D PEM/CL interface can greatly enlarge the interfacial area, which further leads to lower contact resistance and higher catalyst utilization. In another light, not only does an additional layer between PEM and CL help accelerated transport of protons but the high conductivity of additional layer will also promote in-plane electron transport in catalyst layer as well. The direct membrane deposition method has proved to be effective in AEMWE and PEMFC, as well as PEMWE cathode, while successful application to PEMWE anode may require the development of PTL with appropriate MPL. In general, the PTL/CL interface has worse interfacial contact than PEM/CL interface, since the contact is limited by the uncontinuous PTL surface. Additionally, a thin CL with low catalyst loading can cause gaps and voids in CL, making the contact between PTL and CL even worse. Integration of an appropriate support material, such as doped TiO_2 can thicken the anode CL, favoring enhanced PTL/CL contact and catalyst utilization. Tuning the morphology of CL and PTL is another effective approach, including deposition of IrO_2 nanofibers at the interface, fabrication of catalyst nanosheet, laser ablation of PTL surface, etc.

As an inevitable part in PEMWE assembly, catalyst coating techniques are also important. Direct spray is a widely used traditional method for catalyst coating, while the membrane deformation and swelling may lead to coating inhomogeneity. Decal method can avoid membrane swelling, while it contains several consecutive steps, adding to its cost and complexity. To construct CL with special structure, it is viable to grow the CL material on a substrate and transfer to PEM through decal method. RSDT is a new lab-scale technology that combines synthesis and catalyst deposition in one step. By optimized tuning of the precursor concentration, flow rate, and quench distance, CL of ultralow loading and outstanding durability can be fabricated by RSDT. R2R coating is the most promising technique to be applied for large scale PEMWE fabrication. Since alcohols in ink is in direct contact with membrane, swelling should be carefully controlled in this method. Even though CCM is the dominant configuration in PEMWE, several coating techniques for GDE have been also proposed as promising alternatives. Direct spray is a simple way to coat catalyst on PTL, while sputtering deposition can coat CL of

much lower loading and higher homogeneity. Besides, sputtering can save precious metal usage, since only the outermost surface of PTL is coated. On the contrary, though the CL coated by electrodeposition can also be even and well controlled, the catalyst is coated all over the PTL.

6.2. Outlook. For now, two types of electrode configurations are the most commonly used, namely CCM and GDE. The comparison between CCM and GDE is displayed in some works, but which one is more suitable for practical PEMWE applications may conform to specific electrode fabrication methods, catalyst loadings, and operation conditions. Simultaneous engineering of PTL/CL interface and PEM/CL interface is expected to integrate the advantages of both CCM and GDE and overcome the respective limitations. To pinpoint the sources of cell voltage loss, novel overpotential diagnostic systems are developed for the separation of the anode potential from the electrolyzer, which should be extensively applied in future research to investigate the effects of a single parameter change on the different parts of the cell. In addition, to bridge the gap between lab-scale performance and practical applications, while studying the intrinsic catalyst degradation mechanism is prioritized,[233] the stability of the developed PTL, PTL/CL interface and PEM/CL interface by various fabrication methods should also be further investigated. It also relates to the correct measurement of the long-term stability of OER catalyst since these components may fail before the catalyst. Ionomer is another important component in the electrode, whose existence in PEMWE requires further engineering or better alternatives. Moreover, flow field geometry and design in BPP have noticeable influence on the mass transfer and electrical conductivity at PTL/BPP interface,[234,235] which also needs to be carefully studied and optimized. Given the raising attention to large-scale PEMWE operating at high current densities, we believe the summarized anode engineering strategies in this review will provide important clues to design and integrate the key anode components, pushing the PEMWE to the next stage.

AUTHOR INFORMATION

Corresponding Author

Haotian Wang − *Department of Chemical and Biomolecular Engineering, Rice University, Houston, Texas 77005, United States; Department of Materials Science and NanoEngineering and Department of Chemistry, Rice University, Houston, Texas 77005, United States;* ⓞ orcid.org/0000-0002-3552-8978; Email: htwang@rice.edu

Authors

Chang Qiu − *Department of Chemical and Biomolecular Engineering, Rice University, Houston, Texas 77005, United States*

Zikai Xu − *Division of Chemistry and Chemical Engineering, California Institute of Technology, Pasadena, California 91125, United States;* ⓞ orcid.org/0000-0002-4580-0330

Feng-Yang Chen − *Department of Chemical and Biomolecular Engineering, Rice University, Houston, Texas 77005, United States;* ⓞ orcid.org/0000-0002-3113-383X

Complete contact information is available at:
https://pubs.acs.org/10.1021/acscatal.3c05162

Author Contributions

#C. Q. and Z. X. contributed equally.

Notes

NOMENCLATURE

PEM, Proton Exchange Membrane; WE, Water Electrolyzer; PTL, Porous Transport Layer; CL, Catalyst Layer; AWE, Alkaline Water Electrolyzer; AEM, Anion Exchange Membrane; MEA, Membrane Electrode Assembly; OER, Oxygen Evolution Reaction; BPP, Bipolar Plates; GDL, Gas Diffusion Layer; LGDL, Liquid/Gas Diffusion Layer; CCM, Catalyst-Coated Membrane; EIS, Electrochemical Impedance Spectroscopy; PTFE, Polytetrafluoroethylene; FC, Fuel Cell; CT, Computed Tomography; PTP, Patterned Through-Pores; TT-LGDL, Thin/Tunable Liquid/Gas Diffusion Layer; GDE, Gas Diffusion Electrode; VOF, Volume of Fluid; PNM, Pore Network Modeling; LBM, Lattice Boltzmann Method; ECSA, Electrochemical Surface Area; AAO, Anodic Aluminum Oxide; PDMS, Polydimethylsiloxane; GTA, Gradient Tapered Array; NSTF, Nanostructure Thin Film; MCTS, Microstructured Catalyst Transfer Substrate; AuNL, Gold Nanolayer; NPUF, Nanoporous Ultrathin Film; DMD, Direct Membrane Deposition; MPL, Micro Porous Layer; CCLGDL, Catalyst-Coated Liquid/Gas Diffusion Layer; HFR, High Frequency Resistance; npIr-NS, Nanoporous Ir Nanosheet; IPA, Isopropyl Alcohol; R2R, Roll to Roll; SDC, SlotDie Coating; FTO, Fluorine-Doped Tin Oxide; RSDT, Reactive Spray Deposition Technology; PTE, Porous Transport Electrode; EIROF, Electrodeposited IrO_2 Film; PVD, Physical Vapor Deposition

REFERENCES

(1) Chatenet, M.; Pollet, B. G.; Dekel, D. R.; Dionigi, F.; Deseure, J.; Millet, P.; Braatz, R. D.; Bazant, M. Z.; Eikerling, M.; Staffell, I.; Balcombe, P.; Shao-Horn, Y.; Schäfer, H. Water electrolysis: from textbook knowledge to the latest scientific strategies and industrial developments. *Chem. Soc. Rev.* **2022**, *51* (11), 4583−4762.

(2) Jacobson, T. A.; Kler, J. S.; Hernke, M. T.; Braun, R. K.; Meyer, K. C.; Funk, W. E. Direct human health risks of increased atmospheric carbon dioxide. *Nat. Sustain.* **2019**, *2* (8), 691−701.

(3) Baker, H. S.; Millar, R. J.; Karoly, D. J.; Beyerle, U.; Guillod, B. P.; Mitchell, D.; Shiogama, H.; Sparrow, S.; Woollings, T.; Allen, M. R. Higher CO_2 concentrations increase extreme event risk in a 1.5 °C world. *Nat. Clim. Change* **2018**, *8* (7), 604−608.

(4) De Luna, P.; Hahn, C.; Higgins, D.; Jaffer, S. A.; Jaramillo, T. F.; Sargent, E. H. What would it take for renewably powered electrosynthesis to displace petrochemical processes? *Science* **2019**, *364* (6438), No. eaav3506.

(5) Xie, H.; Zhao, Z.; Liu, T.; Wu, Y.; Lan, C.; Jiang, W.; Zhu, L.; Wang, Y.; Yang, D.; Shao, Z. A membrane-based seawater electrolyser for hydrogen generation. *Nature* **2022**, *612* (7941), 673−678.

(6) Xia, C.; Xia, Y.; Zhu, P.; Fan, L.; Wang, H. Direct electrosynthesis of pure aqueous H_2O_2 solutions up to 20% by weight using a solid electrolyte. *Science* **2019**, *366* (6462), 226−231.

(7) Li, F.; Thevenon, A.; Rosas-Hernandez, A.; Wang, Z.; Li, Y.; Gabardo, C. M.; Ozden, A.; Dinh, C. T.; Li, J.; Wang, Y.; Edwards, J. P.; Xu, Y.; McCallum, C.; Tao, L.; Liang, Z.-Q.; Luo, M.; Wang, X.; Li, H.; O'Brien, C. P.; Tan, C.-S.; Nam, D.-H.; Quintero-Bermudez, R.; Zhuang, T.-T.; Li, Y. C.; Han, Z.; Britt, R. D.; Sinton, D.; Agapie, T.; Peters, J. C.; Sargent, E. H. Molecular tuning of CO_2-to-ethylene conversion. *Nature* **2020**, *577* (7791), 509−513.

(8) Du, H. L.; Chatti, M.; Hodgetts, R. Y.; Cherepanov, P. V.; Nguyen, C. K.; Matuszek, K.; MacFarlane, D. R.; Simonov, A. N. Electroreduction of nitrogen with almost 100% current-to-ammonia efficiency. *Nature* **2022**, *609* (7928), 722−727.

(9) Li, L.; Wang, P.; Shao, Q.; Huang, X. Metallic nanostructures with low dimensionality for electrochemical water splitting. *Chem. Soc. Rev.* **2020**, *49* (10), 3072−3106.

(10) Yu, Z. Y.; Duan, Y.; Feng, X. Y.; Yu, X.; Gao, M. R.; Yu, S. H. Clean and Affordable Hydrogen Fuel from Alkaline Water Splitting: Past, Recent Progress, and Future Prospects. *Adv. Mater.* **2021**, *33* (31), 2007100.

(11) Chen, F.-Y.; Wu, Z.-Y.; Adler, Z.; Wang, H. Stability challenges of electrocatalytic oxygen evolution reaction: From mechanistic understanding to reactor design. *Joule* **2021**, *5* (7), 1704−1731.

(12) Du, N.; Roy, C.; Peach, R.; Turnbull, M.; Thiele, S.; Bock, C. Anion-Exchange Membrane Water Electrolyzers. *Chem. Rev.* **2022**, *122* (13), 11830−11895.

(13) Santoro, C.; Lavacchi, A.; Mustarelli, P.; Di Noto, V.; Elbaz, L.; Dekel, D. R.; Jaouen, F. What is Next in Anion-Exchange Membrane Water Electrolyzers? Bottlenecks, Benefits, and Future. *ChemSusChem* **2022**, *15* (8), No. e202200027.

(14) Hrbek, T.; Kúš, P.; Kosto, Y.; Rodríguez, M. G.; Matolínová, I. Magnetron-sputtered thin-film catalyst with low-Ir-Ru content for water electrolysis: Long-term stability and degradation analysis. *J. Power Sources* **2023**, *556*, 232375.

(15) Wu, Z.-Y.; Chen, F.-Y.; Li, B.; Yu, S.-W.; Finfrock, Y. Z.; Meira, D. M.; Yan, Q.-Q.; Zhu, P.; Chen, M.-X.; Song, T.-W.; Yin, Z.; Liang, H.-W.; Zhang, S.; Wang, G.; Wang, H. Non-iridium-based electrocatalyst for durable acidic oxygen evolution reaction in proton exchange membrane water electrolysis. *Nat. Mater.* **2023**, *22* (1), 100−108.

(16) King, L. A.; Hubert, M. A.; Capuano, C.; Manco, J.; Danilovic, N.; Valle, E.; Hellstern, T. R.; Ayers, K.; Jaramillo, T. F. A non-precious metal hydrogen catalyst in a commercial polymer electrolyte membrane electrolyser. *Nat. Nanotechnol.* **2019**, *14* (11), 1071−1074.

(17) Sun, S.; Shao, Z.; Yu, H.; Li, G.; Yi, B. Investigations on degradation of the long-term proton exchange membrane water electrolysis stack. *J. Power Sources* **2014**, *267*, 515−520.

(18) Shiva Kumar, S.; Lim, H. An overview of water electrolysis technologies for green hydrogen production. *Energy Rep.* **2022**, *8*, 13793−13813.

(19) IEA. *Global Hydrogen Review 2022*; International Energy Agency: Paris, 2022; https://www.iea.org/reports/global-hydrogen-review-2022 (accessed 2023-10-15).

(20) Chen, Y.; Liu, C.; Xu, J.; Xia, C.; Wang, P.; Xia, B. Y.; Yan, Y.; Wang, X. Key Components and Design Strategy for a Proton Exchange Membrane Water Electrolyzer. *Small Struct.* **2023**, *4* (6), 2200130.

(21) Jin, H.; Liu, X.; An, P.; Tang, C.; Yu, H.; Zhang, Q.; Peng, H. J.; Gu, L.; Zheng, Y.; Song, T.; Davey, K.; Paik, U.; Dong, J.; Qiao, S.-Z. Dynamic rhenium dopant boosts ruthenium oxide for durable oxygen evolution. *Nat. Commun.* **2023**, *14* (1), 354.

(22) Hao, S.; Liu, M.; Pan, J.; Liu, X.; Tan, X.; Xu, N.; He, Y.; Lei, L.; Zhang, X. Dopants fixation of Ruthenium for boosting acidic oxygen evolution stability and activity. *Nat. Commun.* **2020**, *11* (1), 5368.

(23) Gao, J.; Liu, Y.; Liu, B.; Huang, K. W. Progress of Heterogeneous Iridium-Based Water Oxidation Catalysts. *ACS Nano* **2022**, *16* (11), 17761−17777.

(24) IRENA. *Green Hydrogen Cost Reduction: Scaling up Electrolysers to Meet the 1.5°C Climate Goal*; International Renewable Energy Agency: Abu Dhabi, 2020; https://www.irena.org/publications/2020/Dec/Green-hydrogen-cost-reduction (accessed 2023-10-15).

(25) Wang, Y.; Pang, Y.; Xu, H.; Martinez, A.; Chen, K. S. PEM Fuel cell and electrolysis cell technologies and hydrogen infrastructure development - a review. *Energy Environ. Sci.* **2022**, *15* (6), 2288−2328.

(26) Doan, T. L.; Lee, H. E.; Shah, S. S. H.; Kim, M.; Kim, C. H.; Cho, H. S.; Kim, T. A review of the porous transport layer in polymer

electrolyte membrane water electrolysis. *Int. J. Energy Res.* **2021**, *45* (10), 14207−14220.

(27) Lopata, J.; Kang, Z.; Young, J.; Bender, G.; Weidner, J. W.; Shimpalee, S. Effects of the Transport/Catalyst Layer Interface and Catalyst Loading on Mass and Charge Transport Phenomena in Polymer Electrolyte Membrane Water Electrolysis Devices. *J. Electrochem. Soc.* **2020**, *167* (6), 064507.

(28) Guo, X.; Liu, Y.; Zhang, X.; Ju, Z.; Li, Y.; Mitlin, D.; Yu, G. Revealing the Solid-State Electrolyte Interfacial Stability Model with Na-K Liquid Alloy. *Angew. Chem., Int. Ed.* **2022**, *61* (29), No. e202203409.

(29) Zahiri, B.; Patra, A.; Kiggins, C.; Yong, A. X. B.; Ertekin, E.; Cook, J. B.; Braun, P. V. Revealing the role of the cathode-electrolyte interface on solid-state batteries. *Nat. Mater.* **2021**, *20* (10), 1392−1400.

(30) Agresti, A.; Pazniak, A.; Pescetelli, S.; Di Vito, A.; Rossi, D.; Pecchia, A.; Auf der Maur, M.; Liedl, A.; Larciprete, R.; Kuznetsov, D. V.; Saranin, D.; Di Carlo, A. Titanium-carbide MXenes for work function and interface engineering in perovskite solar cells. *Nat. Mater.* **2019**, *18* (11), 1228−1234.

(31) Zhou, H.; Chen, Q.; Li, G.; Luo, S.; Song, T. B.; Duan, H. S.; Hong, Z.; You, J.; Liu, Y.; Yang, Y. Photovoltaics. Interface engineering of highly efficient perovskite solar cells. *Science* **2014**, *345* (6196), 542−546.

(32) Bian, W.; Wu, W.; Wang, B.; Tang, W.; Zhou, M.; Jin, C.; Ding, H.; Fan, W.; Dong, Y.; Li, J.; Ding, D. Revitalizing interface in protonic ceramic cells by acid etch. *Nature* **2022**, *604* (7906), 479−485.

(33) Fan, J.; Chen, M.; Zhao, Z.; Zhang, Z.; Ye, S.; Xu, S.; Wang, H.; Li, H. Bridging the gap between highly active oxygen reduction reaction catalysts and effective catalyst layers for proton exchange membrane fuel cells. *Nat. Energy* **2021**, *6* (5), 475−486.

(34) Breitwieser, M.; Klingele, M.; Vierrath, S.; Zengerle, R.; Thiele, S. Tailoring the Membrane-Electrode Interface in PEM Fuel Cells: A Review and Perspective on Novel Engineering Approaches. *Adv. Energy Mater.* **2018**, *8* (4), 1701257.

(35) Wan, L.; Xu, Z.; Xu, Q.; Wang, P.; Wang, B. Overall design of novel 3D-ordered MEA with drastically enhanced mass transport for alkaline electrolyzers. *Energy Environ. Sci.* **2022**, *15* (5), 1882−1892.

(36) Liu, H.; Kang, X.; Zhao, T.; Zhang, Z.; Ge, S.; Hu, S.; Luo, Y.; Yang, F.; Li, S.-H.; Sun, C.; Yu, Q.; Cheng, H.-M.; Liu, B. Engineering membrane electrode assembly for advanced polymer electrolyte water electrolyzer. *Sci. China Mater.* **2022**, *65* (12), 3243−3272.

(37) Mo, J.; Kang, Z.; Retterer, S. T.; Cullen, D. A.; Toops, T. J.; Green, J. B.; Mench, M. M.; Zhang, F.-Y. Discovery of true electrochemical reactions for ultrahigh catalyst mass activity in water splitting. *Sci. Adv.* **2016**, *2* (11), No. e1600690.

(38) Gao, J.; Tao, H.; Liu, B. Progress of Nonprecious-Metal-Based Electrocatalysts for Oxygen Evolution in Acidic Media. *Adv. Mater.* **2021**, *33* (31), No. e2003786.

(39) Jiao, S.; Fu, X.; Wang, S.; Zhao, Y. Perfecting electrocatalysts via imperfections: towards the large-scale deployment of water electrolysis technology. *Energy Environ. Sci.* **2021**, *14* (4), 1722−1770.

(40) Song, J.; Wei, C.; Huang, Z. F.; Liu, C.; Zeng, L.; Wang, X.; Xu, Z. J. A review on fundamentals for designing oxygen evolution electrocatalysts. *Chem. Soc. Rev.* **2020**, *49* (7), 2196−2214.

(41) Song, H. J.; Yoon, H.; Ju, B.; Kim, D. W. Highly Efficient Perovskite-Based Electrocatalysts for Water Oxidation in Acidic Environments: A Mini Review. *Adv. Energy Mater.* **2021**, *11* (27), 2002428.

(42) Shi, Q.; Zhu, C.; Du, D.; Lin, Y. Robust noble metal-based electrocatalysts for oxygen evolution reaction. *Chem. Soc. Rev.* **2019**, *48* (12), 3181−3192.

(43) Yang, Y.; Li, P.; Zheng, X.; Sun, W.; Dou, S. X.; Ma, T.; Pan, H. Anion-exchange membrane water electrolyzers and fuel cells. *Chem. Soc. Rev.* **2022**, *51* (23), 9620−9693.

(44) Mo, J.; Steen, S. M.; Zhang, F.-Y.; Toops, T. J.; Brady, M. P.; Green, J. B. Electrochemical investigation of stainless steel corrosion

in a proton exchange membrane electrolyzer cell. *Int. J. Hydrog. Energy* **2015**, *40* (36), 12506−12511.

(45) Mo, J.; Steen, S.; Kang, Z.; Yang, G.; Taylor, D. A.; Li, Y.; Toops, T. J.; Brady, M. P.; Retterer, S. T.; Cullen, D. A.; Green, J. B.; Zhang, F.-Y. Study on corrosion migrations within catalyst-coated membranes of proton exchange membrane electrolyzer cells. *Int. J. Hydrog. Energy* **2017**, *42* (44), 27343−27349.

(46) Rakousky, C.; Reimer, U.; Wippermann, K.; Carmo, M.; Lueke, W.; Stolten, D. An analysis of degradation phenomena in polymer electrolyte membrane water electrolysis. *J. Power Sources* **2016**, *326*, 120−128.

(47) Weiß, A.; Siebel, A.; Bernt, M.; Shen, T. H.; Tileli, V.; Gasteiger, H. A. Impact of Intermittent Operation on Lifetime and Performance of a PEM Water Electrolyzer. *J. Electrochem. Soc.* **2019**, *166* (8), F487−F497.

(48) Liu, C.; Shviro, M.; Gago, A. S.; Zaccarine, S. F.; Bender, G.; Gazdzicki, P.; Morawietz, T.; Biswas, I.; Rasinski, M.; Everwand, A.; Schierholz, R.; Pfeilsticker, J.; Müller, M.; Lopes, P. P.; Eichel, R.-A.; Pivovar, B.; Pylypenko, S.; Friedrich, K. A.; Lehnert, W.; Carmo, M. Exploring the Interface of Skin-Layered Titanium Fibers for Electrochemical Water Splitting. *Adv. Energy Mater.* **2021**, *11* (8), 2002926.

(49) Doan, T. L.; Lee, H. E.; Kim, M.; Cho, W. C.; Cho, H. S.; Kim, T. Influence of IrO$_2$/TiO$_2$ coated titanium porous transport layer on the performance of PEM water electrolysis. *J. Power Sources* **2022**, *533*, 231370.

(50) Fan, Z.; Yu, H.; Jiang, G.; Yao, D.; Sun, S.; Chi, J.; Qin, B.; Shao, Z. Low precious metal loading porous transport layer coating and anode catalyst layer for proton exchange membrane water electrolysis. *Int. J. Hydrog. Energy* **2022**, *47* (44), 18963−18971.

(51) Wakayama, H.; Yamazaki, K. Low-Cost Bipolar Plates of Ti$_4$O$_7$-Coated Ti for Water Electrolysis with Polymer Electrolyte Membranes. *ACS Omega* **2021**, *6* (6), 4161−4166.

(52) Liu, Y.; Huang, S.; Wang, D.; Zhang, H.; Shan, D.; Peng, S.; Shen, G.; Wang, L.; Wang, X. Modifying Ti-Based Gas Diffusion Layer Passivation for Polymer Electrolyte Membrane Water Electrolysis via Electrochemical Nitridation. *ACS Appl. Mater. Interfaces* **2022**, *14* (13), 15728−15735.

(53) Toops, T. J.; Brady, M. P.; Zhang, F.-Y.; Meyer, H. M.; Ayers, K.; Roemer, A.; Dalton, L. Evaluation of nitrided titanium separator plates for proton exchange membrane electrolyzer cells. *J. Power Sources* **2014**, *272*, 954−960.

(54) Liu, C.; Shviro, M.; Bender, G.; Gago, A. S.; Morawietz, T.; Dzara, M. J.; Biswas, I.; Gazdzicki, P.; Kang, Z.; Zaccarine, S. F.; Pylypenko, S.; Friedrich, K. A.; Carmo, M.; Lehnert, W. Degradation Effects at the Porous Transport Layer/Catalyst Layer Interface in Polymer Electrolyte Membrane Water Electrolyzer. *J. Electrochem. Soc.* **2023**, *170* (3), 034508.

(55) Stiber, S.; Sata, N.; Morawietz, T.; Ansar, S. A.; Jahnke, T.; Lee, J. K.; Bazylak, A.; Fallisch, A.; Gago, A. S.; Friedrich, K. A. A high-performance, durable and low-cost proton exchange membrane electrolyser with stainless steel components. *Energy Environ. Sci.* **2022**, *15* (1), 109−122.

(56) Lettenmeier, P.; Wang, R.; Abouatallah, R.; Saruhan, B.; Freitag, O.; Gazdzicki, P.; Morawietz, T.; Hiesgen, R.; Gago, A. S.; Friedrich, K. A. Low-Cost and Durable Bipolar Plates for Proton Exchange Membrane Electrolyzers. *Sci. Rep.* **2017**, *7*, 44035.

(57) Daudt, N. F.; Hackemüller, F. J.; Bram, M. Powder metallurgical production of 316L stainless steel/niobium composites for Proton Exchange membrane electrolysis cells. *Powder Metall.* **2019**, *62* (3), 176−185.

(58) Rojas, N.; Sánchez-Molina, M.; Sevilla, G.; Amores, E.; Almandoz, E.; Esparza, J.; Cruz Vivas, M. R.; Colominas, C. Coated stainless steels evaluation for bipolar plates in PEM water electrolysis conditions. *Int. J. Hydrog. Energy* **2021**, *46* (51), 25929−25943.

(59) Kellenberger, A.; Vaszilcsin, N.; Duca, D.; Dan, M. L.; Duteanu, N.; Stiber, S.; Morawietz, T.; Biswas, I.; Ansar, S. A.; Gazdzicki, P.; Wirkert, F. J.; Roth, J.; Rost, U.; Brodmann, M.; Gago, A. S.; Friedrich, K. A. Towards Replacing Titanium with Copper in the

Bipolar Plates for Proton Exchange Membrane Water Electrolysis. *Materials* **2022**, *15* (5), 1628.

(60) Pushkarev, A. S.; Pushkareva, I. V.; Solovyev, M. A.; Prokop, M.; Bystron, T.; Rajagopalan, S. K.; Bouzek, K.; Grigoriev, S. A. On the influence of porous transport layers parameters on the performances of polymer electrolyte membrane water electrolysis cells. *Electrochim. Acta* **2021**, *399*, 139436.

(61) Peng, X.; Satjaritanun, P.; Taie, Z.; Wiles, L.; Keane, A.; Capuano, C.; Zenyuk, I. V.; Danilovic, N. Insights into Interfacial and Bulk Transport Phenomena Affecting Proton Exchange Membrane Water Electrolyzer Performance at Ultra-Low Iridium Loadings. *Adv. Sci.* **2021**, *8* (21), No. e2102950.

(62) Parra-Restrepo, J.; Bligny, R.; Dillet, J.; Didierjean, S.; Stemmelen, D.; Moyne, C.; Degiovanni, A.; Maranzana, G. Influence of the porous transport layer properties on the mass and charge transfer in a segmented PEM electrolyzer. *Int. J. Hydrog. Energy* **2020**, *45* (15), 8094−8106.

(63) Razmjooei, F.; Morawietz, T.; Taghizadeh, E.; Hadjixenophontos, E.; Mues, L.; Gerle, M.; Wood, B. D.; Harms, C.; Gago, A. S.; Ansar, S. A.; Friedrich, K. A. Increasing the performance of an anion-exchange membrane electrolyzer operating in pure water with a nickel-based microporous layer. *Joule* **2021**, *5* (7), 1776−1799.

(64) Omrani, R.; Shabani, B. Review of gas diffusion layer for proton exchange membrane-based technologies with a focus on unitised regenerative fuel cells. *Int. J. Hydrog. Energy* **2019**, *44* (7), 3834−3860.

(65) Siracusano, S.; Di Blasi, A.; Baglio, V.; Brunaccini, G.; Briguglio, N.; Stassi, A.; Ornelas, R.; Trifoni, E.; Antonucci, V.; Aricò, A. S. Optimization of components and assembling in a PEM electrolyzer stack. *Int. J. Hydrog. Energy* **2011**, *36* (5), 3333−3339.

(66) Weber, C. C.; Schuler, T.; De Bruycker, R.; Gubler, L.; Büchi, F. N.; De Angelis, S. On the role of porous transport layer thickness in polymer electrolyte water electrolysis. *J. Power Sources Adv.* **2022**, *15*, 100095.

(67) Li, H.; Fujigaya, T.; Nakajima, H.; Inada, A.; Ito, K. Optimum structural properties for an anode current collector used in a polymer electrolyte membrane water electrolyzer operated at the boiling point of water. *J. Power Sources* **2016**, *332*, 16−23.

(68) Kang, Z.; Alia, S. M.; Young, J. L.; Bender, G. Effects of various parameters of different porous transport layers in proton exchange membrane water electrolysis. *Electrochim. Acta* **2020**, *354*, 136641.

(69) Zhao, B.; Lee, C.; Lee, J. K.; Fahy, K. F.; LaManna, J. M.; Baltic, E.; Jacobson, D. L.; Hussey, D. S.; Bazylak, A. Superhydrophilic porous transport layer enhances efficiency of polymer electrolyte membrane electrolyzers. *Cell Rep. Phys. Sci.* **2021**, *2* (10), 100580.

(70) Lim, A.; Jeong, H.-Y.; Lim, Y.; Kim, J. Y.; Park, H. Y.; Jang, J. H.; Sung, Y.-E.; Kim, J. M.; Park, H. S. Amphiphilic Ti porous transport layer for highly effective PEM unitized regenerative fuel cells. *Sci. Adv.* **2021**, *7* (13), No. eabf7866.

(71) Zhang, C.; Xu, Z.; Han, N.; Tian, Y.; Kallio, T.; Yu, C.; Jiang, L. Superaerophilic/superaerophobic cooperative electrode for efficient hydrogen evolution reaction via enhanced mass transfer. *Sci. Adv.* **2023**, *9* (3), No. eadd6978.

(72) Yang, Y.; Zhou, X.; Li, B.; Zhang, C. Recent progress of the gas diffusion layer in proton exchange membrane fuel cells: Material and structure designs of microporous layer. *Int. J. Hydrog. Energy* **2021**, *46* (5), 4259−4282.

(73) Zhang, J.; Wang, B.; Jin, J.; Yang, S.; Li, G. A review of the microporous layer in proton exchange membrane fuel cells: Materials and structural designs based on water transport mechanism. *Renew. Sust. Energy Rev.* **2022**, *156*, 111998.

(74) Lettenmeier, P.; Kolb, S.; Burggraf, F.; Gago, A. S.; Friedrich, K. A. Towards developing a backing layer for proton exchange membrane electrolyzers. *J. Power Sources* **2016**, *311*, 153−158.

(75) Lettenmeier, P.; Kolb, S.; Sata, N.; Fallisch, A.; Zielke, L.; Thiele, S.; Gago, A. S.; Friedrich, K. A. Comprehensive investigation of novel pore-graded gas diffusion layers for high-performance and cost-effective proton exchange membrane electrolyzers. *Energy Environ. Sci.* **2017**, *10* (12), 2521−2533.

(76) Schuler, T.; Ciccone, J. M.; Krentscher, B.; Marone, F.; Peter, C.; Schmidt, T. J.; Büchi, F. N. Hierarchically Structured Porous Transport Layers for Polymer Electrolyte Water Electrolysis. *Adv. Energy Mater.* **2020**, *10* (2), 1903216.

(77) Stiber, S.; Balzer, H.; Wierhake, A.; Wirkert, F. J.; Roth, J.; Rost, U.; Brodmann, M.; Lee, J. K.; Bazylak, A.; Waiblinger, W.; Gago, A. S.; Friedrich, K. A. Porous Transport Layers for Proton Exchange Membrane Electrolysis Under Extreme Conditions of Current Density, Temperature, and Pressure. *Adv. Energy Mater.* **2021**, *11* (33), 2100630.

(78) Kim, P. J.; Lee, J. K.; Lee, C. H.; Fahy, K. F.; Shrestha, P.; Krause, K.; Shafaque, H. W.; Bazylak, A. Tailoring catalyst layer interface with titanium mesh porous transport layers. *Electrochim. Acta* **2021**, *373*, 137879.

(79) Lee, J. K.; Lee, C.; Fahy, K. F.; Kim, P. J.; Krause, K.; LaManna, J. M.; Baltic, E.; Jacobson, D. L.; Hussey, D. S.; Bazylak, A. Accelerating Bubble Detachment in Porous Transport Layers with Patterned Through-Pores. *ACS Appl. Energy Mater.* **2020**, *3* (10), 9676−9684.

(80) Kang, Z.; Yu, S.; Yang, G.; Li, Y.; Bender, G.; Pivovar, B. S.; Green, J. B.; Zhang, F.-Y. Performance improvement of proton exchange membrane electrolyzer cells by introducing in-plane transport enhancement layers. *Electrochim. Acta* **2019**, *316*, 43−51.

(81) Hackemüller, F. J.; Borgardt, E.; Panchenko, O.; Müller, M.; Bram, M. Manufacturing of Large-Scale Titanium-Based Porous Transport Layers for Polymer Electrolyte Membrane Electrolysis by Tape Casting. *Adv. Eng. Mater.* **2019**, *21* (6), 1801201.

(82) Lee, J. K.; Lau, G. Y.; Sabharwal, M.; Weber, A. Z.; Peng, X.; Tucker, M. C. Titanium porous-transport layers for PEM water electrolysis prepared by tape casting. *J. Power Sources* **2023**, *559*, 232606.

(83) Satjaritanun, P.; O'Brien, M.; Kulkarni, D.; Shimpalee, S.; Capuano, C.; Ayers, K. E.; Danilovic, N.; Parkinson, D. Y.; Zenyuk, I. V. Observation of Preferential Pathways for Oxygen Removal through Porous Transport Layers of Polymer Electrolyte Water Electrolyzers. *iScience* **2020**, *23* (12), 101783.

(84) Zlobinski, M.; Schuler, T.; Büchi, F. N.; Schmidt, T. J.; Boillat, P. Transient and Steady State Two-Phase Flow in Anodic Porous Transport Layer of Proton Exchange Membrane Water Electrolyzer. *J. Electrochem. Soc.* **2020**, *167* (8), 084509.

(85) Yuan, S.; Zhao, C.; Cai, X.; An, L.; Shen, S.; Yan, X.; Zhang, J. Bubble evolution and transport in PEM water electrolysis: Mechanism, impact, and management. *Prog. Energy Combust. Sci.* **2023**, *96*, 101075.

(86) Angulo, A.; van der Linde, P.; Gardeniers, H.; Modestino, M.; Fernández Rivas, D. Influence of Bubbles on the Energy Conversion Efficiency of Electrochemical Reactors. *Joule* **2020**, *4* (3), 555−579.

(87) Mo, J.; Kang, Z.; Yang, G.; Li, Y.; Retterer, S. T.; Cullen, D. A.; Toops, T. J.; Bender, G.; Pivovar, B. S.; Green, J. B.; Zhang, F.-Y. In situ investigation on ultrafast oxygen evolution reactions of water splitting in proton exchange membrane electrolyzer cells. *J. Mater. Chem. A* **2017**, *5* (35), 18469−18475.

(88) Li, Y.; Kang, Z.; Mo, J.; Yang, G.; Yu, S.; Talley, D. A.; Han, B.; Zhang, F.-Y. In-situ investigation of bubble dynamics and two-phase flow in proton exchange membrane electrolyzer cells. *Int. J. Hydrog. Energy* **2018**, *43* (24), 11223−11233.

(89) Majasan, J. O.; Cho, J. I. S.; Dedigama, I.; Tsaoulidis, D.; Shearing, P.; Brett, D. J. L. Two-phase flow behaviour and performance of polymer electrolyte membrane electrolysers: Electrochemical and optical characterisation. *Int. J. Hydrog. Energy* **2018**, *43* (33), 15659−15672.

(90) Wang, W.; Yu, S.; Li, K.; Ding, L.; Xie, Z.; Li, Y.; Yang, G.; Cullen, D. A.; Yu, H.; Kang, Z.; Wrubel, J. A.; Ma, Z.; Bender, G.; Capuano, C. B.; Keane, A.; Zhang, F.-Y. Insights into the rapid two-phase transport dynamics in different structured porous transport layers of water electrolyzers through high-speed visualization. *J. Power Sources* **2021**, *516*, 230641.

(91) Iwata, R.; Zhang, L.; Wilke, K. L.; Gong, S.; He, M.; Gallant, B. M.; Wang, E. N. Bubble growth and departure modes on wettable/

non-wettable porous foams in alkaline water splitting. *Joule* **2021**, *5* (4), 887−900.

(92) Maier, M.; Smith, K.; Dodwell, J.; Hinds, G.; Shearing, P. R.; Brett, D. J. L. Mass transport in PEM water electrolysers: A review. *Int. J. Hydrog. Energy* **2022**, *47* (1), 30−56.

(93) Panchenko, O.; Borgardt, E.; Zwaygardt, W.; Hackemüller, F. J.; Bram, M.; Kardjilov, N.; Arlt, T.; Manke, I.; Müller, M.; Stolten, D.; Lehnert, W. In-situ two-phase flow investigation of different porous transport layer for a polymer electrolyte membrane (PEM) electrolyzer with neutron spectroscopy. *J. Power Sources* **2018**, *390*, 108−115.

(94) Selamet, O. F.; Pasaogullari, U.; Spernjak, D.; Hussey, D. S.; Jacobson, D. L.; Mat, M. D. Two-phase flow in a proton exchange membrane electrolyzer visualized in situ by simultaneous neutron radiography and optical imaging. *Int. J. Hydrog. Energy* **2013**, *38* (14), 5823−5835.

(95) Seweryn, J.; Biesdorf, J.; Schmidt, T. J.; Boillat, P. Communication—Neutron Radiography of the Water/Gas Distribution in the Porous Layers of an Operating Electrolyser. *J. Electrochem. Soc.* **2016**, *163* (11), F3009−F3011.

(96) Maier, M.; Dodwell, J.; Ziesche, R.; Tan, C.; Heenan, T.; Majasan, J.; Kardjilov, N.; Markötter, H.; Manke, I.; Castanheira, L.; Hinds, G.; Shearing, P. R.; Brett, D. J. L. Mass transport in polymer electrolyte membrane water electrolyser liquid-gas diffusion layers: A combined neutron imaging and X-ray computed tomography study. *J. Power Sources* **2020**, *455*, 227968.

(97) Lee, J. K.; Lee, C.; Fahy, K. F.; Kim, P. J.; LaManna, J. M.; Baltic, E.; Jacobson, D. L.; Hussey, D. S.; Stiber, S.; Gago, A. S.; Friedrich, K. A.; Bazylak, A. Spatially graded porous transport layers for gas evolving electrochemical energy conversion: High performance polymer electrolyte membrane electrolyzers. *Energy Convers. Manag.* **2020**, *226*, 113545.

(98) Leonard, E.; Shum, A. D.; Normile, S.; Sabarirajan, D. C.; Yared, D. G.; Xiao, X.; Zenyuk, I. V. Operando X-ray tomography and sub-second radiography for characterizing transport in polymer electrolyte membrane electrolyzer. *Electrochim. Acta* **2018**, *276*, 424−433.

(99) Kim, P. J.; Lee, C. H.; Lee, J. K.; Fahy, K. F.; Bazylak, A. In-Plane Transport in Water Electrolyzer Porous Transport Layers with Through Pores. *J. Electrochem. Soc.* **2020**, *167* (12), 124522.

(100) De Angelis, S.; Schuler, T.; Charalambous, M. A.; Marone, F.; Schmidt, T. J.; Büchi, F. N. Unraveling two-phase transport in porous transport layer materials for polymer electrolyte water electrolysis. *J. Mater. Chem. A* **2021**, *9* (38), 22102−22113.

(101) Satjaritanun, P.; Shimpalee, S.; Zenyuk, I. V. Gas Diffusion Layers: Experimental and Modeling Approach for Morphological and Transport Properties. *Acc. Mater. Res.* **2022**, *3* (4), 416−425.

(102) Lee, J. K.; Bazylak, A. Stochastic Generation of Sintered Titanium Powder-Based Porous Transport Layers in Polymer Electrolyte Membrane Electrolyzers and Investigation of Structural Properties. *ECS Trans.* **2017**, *80* (8), 1097−1106.

(103) Leonard, E.; Shum, A. D.; Danilovic, N.; Capuano, C.; Ayers, K. E.; Pant, L. M.; Weber, A. Z.; Xiao, X.; Parkinson, D. Y.; Zenyuk, I. V. Interfacial analysis of a PEM electrolyzer using X-ray computed tomography. *Sustain. Energy Fuels* **2020**, *4* (2), 921−931.

(104) Kulkarni, D.; Huynh, A.; Satjaritanun, P.; O'Brien, M.; Shimpalee, S.; Parkinson, D.; Shevchenko, P.; DeCarlo, F.; Danilovic, N.; Ayers, K. E.; Capuano, C.; Zenyuk, I. V. Elucidating effects of catalyst loadings and porous transport layer morphologies on operation of proton exchange membrane water electrolyzers. *Appl. Catal., B* **2022**, *308*, 121213.

(105) Bierling, M.; McLaughlin, D.; Mayerhöfer, B.; Thiele, S. Toward Understanding Catalyst Layer Deposition Processes and Distribution in Anodic Porous Transport Electrodes in Proton Exchange Membrane Water Electrolyzers. *Adv. Energy Mater.* **2023**, *13* (13), 2203636.

(106) Shangguan, Z.; Li, B.; Ming, P.; Zhang, C. Understanding the functions and modifications of interfaces in membrane electrode

assemblies of proton exchange membrane fuel cells. *J. Mater. Chem. A* **2021**, *9* (27), 15111−15139.

(107) Hegge, F.; Moroni, R.; Trinke, P.; Bensmann, B.; Hanke-Rauschenbach, R.; Thiele, S.; Vierrath, S. Three-dimensional microstructure analysis of a polymer electrolyte membrane water electrolyzer anode. *J. Power Sources* **2018**, *393*, 62−66.

(108) Aoyama, Y.; Suzuki, K.; Tabe, Y.; Chikahisa, T.; Tanuma, T. Water Transport and PEFC Performance with Different Interface Structure between Micro-Porous Layer and Catalyst Layer. *J. Electrochem. Soc.* **2016**, *163* (5), F359−F366.

(109) Lin, N.; Zausch, J. 1D multiphysics modelling of PEM water electrolysis anodes with porous transport layers and the membrane. *Chem. Eng. Sci.* **2022**, *253*, 117600.

(110) Paliwal, S.; Panda, D.; Bhaskaran, S.; Vorhauer-Huget, N.; Tsotsas, E.; Surasani, V. K. Lattice Boltzmann method to study the water-oxygen distributions in porous transport layer (PTL) of polymer electrolyte membrane (PEM) electrolyser. *Int. J. Hydrog. Energy* **2021**, *46* (44), 22747−22762.

(111) Chen, Q.; Wang, Y.; Yang, F.; Xu, H. Two-dimensional multi-physics modeling of porous transport layer in polymer electrolyte membrane electrolyzer for water splitting. *Int. J. Hydrog. Energy* **2020**, *45* (58), 32984−32994.

(112) Lee, J. K.; Lee, C. H.; Bazylak, A. Pore network modelling to enhance liquid water transport through porous transport layers for polymer electrolyte membrane electrolyzers. *J. Power Sources* **2019**, *437*, 226910.

(113) Zinser, A.; Papakonstantinou, G.; Sundmacher, K. Analysis of mass transport processes in the anodic porous transport layer in PEM water electrolysers. *Int. J. Hydrog. Energy* **2019**, *44* (52), 28077−28087.

(114) Nouri-Khorasani, A.; Tabu Ojong, E.; Smolinka, T.; Wilkinson, D. P. Model of oxygen bubbles and performance impact in the porous transport layer of PEM water electrolysis cells. *Int. J. Hydrog. Energy* **2017**, *42* (48), 28665−28680.

(115) Lee, J. K.; Bazylak, A. Stochastic Modelling For Controlling the Structure of Sintered Titanium Powder-Based Porous Transport Layers for Polymer Electrolyte Membrane Electrolyzers. *J. Electrochem. Soc.* **2019**, *166* (13), F1000−F1006.

(116) Lee, J. K.; Bazylak, A. Balancing Reactant Transport and PTL-CL Contact in PEM Electrolyzers by Optimizing PTL Design Parameters via Stochastic Pore Network Modeling. *ECS Trans.* **2019**, *92* (8), 801−820.

(117) Liu, J.; Li, M.; Yang, Y.; Schluter, N.; Mimic, D.; Schroder, D. Tailored Porous Transport Layers for Optimal Oxygen Transport in Water Electrolyzers: Combined Stochastic Reconstruction and Lattice Boltzmann Method. *ChemPhysChem* **2023**, *24* (18), No. e202300197.

(118) Xu, S.; Liao, P.; Yang, D.; Li, Z.; Ming, P.; Zhou, X. Liquid water transport in gas flow channels of PEMFCs: A review on numerical simulations and visualization experiments. *Int. J. Hydrog. Energy* **2023**, *48* (27), 10118−10143.

(119) Arbabi, F.; Montazeri, H.; Abouatallah, R.; Wang, R.; Bazylak, A. Three-Dimensional Computational Fluid Dynamics Modelling of Oxygen Bubble Transport in Polymer Electrolyte Membrane Electrolyzer Porous Transport Layers. *J. Electrochem. Soc.* **2016**, *163* (11), F3062−F3069.

(120) Lee, J. K.; Bazylak, A. Optimizing Porous Transport Layer Design Parameters via Stochastic Pore Network Modelling: Reactant Transport and Interfacial Contact Considerations. *J. Electrochem. Soc.* **2020**, *167* (1), 013541.

(121) Bhaskaran, S.; Pandey, D.; Surasani, V. K.; Tsotsas, E.; Vidakovic-Koch, T.; Vorhauer-Huget, N. LBM studies at pore scale for graded anodic porous transport layer (PTL) of PEM water electrolyzer. *Int. J. Hydrog. Energy* **2022**, *47* (74), 31551−31565.

(122) Pham, C. V.; Escalera-López, D.; Mayrhofer, K.; Cherevko, S.; Thiele, S. Essentials of High Performance Water Electrolyzers - From Catalyst Layer Materials to Electrode Engineering. *Adv. Energy Mater.* **2021**, *11* (44), 2101998.

(123) Choi, S.; Shin, S.-H.; Lee, D.-H.; Doo, G.; Lee, D. W.; Hyun, J.; Lee, J. Y.; Kim, H.-T. Enhancing the durability of hydrocarbon-

membrane-based polymer electrolyte water electrolysis using a radical scavenger-embedded interlocking interfacial layer. *J. Mater. Chem. A* **2022**, *10* (2), 789−798.

(124) Voronova, A.; Kim, H. J.; Jang, J. H.; Park, H. Y.; Seo, B. Effect of low voltage limit on degradation mechanism during high-frequency dynamic load in proton exchange membrane water electrolysis. *Int. J. Energy Res.* **2022**, *46* (9), 11867−11878.

(125) Minke, C.; Suermann, M.; Bensmann, B.; Hanke-Rauschenbach, R. Is iridium demand a potential bottleneck in the realization of large-scale PEM water electrolysis? *Int. J. Hydrog. Energy* **2021**, *46* (46), 23581−23590.

(126) Torrero, J.; Morawietz, T.; García Sanchez, D.; Galyamin, D.; Retuerto, M.; Martin-Diaconescu, V.; Rojas, S.; Alonso, J. A.; Gago, A. S.; Friedrich, K. A. High Performance and Durable Anode with 10-Fold Reduction of Iridium Loading for Proton Exchange Membrane Water Electrolysis. *Adv. Energy Mater.* **2023**, *13* (23), 2204169.

(127) Riedmayer, R.; Paren, B. A.; Schofield, L.; Shao-Horn, Y.; Mallapragada, D. Proton Exchange Membrane Electrolysis Perform-ance Targets for Achieving 2050 Expansion Goals Constrained by Iridium Supply. *Energy Fuels* **2023**, *37* (12), 8614−8623.

(128) Zaccarine, S. F.; Shviro, M.; Weker, J. N.; Dzara, M. J.; Foster, J.; Carmo, M.; Pylypenko, S. Multi-Scale Multi-Technique Character-ization Approach for Analysis of PEM Electrolyzer Catalyst Layer Degradation. *J. Electrochem. Soc.* **2022**, *169* (6), 064502.

(129) Padgett, E.; Bender, G.; Haug, A.; Lewinski, K.; Sun, F.; Yu, H.; Cullen, D.; Steinbach, A.; Alia, S. M. Catalyst Layer Resistance and Utilization in PEM Electrolysis. *J. Electrochem. Soc.* **2023**, *170* (8), 084512.

(130) Hrbek, T.; Kúš, P.; Yakovlev, Y.; Nováková, J.; Lobko, Y.; Khalakhan, I.; Matolín, V.; Matolínová, I. Sputter-etching treatment of proton-exchange membranes: Completely dry thin-film approach to low-loading catalyst-coated membranes for water electrolysis. *Int. J. Hydrog. Energy* **2020**, *45* (41), 20776−20786.

(131) Tian, B.; Li, Y.; Liu, Y.; Ning, F.; Dan, X.; Wen, Q.; He, L.; He, C.; Shen, M.; Zhou, X. Ordered Membrane Electrode Assembly with Drastically Enhanced Proton and Mass Transport for Proton Exchange Membrane Water Electrolysis. *Nano Lett.* **2023**, *23* (14), 6474−6481.

(132) Zhang, L.; Porter, T.; Guillory, S.; Chi, C.; Arges, C. G. Patterning Polymer Electrolyte Membrane for Fuel Cell and Electrolysis Applications. *ECS Trans.* **2017**, *77* (11), 1325−1335.

(133) Dong, S.; Zhang, C.; Yue, Z.; Zhang, F.; Zhao, H.; Cheng, Q.; Wang, G.; Xu, J.; Chen, C.; Zou, Z.; Dou, Z.; Yang, H. Overall Design of Anode with Gradient Ordered Structure with Low Iridium Loading for Proton Exchange Membrane Water Electrolysis. *Nano Lett.* **2022**, *22* (23), 9434−9440.

(134) Debe, M. K. Nanostructured Thin Film Electrocatalysts for PEM Fuel Cells - A Tutorial on the Fundamental Characteristics and Practical Properties of NSTF Catalysts. *ECS Trans.* **2012**, *45* (2), 47−68.

(135) Lewinski, K. A.; van der Vliet, D. F.; Luopa, S. M. NSTF Advances for PEM Electrolysis - The Effect of Alloying on Activity of NSTF Electrolyzer Catalysts and Performance of NSTF Based PEM Electrolyzers. *ECS Trans.* **2015**, *69* (17), 893−917.

(136) Song, S.; Zhang, H.; Liu, B.; Zhao, P.; Zhang, Y.; Yi, B. An Improved Catalyst-Coated Membrane Structure for PEM Water Electrolyzer. *Electrochem. Solid-State Lett.* **2007**, *10* (8), B122−B125.

(137) Yang, G.; Yu, S.; Kang, Z.; Li, Y.; Bender, G.; Pivovar, B. S.; Green, J. B.; Cullen, D. A.; Zhang, F. Y. Building Electron/Proton Nanohighways for Full Utilization of Water Splitting Catalysts. *Adv. Energy Mater.* **2020**, *10* (16), 1903871.

(138) Zeng, Y.; Guo, X.; Shao, Z.; Yu, H.; Song, W.; Wang, Z.; Zhang, H.; Yi, B. A cost-effective nanoporous ultrathin film electrode based on nanoporous gold/IrO$_2$ composite for proton exchange membrane water electrolysis. *J. Power Sources* **2017**, *342*, 947−955.

(139) Klingele, M.; Breitwieser, M.; Zengerle, R.; Thiele, S. Direct deposition of proton exchange membranes enabling high performance hydrogen fuel cells. *J. Mater. Chem. A* **2015**, *3* (21), 11239−11245.

(140) Vierrath, S.; Breitwieser, M.; Klingele, M.; Britton, B.; Holdcroft, S.; Zengerle, R.; Thiele, S. The reasons for the high power density of fuel cells fabricated with directly deposited membranes. *J. Power Sources* **2016**, *326*, 170−175.

(141) Holzapfel, P.; Bühler, M.; Van Pham, C.; Hegge, F.; Böhm, T.; McLaughlin, D.; Breitwieser, M.; Thiele, S. Directly coated membrane electrode assemblies for proton exchange membrane water electrolysis. *Electrochem. Commun.* **2020**, *110*, 106640.

(142) Bühler, M.; Klose, C.; Hegge, F.; Lickert, T.; Thiele, S. A Novel Fabrication Technique for Electrodes of PEM Water Electrolyzers. *ECS Trans.* **2017**, *80* (8), 1069−1075.

(143) Yu, S.; Li, K.; Wang, W.; Xie, Z.; Ding, L.; Kang, Z.; Wrubel, J.; Ma, Z.; Bender, G.; Yu, H.; Baxter, J.; Cullen, D. A.; Keane, A.; Ayers, K.; Capuano, C. B.; Zhang, F.-Y. Tuning Catalyst Activation and Utilization Via Controlled Electrode Patterning for Low-Loading and High-Efficiency Water Electrolyzers. *Small* **2022**, *18* (14), 2107745.

(144) Ding, L.; Wang, W.; Xie, Z.; Li, K.; Yu, S.; Capuano, C. B.; Keane, A.; Ayers, K.; Zhang, F.-Y. Highly Porous Iridium Thin Electrodes with Low Loading and Improved Reaction Kinetics for Hydrogen Generation in PEM Electrolyzer Cells. *ACS Appl. Mater. Interfaces* **2023**, *15* (20), 24284−24295.

(145) Feng, Q.; Yuan, X. Z.; Liu, G.; Wei, B.; Zhang, Z.; Li, H.; Wang, H. A review of proton exchange membrane water electrolysis on degradation mechanisms and mitigation strategies. *J. Power Sources* **2017**, *366*, 33−55.

(146) Bernt, M.; Siebel, A.; Gasteiger, H. A. Analysis of Voltage Losses in PEM Water Electrolyzers with Low Platinum Group Metal Loadings. *J. Electrochem. Soc.* **2018**, *165* (5), F305−F314.

(147) Hegge, F.; Lombeck, F.; Cruz Ortiz, E.; Bohn, L.; Von Holst, M.; Kroschel, M.; Hübner, J.; Breitwieser, M.; Strasser, P.; Vierrath, S. Efficient and Stable Low Iridium Loaded Anodes for PEM Water Electrolysis Made Possible by Nanofiber Interlayers. *ACS Appl. Energy Mater.* **2020**, *3* (9), 8276−8284.

(148) Chatterjee, S.; Peng, X.; Intikhab, S.; Zeng, G.; Kariuki, N. N.; Myers, D. J.; Danilovic, N.; Snyder, J. Nanoporous Iridium Nanosheets for Polymer Electrolyte Membrane Electrolysis. *Adv. Energy Mater.* **2021**, *11* (34), 2101438.

(149) Lee, J. K.; Schuler, T.; Bender, G.; Sabharwal, M.; Peng, X.; Weber, A. Z.; Danilovic, N. Interfacial engineering via laser ablation for high-performing PEM water electrolysis. *Appl. Energy* **2023**, *336*, 120853.

(150) Lee, J. K.; Anderson, G.; Tricker, A. W.; Babbe, F.; Madan, A.; Cullen, D. A.; Arregui-Mena, J. D.; Danilovic, N.; Mukundan, R.; Weber, A. Z.; Peng, X. Ionomer-free and recyclable porous-transport electrode for high-performing proton-exchange-membrane water electrolysis. *Nat. Commun.* **2023**, *14* (1), 4592.

(151) Fu, C.; O'Carroll, T.; Shen, S.; Luo, L.; Zhang, J.; Xu, H.; Wu, G. Metallic-Ir-based anode catalysts in PEM water electrolyzers: Achievements, challenges, and perspectives. *Curr. Opin. Electrochem.* **2023**, *38*, 101227.

(152) Moriau, L.; Smiljanić, M.; Lončar, A.; Hodnik, N. Supported iridium-based oxygen evolution reaction electrocatalysts-recent developments. *ChemCatChem.* **2022**, *14* (20), No. e202200586.

(153) Rozain, C.; Mayousse, E.; Guillet, N.; Millet, P. Influence of iridium oxide loadings on the performance of PEM water electrolysis cells: Part II - Advanced oxygen electrodes. *Appl. Catal., B* **2016**, *182*, 123−131.

(154) Puthiyapura, V. K.; Pasupathi, S.; Su, H.; Liu, X.; Pollet, B.; Scott, K. Investigation of supported IrO$_2$ as electrocatalyst for the oxygen evolution reaction in proton exchange membrane water electrolyser. *Int. J. Hydrog. Energy* **2014**, *39* (5), 1905−1913.

(155) Oakton, E.; Lebedev, D.; Povia, M.; Abbott, D. F.; Fabbri, E.; Fedorov, A.; Nachtegaal, M.; Copéret, C.; Schmidt, T. J. IrO$_2$-TiO$_2$: A High-Surface-Area, Active, and Stable Electrocatalyst for the Oxygen Evolution Reaction. *ACS Catal.* **2017**, *7* (4), 2346−2352.

(156) Mazúr, P.; Polonský, J.; Paidar, M.; Bouzek, K. Non-conductive TiO$_2$ as the anode catalyst support for PEM water electrolysis. *Int. J. Hydrog. Energy* **2012**, *37* (17), 12081−12088.

(157) Böhm, D.; Beetz, M.; Gebauer, C.; Bernt, M.; Schröter, J.; Kornherr, M.; Zoller, F.; Bein, T.; Fattakhova-Rohlfing, D. Highly conductive titania supported iridium oxide nanoparticles with low overall iridium density as OER catalyst for large-scale PEM electrolysis. *Appl. Mater. Today* **2021**, *24*, 101134.

(158) Schlicht, S.; Büttner, P.; Bachmann, J. Highly Active Ir/TiO$_2$ Electrodes for the Oxygen Evolution Reaction Using Atomic Layer Deposition on Ordered Porous Substrates. *ACS Appl. Energy Mater.* **2019**, *2* (3), 2344−2349.

(159) Lv, H.; Zhang, G.; Hao, C.; Mi, C.; Zhou, W.; Yang, D.; Li, B.; Zhang, C. Activity of IrO$_2$ supported on tantalum-doped TiO$_2$ electrocatalyst for solid polymer electrolyte water electrolyzer. *RSC Adv.* **2017**, *7* (64), 40427−40436.

(160) Lv, H.; Wang, S.; Hao, C.; Zhou, W.; Li, J.; Xue, M.; Zhang, C. Oxygen-Deficient Ti$_{0.9}$Nb$_{0.1}$O$_{2-x}$ as an Efficient Anodic Catalyst Support for PEM Water Electrolyzer. *ChemCatChem.* **2019**, *11* (10), 2511−2519.

(161) Hao, C.; Lv, H.; Mi, C.; Song, Y.; Ma, J. Investigation of Mesoporous Niobium-Doped TiO$_2$ as an Oxygen Evolution Catalyst Support in an SPE Water Electrolyzer. *ACS Sustain. Chem. Eng.* **2016**, *4* (3), 746−756.

(162) Zhao, S.; Stocks, A.; Rasimick, B.; More, K.; Xu, H. Highly active, durable dispersed iridium nanocatalysts for PEM water electrolyzers. *J. Electrochem. Soc.* **2018**, *165* (2), F82−F89.

(163) Mohammadnezhad, G.; Momeni, M. M.; Nasiriani, F. Enhanced photoelectrochemical performance of tin oxide decorated tungsten oxide doped TiO$_2$ nanotube by electrodeposition for water splitting. *J. Electroanal. Chem.* **2020**, *876*, 114505.

(164) Hao, C.; Lv, H.; Zhao, Q.; Li, B.; Zhang, C.; Mi, C.; Song, Y.; Ma, J. Investigation of V-doped TiO$_2$ as an anodic catalyst support for SPE water electrolysis. *Int. J. Hydrog. Energy* **2017**, *42* (15), 9384−9395.

(165) Siracusano, S.; Baglio, V.; D'Urso, C.; Antonucci, V.; Aricò, A. S. Preparation and characterization of titanium suboxides as conductive supports of IrO$_2$ electrocatalysts for application in SPE electrolysers. *Electrochim. Acta* **2009**, *54* (26), 6292−6299.

(166) Böhm, L.; Näther, J.; Underberg, M.; Kazamer, N.; Holtkotte, L.; Rost, U.; Marginean, G.; Wirkert, F.; Brodmann, M.; Hülser, T.; Köster, F. Pulsed electrodeposition of iridium catalyst nanoparticles on titanium suboxide supports for application in PEM electrolysis. *Mater. Today Proc.* **2021**, *45*, 4254−4259.

(167) Lu, Z.-X.; Shi, Y.; Yan, C.-F.; Guo, C.-Q.; Wang, Z.-D. Investigation on IrO$_2$ supported on hydrogenated TiO$_2$ nanotube array as OER electro-catalyst for water electrolysis. *Int. J. Hydrog. Energy* **2017**, *42* (6), 3572−3578.

(168) Abbou, S.; Chattot, R.; Martin, V.; Claudel, F.; Solà-Hernandez, L.; Beauger, C.; Dubau, L.; Maillard, F. Manipulating the Corrosion Resistance of SnO$_2$ Aerogels through Doping for Efficient and Durable Oxygen Evolution Reaction Electrocatalysis in Acidic Media. *ACS Catal.* **2020**, *10* (13), 7283−7294.

(169) Wang, L.; Song, F.; Ozouf, G.; Geiger, D.; Morawietz, T.; Handl, M.; Gazdzicki, P.; Beauger, C.; Kaiser, U.; Hiesgen, R.; Gago, A. S.; Friedrich, K. A. Improving the activity and stability of Ir catalysts for PEM electrolyzer anodes by SnO$_2$:Sb aerogel supports: does V addition play an active role in electrocatalysis? *J. Mater. Chem. A* **2017**, *5* (7), 3172−3178.

(170) Böhm, D.; Beetz, M.; Schuster, M.; Peters, K.; Hufnagel, A. G.; Döblinger, M.; Böller, B.; Bein, T.; Fattakhova-Rohlfing, D. Efficient OER Catalyst with Low Ir Volume Density Obtained by Homogeneous Deposition of Iridium Oxide Nanoparticles on Macroporous Antimony-Doped Tin Oxide Support. *Adv. Funct. Mater.* **2020**, *30* (1), 1906670.

(171) Ohno, H.; Nohara, S.; Kakinuma, K.; Uchida, M.; Uchida, H. Effect of Electronic Conductivities of Iridium Oxide/Doped SnO$_2$ Oxygen-Evolving Catalysts on the Polarization Properties in Proton Exchange Membrane Water Electrolysis. *Catalysts* **2019**, *9* (1), 74.

(172) Aricò, A. S.; Siracusano, S.; Briguglio, N.; Baglio, V.; Di Blasi, A.; Antonucci, V. Polymer electrolyte membrane water electrolysis: status of technologies and potential applications in combination with

renewable power sources. *J. Appl. Electrochem.* **2013**, *43* (2), 107−118.

(173) Carmo, M.; Fritz, D. L.; Mergel, J.; Stolten, D. A comprehensive review on PEM water electrolysis. *Int. J. Hydrog. Energy* **2013**, *38* (12), 4901−4934.

(174) Yi, Y. D.; Bae, Y. C. Swelling behaviors of proton exchange membranes in alcohols. *Polymer* **2017**, *130*, 112−123.

(175) Sun, L.; Ran, R.; Shao, Z. Fabrication and evolution of catalyst-coated membranes by direct spray deposition of catalyst ink onto Nafion membrane at high temperature. *Int. J. Hydrog. Energy* **2010**, *35* (7), 2921−2925.

(176) Sun, L.; Ran, R.; Wang, G.; Shao, Z. Fabrication and performance test of a catalyst-coated membrane from direct spray deposition. *Solid State Ion.* **2008**, *179* (21−26), 960−965.

(177) Thanasilp, S.; Hunsom, M. Effect of MEA fabrication techniques on the cell performance of Pt-Pd/C electrocatalyst for oxygen reduction in PEM fuel cell. *Fuel* **2010**, *89* (12), 3847−3852.

(178) Shi, Y.; Lu, Z.; Guo, L.; Yan, C. Fabrication of membrane electrode assemblies by direct spray catalyst on water swollen Nafion membrane for PEM water electrolysis. *Int. J. Hydrog. Energy* **2017**, *42* (42), 26183−26191.

(179) Stähler, A.; Stähler, M.; Scheepers, F.; Lehnert, W.; Carmo, M. Scalable Implementation of Recombination Catalyst Layers to Mitigate Gas Crossover in PEM Water Electrolyzers. *J. Electrochem. Soc.* **2022**, *169* (3), 034522.

(180) Hsu, C. An innovative process for PEMFC electrodes using the expansion of Nafion film. *J. Power Sources* **2003**, *115* (2), 268−273.

(181) Su, H.; Bladergroen, B. J.; Linkov, V.; Pasupathi, S.; Ji, S. Study of catalyst sprayed membrane under irradiation method to prepare high performance membrane electrode assemblies for solid polymer electrolyte water electrolysis. *Int. J. Hydrog. Energy* **2011**, *36* (23), 15081−15088.

(182) Leimin, X.; Shijun, L.; Lijun, Y.; Zhenxing, L. Investigation of a Novel Catalyst Coated Membrane Method to Prepare Low-Platinum-Loading Membrane Electrode Assemblies for PEMFCs. *Fuel Cells* **2009**, *9* (2), 101−105.

(183) Jung, H.-Y.; Kim, J. W. Role of the glass transition temperature of Nafion 117 membrane in the preparation of the membrane electrode assembly in a direct methanol fuel cell (DMFC). *Int. J. Hydrog. Energy* **2012**, *37* (17), 12580−12585.

(184) Tang, H.; Wang, S.; Jiang, S. P.; Pan, M. A comparative study of CCM and hot-pressed MEAs for PEM fuel cells. *J. Power Sources* **2007**, *170* (1), 140−144.

(185) Mehta, V.; Cooper, J. S. Review and analysis of PEM fuel cell design and manufacturing. *J. Power Sources* **2003**, *114* (1), 32−53.

(186) Siracusano, S.; Van Dijk, N.; Backhouse, R.; Merlo, L.; Baglio, V.; Aricò, A. S. Degradation issues of PEM electrolysis MEAs. *Renew. Energy* **2018**, *123*, 52−57.

(187) Park, J.; Shin, K.; Lee, C. Roll-to-Roll Coating Technology and Its Applications: A Review. *Int. J. Precis. Eng. Manuf.* **2016**, *17* (4), 537−550.

(188) Søndergaard, R.; Hösel, M.; Angmo, D.; Larsen-Olsen, T. T.; Krebs, F. C. Roll-to-roll fabrication of polymer solar cells. *Mater. Today* **2012**, *15* (1−2), 36−49.

(189) Hwang, K.; Jung, Y. S.; Heo, Y. J.; Scholes, F. H.; Watkins, S. E.; Subbiah, J.; Jones, D. J.; Kim, D. Y.; Vak, D. Toward large scale roll-to-roll production of fully printed perovskite solar cells. *Adv. Mater.* **2015**, *27* (7), 1241−1247.

(190) Mauger, S. A.; Wang, M.; Cetinbas, F. C.; Dzara, M. J.; Park, J.; Myers, D. J.; Ahluwalia, R. K.; Pylypenko, S.; Hu, L.; Litster, S.; Neyerlin, K. C.; Ulsh, M. Development of high-performance roll-to-roll-coated gas-diffusion-electrode-based fuel cells. *J. Power Sources* **2021**, *506*, 230039.

(191) Steenberg, T.; Hjuler, H. A.; Terkelsen, C.; Sánchez, M. T. R.; Cleemann, L. N.; Krebs, F. C. Roll-to-roll coated PBI membranes for high temperature PEM fuel cells. *Energy Environ. Sci.* **2012**, *5* (3), 6076−6080.

(192) Liu, P.; Yang, D.; Li, B.; Zhang, C.; Ming, P. Recent progress of catalyst ink for roll-to-roll manufacturing paired with slot die coating for proton exchange membrane fuel cells. *Int. J. Hydrog. Energy* **2023**, *48* (51), 19666−19685.

(193) Park, J.; Kang, Z.; Bender, G.; Ulsh, M.; Mauger, S. A. Roll-to-roll production of catalyst coated membranes for low-temperature electrolyzers. *J. Power Sources* **2020**, *479*, 228819.

(194) Wilson, M. S.; Gottesfeld, S. Thin-film catalyst layers for polymer electrolyte fuel cell electrodes. *J. Appl. Electrochem.* **1992**, *22* (1), 1−7.

(195) Burdzik, A.; Stähler, M.; Friedrich, I.; Carmo, M.; Stolten, D. Homogeneity analysis of square meter-sized electrodes for PEM electrolysis and PEM fuel cells. *J. Coat. Technol. Res.* **2018**, *15* (6), 1423−1432.

(196) Toudret, P.; Blachot, J.-F.; Heitzmann, M.; Jacques, P.-A. Impact of the Cathode Layer Printing Process on the Performance of MEA Integrating PGM Free Catalyst. *Catalysts* **2021**, *11* (6), 669.

(197) Mehmood, A.; Ha, H. Y. An efficient decal transfer method using a roll-press to fabricate membrane electrode assemblies for direct methanol fuel cells. *Int. J. Hydrog. Energy* **2012**, *37* (23), 18463−18470.

(198) Shahgaldi, S.; Alaefour, I.; Unsworth, G.; Li, X. Development of a low temperature decal transfer method for the fabrication of proton exchange membrane fuel cells. *Int. J. Hydrog. Energy* **2017**, *42* (16), 11813−11822.

(199) Park, J. E.; Kim, S.; Kim, O.-H.; Ahn, C.-Y.; Kim, M.-J.; Kang, S. Y.; Jeon, T. I.; Shim, J.-G.; Lee, D. W.; Lee, J. H.; Cho, Y.-H.; Sung, Y.-E. Ultra-low loading of IrO_2 with an inverse-opal structure in a polymer-exchange membrane water electrolysis. *Nano Energy* **2019**, *58*, 158−166.

(200) Jiang, G.; Yu, H.; Li, Y.; Yao, D.; Chi, J.; Sun, S.; Shao, Z. Low-Loading and Highly Stable Membrane Electrode Based on an Ir@WO$_x$NR Ordered Array for PEM Water Electrolysis. *ACS Appl. Mater. Interfaces* **2021**, *13* (13), 15073−15082.

(201) Neagu, R.; Zhang, X.; Maric, R.; Roller, J. M. Characterisation and Performance of SOFC Components Made by Reactive Spray Deposition Technology. *ECS Trans.* **2009**, *25* (2), 2481−2486.

(202) Ouimet, R. J.; Gado, A. M.; Bliznakov, S.; Bonville, L. J.; Maric, R. Advanced electrodes for electrochemical energy storage and conversion devices fabricated by reactive spray deposition technology. *Electrochem. Commun.* **2021**, *133*, 107162.

(203) Ayers, K. E.; Renner, J. N.; Danilovic, N.; Wang, J. X.; Zhang, Y.; Maric, R.; Yu, H. Pathways to ultra-low platinum group metal catalyst loading in proton exchange membrane electrolyzers. *Catal. Today* **2016**, *262*, 121−132.

(204) Yu, H.; Danilovic, N.; Wang, Y.; Willis, W.; Poozhikunnath, A.; Bonville, L.; Capuano, C.; Ayers, K.; Maric, R. Nano-size IrO_x catalyst of high activity and stability in PEM water electrolyzer with ultra-low iridium loading. *Appl. Catal., B* **2018**, *239*, 133−146.

(205) Zeng, Z.; Ouimet, R.; Bonville, L.; Niedzwiecki, A.; Capuano, C.; Ayers, K.; Soleymani, A. P.; Jankovic, J.; Yu, H.; Mirshekari, G.; Maric, R.; Bliznakov, S. Degradation Mechanisms in Advanced MEAs for PEM Water Electrolyzers Fabricated by Reactive Spray Deposition Technology. *J. Electrochem. Soc.* **2022**, *169* (5), 054536.

(206) Yu, H.; Bonville, L.; Jankovic, J.; Maric, R. Microscopic insights on the degradation of a PEM water electrolyzer with ultra-low catalyst loading. *Appl. Catal., B* **2020**, *260*, 118194.

(207) Bühler, M.; Holzapfel, P.; McLaughlin, D.; Thiele, S. From Catalyst Coated Membranes to Porous Transport Electrode Based Configurations in PEM Water Electrolyzers. *J. Electrochem. Soc.* **2019**, *166* (14), F1070−F1078.

(208) Choe, S.; Lee, B.-S.; Cho, M. K.; Kim, H.-J.; Henkensmeier, D.; Yoo, S. J.; Kim, J. Y.; Lee, S. Y.; Park, H. S.; Jang, J. H. Electrodeposited IrO_2/Ti electrodes as durable and cost-effective anodes in high-temperature polymer-membrane-electrolyte water electrolyzers. *Appl. Catal., B* **2018**, *226*, 289−294.

(209) Jeong, H.-Y.; Oh, J.; Yi, G. S.; Park, H.-Y.; Cho, S. K.; Jang, J. H.; Yoo, S. J.; Park, H. S. High-performance water electrolyzer with minimum platinum group metal usage: Iron nitride-iridium oxide

core-shell nanostructures for stable and efficient oxygen evolution reaction. *Appl. Catal., B* **2023**, *330*, 122596.

(210) Lim, A.; Kim, J.; Lee, H. J.; Kim, H.-J.; Yoo, S. J.; Jang, J. H.; Young Park, H.; Sung, Y.-E.; Park, H. S. Low-loading IrO₂ supported on Pt for catalysis of PEM water electrolysis and regenerative fuel cells. *Appl. Catal., B* **2020**, *272*, 118955.

(211) Yeo, K.-R.; Lee, K.-S.; Kim, H.; Lee, J.; Kim, S.-K. A highly active and stable 3D dandelion spore-structured self-supporting Ir-based electrocatalyst for proton exchange membrane water electrolysis fabricated using structural reconstruction. *Energy Environ. Sci.* **2022**, *15* (8), 3449−3461.

(212) Laube, A.; Hofer, A.; Ressel, S.; Chica, A.; Bachmann, J.; Struckmann, T. PEM water electrolysis cells with catalyst coating by atomic layer deposition. *Int. J. Hydrog. Energy* **2021**, *46* (79), 38972−38982.

(213) Kúš, P.; Ostroverkh, A.; Ševčíková, K.; Khalakhan, I.; Fiala, R.; Skála, T.; Tsud, N.; Matolin, V. Magnetron sputtered Ir thin film on TiC-based support sublayer as low-loading anode catalyst for proton exchange membrane water electrolysis. *Int. J. Hydrog. Energy* **2016**, *41* (34), 15124−15132.

(214) Liu, C.; Carmo, M.; Bender, G.; Everwand, A.; Lickert, T.; Young, J. L.; Smolinka, T.; Stolten, D.; Lehnert, W. Performance enhancement of PEM electrolyzers through iridium-coated titanium porous transport layers. *Electrochem. Commun.* **2018**, *97*, 96−99.

(215) Bühler, M.; Hegge, F.; Holzapfel, P.; Bierling, M.; Suermann, M.; Vierrath, S.; Thiele, S. Optimization of anodic porous transport electrodes for proton exchange membrane water electrolyzers. *J. Mater. Chem. A* **2019**, *7* (47), 26984−26995.

(216) Pham, C. V.; Bühler, M.; Knöppel, J.; Bierling, M.; Seeberger, D.; Escalera-López, D.; Mayrhofer, K. J. J.; Cherevko, S.; Thiele, S. IrO₂ coated TiO₂ core-shell microparticles advance performance of low loading proton exchange membrane water electrolyzers. *Appl. Catal., B* **2020**, *269*, 118762.

(217) Taie, Z.; Peng, X.; Kulkarni, D.; Zenyuk, I. V.; Weber, A. Z.; Hagen, C.; Danilovic, N. Pathway to Complete Energy Sector Decarbonization with Available Iridium Resources using Ultralow Loaded Water Electrolyzers. *ACS Appl. Mater. Interfaces* **2020**, *12* (47), 52701−52712.

(218) Deng, Y.; Chen, W.; Li, B.; Wang, C.; Kuang, T.; Li, Y. Physical vapor deposition technology for coated cutting tools: A review. *Ceram. Int.* **2020**, *46* (11), 18373−18390.

(219) Geyao, L.; Yang, D.; Wanglin, C.; Chengyong, W. Development and application of physical vapor deposited coatings for medical devices: A review. *Procedia CIRP* **2020**, *89*, 250−262.

(220) Miśkiewicz, P.; Frydrych, I.; Cichocka, A. Application of physical vapor deposition in textile industry. *Autex Res. J.* **2022**, *22* (1), 42−54.

(221) Bello, M.; Shanmugan, S. Achievements in mid and high-temperature selective absorber coatings by physical vapor deposition (PVD) for solar thermal Application-A review. *J. Alloys Compd.* **2020**, *839*, 155510.

(222) Shahidi, S.; Moazzenchi, B.; Ghoranneviss, M. A review-application of physical vapor deposition (PVD) and related methods in the textile industry. *Eur. Phys. J. Appl. Phys.* **2015**, *71* (3), 31302.

(223) Baptista, A.; Silva, F. J. G.; Porteiro, J.; Míguez, J. L.; Pinto, G.; Fernandes, L. On the Physical Vapour Deposition (PVD): Evolution of Magnetron Sputtering Processes for Industrial Applications. *Procedia Manuf.* **2018**, *17*, 746−757.

(224) *Toshiba's New Large-scale Production Technology for Electrolysis Electrodes for Hydrogen Production from Renewables Cuts Iridium Use to 1/10 - Promoting PEM water electrolyzers for power to gas technology that will contribute to realization of a hydrogen economy*; https://www.global.toshiba/ww/technology/corporate/rdc/rd/topics/22/2210-01.html/ (accessed 2023-10-15).

(225) Zatoń, M.; Rozière, J.; Jones, D. Current understanding of chemical degradation mechanisms of perfluorosulfonic acid membranes and their mitigation strategies: a review. *Sustain. Energy Fuels* **2017**, *1* (3), 409−438.

(226) Liu, C.; Wippermann, K.; Rasinski, M.; Suo, Y.; Shviro, M.; Carmo, M.; Lehnert, W. Constructing a Multifunctional Interface between Membrane and Porous Transport Layer for Water Electrolyzers. *ACS Appl. Mater. Interfaces* **2021**, *13* (14), 16182−16196.

(227) Hansen, K. U.; Cherniack, L. H.; Jiao, F. Voltage Loss Diagnosis in CO₂ Electrolyzers Using Five-Electrode Technique. *ACS Energy Lett.* **2022**, *7* (12), 4504−4511.

(228) Salvatore, D.; Berlinguette, C. P. Voltage Matters When Reducing CO₂ in an Electrochemical Flow Cell. *ACS Energy Lett.* **2020**, *5* (1), 215−220.

(229) Xu, Q.; Oener, S. Z.; Lindquist, G.; Jiang, H.; Li, C.; Boettcher, S. W. Integrated Reference Electrodes in Anion-Exchange-Membrane Electrolyzers Impact of Stainless-Steel Gas-Diffusion Layers and Internal Mechanical Pressure. *ACS Energy Lett.* **2021**, *6*, 305−312.

(230) Sorsa, O.; Nieminen, J.; Kauranen, P.; Kallio, T. Stable Reference Electrode in Polymer Electrolyte Membrane Electrolyser for Three-Electrode Measurements. *J. Electrochem. Soc.* **2019**, *166* (16), F1326−F1336.

(231) Bernt, M.; Gasteiger, H. A. Influence of Ionomer Content in IrO₂/TiO₂ Electrodes on PEM Water Electrolyzer Performance. *J. Electrochem. Soc.* **2016**, *163* (11), F3179−F3189.

(232) Xie, Z.; Yu, S.; Ma, X.; Li, K.; Ding, L.; Wang, W.; Cullen, D. A.; Meyer, H. M.; Yu, H.; Tong, J.; Wu, Z.; Zhang, F.-Y. MoS₂ nanosheet integrated electrodes with engineered 1T-2H phases and defects for efficient hydrogen production in practical PEM electrolysis. *Appl. Catal., B* **2022**, *313*, 121458.

(233) Knoppel, J.; Mockl, M.; Escalera-Lopez, D.; Stojanovski, K.; Bierling, M.; Bohm, T.; Thiele, S.; Rzepka, M.; Cherevko, S. On the limitations in assessing stability of oxygen evolution catalysts using aqueous model electrochemical cells. *Nat. Commun.* **2021**, *12* (1), 2231.

(234) Lin, R.; Lu, Y.; Xu, J.; Huo, J.; Cai, X. Investigation on performance of proton exchange membrane electrolyzer with different flow field structures. *Appl. Energy* **2022**, *326*, 120011.

(235) Yang, R.; Mohamed, A.; Kim, K. Optimal design and flow-field pattern selection of proton exchange membrane electrolyzers using artificial intelligence. *Energy* **2023**, *264*, 126135.